Ensemble cryoEM elucidates the mechanism of insulin capture and degradation by human insulin degrading enzyme

Zhening Zhang[1,*], Wenguang G. Liang[2,*], Lucas J. Bailey[3], Yong Zi Tan[1,9], Hui Wei[1], Andrew Wang[2], Mara Farcasanu[2], Virgil A. Woods[4], Lauren A. McCord[2], David Lee[4], Weifeng Shang[5], Rebecca Deprez-Poulain[6], Benoit Deprez[6], David R. Liu[7], Akiko Koide[8], Shohei Koide[8], Anthony A. Kossiakoff[3], Sheng Li[4,#], Bridget Carragher[1,9,#], Clinton S. Potter[1,9,#] and Wei-Jen Tang[2,#]

1. National Resource for Automated Molecular Microscopy, Simons Electron Microscopy Center, New York Structural Biology Center, 89 Convent Ave, New York, New York, 10027, USA
2. Ben-May Institute for Cancer Research, The University of Chicago, 929 East 57th Street, Chicago, Illinois 60637, USA
3. Department of Biochemistry and Molecular Biology, The University of Chicago, 929 East 57th Street, Chicago, Illinois 60637, USA
4. Department of Medicine, University of California at San Diego, 9500 Gilman Drive, La Jolla, CA 92093, USA
5. BioCAT, Argonne National Laboratory, Illinois 60439, USA
6. Univ. Lille, INSERM, Institut Pasteur de Lille, U1177 - Drug and Molecules for Living Systems, F-59000 Lille, France
7. Department of Chemistry and Chemical Biology, Harvard University
8. Perlmutter Cancer Center, New York University Langone Medical Center and Department of Biochemistry and Molecular Pharmacology, New York University School of Medicine, New York, NY 10016, USA
9. Department of Biochemistry and Molecular Biophysics, Columbia University, New York, NY 10032, USA.
* Contributed equally
# Corresponding authors

Abstract

Insulin degrading enzyme (IDE) plays key roles in degrading peptides vital in type 2 diabetes, Alzheimer's, inflammation, and other human diseases. However, the process through which IDE recognizes peptides that tend to form amyloid fibrils remained unsolved. We used cryoEM to understand both the apo- and insulin-bound dimeric IDE states, revealing that IDE displays a large opening between the homologous ~55 kDa N- and C-terminal halves to allow selective substrate capture based on size and charge complementarity. We also used cryoEM, X-ray crystallography, SAXS, and HDX-MS to elucidate the molecular basis of how amyloidogenic peptides stabilize the disordered IDE catalytic cleft, thereby inducing selective degradation by substrate-assisted catalysis. Furthermore, our insulin-bound IDE structures explain how IDE processively degrades insulin by stochastically cutting either chain without breaking disulfide bonds. Together, our studies provide a mechanism for how IDE selectively degrades amyloidogenic peptides and offers structural insights for developing IDE-based therapies.

Keywords: insulin, amyloid peptide, insulin degrading enzyme, proteostasis, diabetes, Alzheimer’s disease, cryoEM, crystallography, hydrogen-deuterium exchange, integrative structural biology.

Highlights

- Four new human dimeric IDE structures including insulin-bound, closed-state IDE and open-state IDE at 3.7 Å and 4.2 Å resolution, respectively.
- CryoEM structures of open-state dimeric IDE illuminate mechanisms of substrate capture and allostery.
- Stabilization of the catalytic site by substrates allows IDE to selectively degrade amyloidogenic peptides.
- IDE stochastically cleaves either chain of insulin to processively break down insulin into two pieces.

Introduction

Insulin degrading enzyme (IDE) is an evolutionarily conserved, M16 family metalloprotease that controls diverse biological functions in model organisms such as mating and cell division in budding yeast and growth in fruit flies (Adames et al., 1995; Fujita et al., 1994; Galagovsky et al., 2014; Tang, 2016). IDE is ubiquitously expressed in all tissues and can be found in almost all subcellular compartments, despite being made as a cytosolic protein (Tang, 2016; Tundo et al., 2017). IDE can effectively degrade insulin, amylin, and glucagon, pancreatic hormones that control blood glucose levels, as well as amyloid β (Aβ), a peptide implicated in Alzheimer's disease (Duckworth et al., 1998; Kurochkin et al., 2018; Pivovarova et al., 2016; Tang, 2016; Tundo et al., 2017). Defects in IDE alter the progression of type 2 diabetes mellitus and Alzheimer's disease in rodents, and are linked to these diseases in humans (Farris et al., 2003; Farris et al., 2004; Fuchsberger et al., 2016; Pivovarova et al., 2016; Tang, 2016; Tundo et al., 2017). Two IDE-specific inhibitors improve glucose tolerance (Durham et al., 2015; Maianti et al., 2014) and IDE overexpression reduces Aβ load in mice (Leissring et al., 2003), making this enzyme a promising therapeutic target (Kurochkin et al., 2018; Pivovarova et al., 2016; Tang, 2016; Tundo et al., 2017).

Crystallographic and biochemical studies have provided the framework for IDE substrate recognition (Guo et al., 2010; Malito et al., 2008a; Malito et al., 2008b; Manolopoulou et al., 2009; Noinaj et al., 2011; Ren et al., 2010; Shen et al., 2006; Tang, 2016). IDE is a 110 kDa zinc metalloprotease that readily dimerizes in solution (Kd=~10 nM) (Li et al., 2006). IDE has at least two major conformational states in its catalytic cycle; open-state IDE captures substrates and releases products while closed-state IDE performs catalysis (**Figure 1A**). Thus far, all crystal structures of dimeric IDE are in the closed state. Within the IDE dimer, each IDE subunit consists of ~55 kDa N- and C-terminal domains, IDE-N and IDE-C (**Figure 1B**). Together, these domains form an enclosed, sizable catalytic chamber, the size of which explains why IDE prefers to degrade peptides that are less than 80 amino acid long (**Figure 1B**). Various substrate-bound IDE structures reveal that the high selectivity of IDE is partly achieved by the specific interactions between the IDE catalytic chamber and substrate via size and charge complementarity (Guo et al., 2010; Malito et al., 2008b; Manolopoulou et al., 2009; Ralat et al., 2011; Ren et al., 2010; Shen et al., 2006). The formation of cross-β-sheet between an exposed β-strand in the unfolded substrate and the catalytic cleft in conjunction with the

anchoring of the substrate's N-terminus of substrate to a site that is ~30 Å away from the catalytic zinc ion explains how IDE selectively cleaves the exposed β-strand distal to the N-terminus of the targeted peptides in a stochastic manner (Shen et al., 2006).

Until now, structures of open and insulin-bound state IDE, two key conformations vital for the IDE catalytic cycle, have remained unsolved (**Figure 1A, 1C**). In closed-state IDE, substrate cannot enter into the catalytic chamber of IDE and the cleaved products cannot exit. Thus, IDE needs to undergo a significant open-closed transition during its catalytic cycle. In addition to contributing to an understanding of how IDE captures its substrate and releases its reaction products, the structure of open-state IDE can provide the insight into how the open-closed transition of IDE facilitates the unfolding of its substrates prior to the cleavage reaction as well as how IDE conducts its non-proteolytic roles, e.g., regulating proteasome activity and preventing amyloid fibril formation of α-synuclein (Sharma et al., 2015; Tang, 2016). The IDE-insulin interaction represents a unique challenge of how IDE interacts with its substrates. Insulin consists of A and B chains that are held together by two inter-molecular disulfide bonds. IDE processively degrades insulin into two pieces without breaking these disulfide bonds (**Figure 1A**) (Manolopoulou et al., 2009). The previously reported crystal structure of insulin-bound IDE reveals how insulin is partially unfolded inside the catalytic chamber of IDE, the first step in the unfolding and degradation of insulin by IDE (Manolopoulou et al., 2009) (**Figure 1C**). However, the structure of IDE in complex with the fully unfolded insulin prior to the processive cleavage of insulin has remained unsolved.

Amyloidogenic peptides such as Aβ can form highly toxic oligomers/fibrils, leading to many human disorders (Chiti and Dobson, 2006; Eisenberg and Jucker, 2012; Merlini and Bellotti, 2003). A salient feature of many amyloidogenic peptides is their high propensity to unfold, resulting in exposed β-strands that together form cross-β-sheets and then amyloid fibrils (Eisenberg and Jucker, 2012; Fitzpatrick et al., 2017; Lu et al., 2013). Nucleation to form low molecular weight oligomers is a key rate limiting step in the formation of amyloid fibrils (Merlini and Bellotti, 2003). IDE selectively degrades certain amyloidogenic peptides, preventing amyloid fibril formation (Kurochkin, 2001; Malito et al., 2008a). IDE achieves this by cutting only the monomeric form of these peptides and cleaving at sites located at the β-strand vital for cross-β-sheet formation (Malito et al., 2008a; Tang, 2016). Based on the absence of electron density for the catalytic zinc ion-containing IDE door subdomain in a previously reported Fab1-bound IDE crystal structure, we have put forth a hypothesis that IDE uses

substrate-assisted catalysis to recognize amyloidogenic peptides (McCord et al., 2013). Upon substrate capture, the open-closed transition of IDE causes amyloidogenic peptides to unfold. The resulting exposed β-strand then binds and stabilizes the catalytic cleft within the IDE door subdomain, leading to stochastic cleavage of these peptides. This hypothesis could explain how IDE uses substrate-induced stabilization of the IDE catalytic site to selectively degrade amyloidogenic peptides. However, this hypothesis has not been formally tested. Thus, the molecular basis for the recognition of amyloidogenic peptides by IDE remains unsolved.

Recent advances in cryogenic electron microscopy (cryoEM) have profoundly transformed structural biology, making it possible to obtain near atomic resolution 3D structures that are otherwise difficult to achieve by crystallography (Henderson, 2015; Merk et al., 2016). Here, we report cryoEM structures of apo and unfolded insulin-bound human IDE, which is recalcitrant to crystallography. Hydrogen-deuterium exchange coupled with mass spectrometry (HDX-MS) and small angle X-ray scattering (SAXS) have recently become widely used techniques to characterize the high order structure of proteins and protein complexes under physiological conditions in solution, nicely complement high resolution techniques such as crystallography and cryoEM (Blanchet and Svergun, 2013; Marciano et al., 2014; Putnam et al., 2007; Ward et al., 2013; Wei et al., 2014). We integrate all four aforementioned structure methods to elucidate the molecular basis of how IDE captures, unfolds, and degrades its substrates and how IDE recognizes amyloidogenic peptides.

Results

Fab-assisted cryoEM of human IDE

Because IDE in the open conformation has proved recalcitrant to crystallization, we explored the use of cryoEM to study these structures. While IDE readily dimerizes (K_d=10 nM), the dimer's overall size (220 kDa), pseudo two-fold symmetry and conformational heterogeneity made it challenging for cryoEM (data not shown). We addressed these issues by using Fab-assisted cryoEM (Kim et al., 2015; Lyumkis et al., 2013; Wu et al., 2012). To identify Fabs that bind IDE tightly, we screened a phage-display synthetic Fab library constructed using “restricted chemical diversity” where positions randomized within the complementarity determining regions are biased towards amino acids enriched in antibody paratopes (Miller et al., 2012). This allowed rapid identification of eighteen high-affinity IDE binding Fabs without

immunization. Fab_{H11} was chosen because it bound IDE tightly (~1nM) and only slightly increased IDE activity (**Figure 2-figure supplement 1A-C**). We then rigidified the elbow region between the heavy and light chain of Fab_{H11}, which has improved the resolution of several structures that used Fab as the crystallization chaperone (Bailey et al., 2018). The resulting molecule, $Fab_{H11\text{-}E}$, was then used to determine an X-ray structure of $Fab_{H11\text{-}E}$-bound IDE at 3.8Å resolution (R/R_{free}=22/27%, **Supplementary file 1**). This structure reveals the binding epitope of this Fab to IDE (**Figure 2A, 2B**). The tight binding between IDE and $Fab_{H11\text{-}E}$ is mediated by a network of hydrogen bonds and van der Waal contacts (**Figure 2B**). The crystal structure revealed a closed-state IDE dimer that is nearly identical to those reported previously (**Figure 2-figure supplement 1D**)(Guo et al., 2010; Malito et al., 2008b; Manolopoulou et al., 2009; Ren et al., 2010; Shen et al., 2006). All crystal structures of IDE dimer solved so far are in the closed state, likely due to the constraints imposed by the crystal lattice. This illustrates the challenge in using crystallography to decipher the structure of open-state IDE.

In order to ensure that Fab binding does not alter the conformation and function of IDE, we applied HDX-MS to assess whether $Fab_{H11\text{-}E}$ causes noticeable global change in IDE conformations in solution because HDX-MS not only probes the binding regions of a given protein with its partners but also examines protein dynamics and regional stability (Chung et al., 2011; Li et al., 2011; Marciano et al., 2014). As predicted from the $Fab_{H11\text{-}E}$-bound IDE crystal structure, we found epitope residues 374-394 to be the primary region that displays strong reduction in HDX. Two additional regions, residues 297 to 303 and residues 501 to 508, also show moderate reduction in HDX in response to $Fab_{H11\text{-}E}$ binding (**Figure 2C, Figure 2-figure supplement 2-4**). Together, these three regions form a conformational binding epitope, which is in an excellent agreement with our crystal structure. As there is no major change in HDX between IDE alone and $Fab_{H11\text{-}E}$-bound IDE that is distal to $Fab_{H11\text{-}E}$ binding site, our HDX-MS data also suggest that $Fab_{H11\text{-}E}$ binding has a minimal effect on the conformation dynamics or regional stability of IDE in solution. We only found a minor reduction in HDX in a small region, residues 169 to 198, which is a part of IDE door subdomain that contains the catalytic zinc ion. Interestingly, the stabilization of IDE door subdomain is a key feature induced by substrate binding, which is discussed in details in *"substrate-induced conformational change of IDE"*. This could explain a 50% enhancement of IDE catalytic activity upon $Fab_{H11\text{-}E}$ binding (**Figure 2-figure supplement 1C**). Altogether, our data suggests that $Fab_{H11\text{-}E}$ does not significantly alter the global structure or activity of IDE. Thus, the cryoEM

structures of $Fab_{H11\text{-}E}$-bound IDE is likely to represent the conformations of IDE dimer in solution.

We then performed cryoEM structural analysis of the $Fab_{H11\text{-}E}$-bound IDE dimer in the presence and absence of insulin. 3D maps were reconstructed from 388,643 and 762,283 particles for apo- and insulin-bound IDE-$Fab_{H11\text{-}E}$ complex, respectively (**Figure 2D-F; Figure 2-figure supplement 5-10; Supplementary file 2-3**). A cryoEM map of the insulin-bound IDE-$Fab_{H11\text{-}E}$ was constructed using 218,162 particles initially, refined, and solved at 4.1 Å resolution, which confirms how $Fab_{H11\text{-}E}$ binds IDE (**Figure 2G**, **Figure 2-figure supplement 8B, Supplementary file 3**). We further improved the resolution of the IDE dimer using IDE dimer-focused classification with signal subtraction and refinement, resulting in a map and structural model with an overall resolution of 3.7 Å (**Figure 2-figure supplement 8B,9,10, Supplementary file 3**). Apo $Fab_{H11\text{-}E}$-bound IDE showed a highly preferred orientation in vitreous ice. Thus, images were acquired with the grid tilted at an angle to the electron beam, which allowed better sampling of other orientations (**Figure 2F, Figure 2-figure supplement 9B**) (Tan et al., 2017). The initial 3D refinement of apo IDE-$Fab_{H11\text{-}E}$ of 151,868 particles had a resolution of 4.4 Å. Further 3D classification revealed three major conformations and structural models were built (**Supplementary file 3**). We again applied IDE dimer-focused classification with signal subtraction of the IDE-$Fab_{H11\text{-}E}$ dimer to refine each conformation separately, which improved the resolution significantly (**Figure 2-figure supplement 9A, Supplementary file 3**). The three apo-IDE structures derive from combinations of the IDE partial open (pO) and open (O) states (**Figure 3A**). The dimer with one open and one partially open conformational subunit (open/partial open, 110,499 particles) reached an overall resolution of 4.2 Å (**Figure 3A, Figure 2-figure supplement 5-9, Supplementary file 3**). The dimer with two open conformational subunits (open/open, 24,425 particles) resulted in an overall resolution of 6.5 Å (**Figure 3A, Figure 2-figure supplement 5-9, Supplementary file 3**). The dimer with two partially open conformational subunits (partial open/partial open, 16,944 particles) reached 6.9 Å resolution (**Figure 3A, Figure 2-figure supplement 5-9, Supplementary file 3**).

CryoEM structures of IDE dimer

CryoEM analysis reveals four novel IDE dimer structures, one from insulin-bound IDE and three from apo-IDE (**Figure 3A**). The cryoEM structure of the insulin-bound IDE dimer at 3.7 Å resolution (**Movie S1-2**) shows that both IDE subunits adopt a similar but not identical

partially closed (pC) state that differs from the previously-reported closed-state IDE (**Figure 3B, Figure 3-figure supplement 1, Supplementary file 4**) (Guo et al., 2010; Malito et al., 2008b; Manolopoulou et al., 2009; Ren et al., 2010; Shen et al., 2006). The buried surface area between IDE-N and IDE-C and distance between center of mass (COM) of D1 and D4 in the cryoEM pC state is nearly identical to those in the closed-state IDE shown by X-ray crystallographic studies (**Figure 3B, Supplementary file 4**). However, this pC state has an approximately 2° decreased dihedral angle between the COM of four homologous domains, D1-D4, compared to those in the closed-state IDE (**Figure 3B, Supplementary file 4**), suggesting a potential gliding motion allows IDE to shift between partially-closed and closed states. The position of insulin in the catalytic cleft of the cryoEM maps reveals that the IDE pC state is ready for catalysis. Thus, both IDE pC and C states are catalytically competent.

The combinations of the IDE partial open (pO) and open (O) states results in three apo-IDE structures (**Figure 3A**). The IDE pO and O states differs from the pC and C states by 5 Å to 24 Å increases in the distance between D1 and D4 and 7° to 17° increases in the dihedral angle, respectively (**Figure 3B, Figure 3-figure supplement 1, Supplementary file 4, Movie S1**). These changes result in decreased buried surface between IDE-N and IDE-C in pO and O states. The three conformers have resolution limits which correlated well with their relative populations: O/pO (4.2 Å, 73%), O/O (6.5 Å, 16%), and pO/pO (6.9 Å, 11%). Interestingly, the conformation of pO and O states in the pO/O IDE dimer differ significantly from those in pO/pO or O/O IDE dimer. Furthermore, two subunits within O/O or pO/pO states have noticeable differences in the distance and buried surface between IDE-N and IDE-C and the dihedral angle (**Supplementary file 4**). Such differences provide a potential explanation for the mechanism by which dimerization-induced allostery regulates the catalytic activity of IDE (**Figure 3B, Figure 3-figure supplement 1**) (McCord et al., 2013; Ralat et al., 2011; Song et al., 2010). Open-state IDE has an opening just wide enough to capture its substrates, e.g., insulin, TGF-α, and MIP-1α/β, allowing the IDE catalytic chamber to attract these substrates with high dipole moment via charge complementarity (**Figure 3D**) (Guo et al., 2010; Manolopoulou et al., 2009; Ren et al., 2010).

SAXS analysis of IDE

Our cryoEM structures reveal that only open-state IDE can capture its prototypical substrate, insulin, and release cleaved products. The interaction of open-state IDE with insulin likely facilitates the open-closed transition of IDE. We chose SAXS to test this hypothesis because SAXS provides the ensemble information regarding size and shape of molecules in solution (Blanchet and Svergun, 2013). To exclude IDE monomer and larger aggregates, we used size exclusion chromatography in-line with SAXS. Such a SAXS profile of the IDE dimer allows us to assess the distribution of open- and closed-state IDE in the presence and absence of insulin with better precision. We evaluated the experimental data with the prediction from our cryoEM models using the radius of gyration (R_g), the average of square center of mass distances of the molecule, and the distance distribution function, p(r) (**Figure 4A, Figure 4-figure supplement 1**). Our SAXS data showed that IDE in solution exist in equilibrium between open and partially-open states and that insulin constrained the IDE dimer into mostly partially-closed or closed states. This agrees with our observation in cryoEM.

Enzyme kinetic analysis estimated that insulin degradation by IDE occurs reasonably rapidly, up to ~2 per second (Manolopoulou et al., 2009). To assess whether the insulin-induced open-closed transition of IDE could limit insulin degradation by IDE, we used time-resolved SAXS analysis to obtain rate constants for the insulin-induced open-closed transition of IDE. Time-resolved SAXS experiments were done using a microfluidic laminar flow mixer adapted from the design initially developed for time resolved fluorescence studies (Park et al., 2008; Park et al., 2006). We found that the change in R_g value caused by the rapid mixing of IDE with insulin fit well with a single exponential decay with τ = 0.1 sec (**Figure 4B**). Thus, the timeframe required for insulin to induce conformational switching from a high R_g state to a low R_g state is close to the rate of degradation of insulin by IDE (~2 s^{-1}). This suggests that insulin-induced IDE open-closed transition is likely a key rate-limiting step for insulin clearance by IDE.

Substrate-induced conformational changes of IDE

In a previous crystal structure of the Fab1-bound closed apo-IDE, one subunit within the IDE dimer did not have the electron density for the IDE door subdomain (McCord et al., 2013). This leads to the hypothesis that IDE has a catalytic zinc-containing door subdomain that is partially unfolded and/or undergoes a rigid body motion. This hypothesis predicts that, under

the crystallization conditions used for Fab1-bound closed apo-IDE crystal structure, the presence of IDE substrates would stabilize IDE door domain, rendering it visible. We thus solved crystal structures for Fab1-bound IDE structures in the presence of Aβ and insulin at 3.5 Å and 3.9 Å resolution, respectively (R/R_{free}=23/27%, R/free = 24/29%) and $Fab1_E$- and insulin-bound IDE at 3.3 Å resolution (R/R_{free}=20/25%) (**Supplementary file 1**). Instead of being absent, as in the apo-IDE crystal structure (McCord et al., 2013), we found that the door subdomain of IDE is clearly visible in these structures (**Figure 5A**). In fact, these IDE structures are nearly identical to closed-state IDE determined in the previously reported insulin- or Aβ-bound IDE (RMSD=0.46 and 0.56 Å, respectively, **Figure 5-figure supplement 1**). Consistent with that notion that this is induced by substrate, unfolded Aβ or insulin is clearly visible inside the IDE catalytic chamber. This hypothesis also predicts that the IDE door subdomains in the cryoEM structures of apo-IDE dimer would have the higher thermal B factors than those in that of insulin-bound IDE dimer. Indeed, while clearly visible, the IDE door subdomain, particularly the catalytic zinc-coordinating α4 helix, has significantly higher thermal B factors than in the insulin-bound structure (**Figure 5B, Figure 5-figure supplement 2**). The presence of insulin thus profoundly reduces the thermal B factors of IDE door subdomain (**Figure 5B, Figure 5-figure supplement 2**). Together, our data support the stabilization of the partial unfolding and/or motion of IDE catalytic domain by substrate binding. This lends credence to our hypothesis that IDE catalysis is assisted by its substrates and the importance of this region to the proper functioning of the enzyme.

We then probed the dynamics of IDE door subdomain using two high affinity IDE inhibitors, BDM44768 and 6bK by HDX-MS. Peptide amide HDX is a powerful tool to probe protein conformational dynamics because it allows evaluation of comparative solvent accessibility throughout the protein (Chung et al., 2011; Deprez-poulain et al., 2015a; Li et al., 2011; Maianti et al., 2014; Marciano et al., 2014). These two inhibitors bind different sites to compete with substrate binding. BDM44768 binds the IDE catalytic zinc-binding site while 6bK binds to a site distinct from the catalytic cleft and the N-terminal substrate anchoring exosite. In addition to the expected HDX reduction where BDM44768 and 6bK directly bind, both inhibitors also decreased HDX in the IDE door subdomain (**Figure 5C, 5D, Figure 5-figure supplement 3-6**). These data support the dynamic nature of the catalytic cleft within IDE door subdomain and the importance of this region to the proper functioning of the enzyme.

The combination of HDX-MS with cryoEM structures offers a framework for studying the detailed conformational changes of IDE induced by its substrates. Multiple regions in IDE exhibited a significant reduction in HDX upon insulin binding (**Figure 6A, Figure 6-figure supplement 1-4**). These regions correlate well with those that have higher thermal B factors in our cryoEM structures when insulin is absent (**Figure 5B**). These include known substrate-binding sites of IDE: the door subdomain that contains the zinc catalytic site in domain D1, exosite in domain D2 that anchors the N-terminal region of IDE substrates, and residues 821-830 in domain D4 that binds the P1' and P2' residues of IDE substrates after the scissile bond (McCord et al., 2013; Shen et al., 2006). Insulin also reduced HDX in regions that directly bind IDE door subdomain including the hydrophobic rich H loop, residues 668-673 and residues 821-830 (McCord et al., 2013). Together, these data support the conclusion that the binding of substrate stabilizes the IDE catalytic site. Furthermore, insulin binding also reduced the HDX at the IDE-N and IDE-C joining loop and its underlying α-helices, α11 and α20, which is consistent with our SAXS data showing that insulin facilitates the open-closed transition of IDE. A similar pattern of HDX reduction in IDE was also observed when IDE was mixed with $A\beta_{1-40}$ (**Figure 6B**). However, subtle but noticeable differences exist that could aid the search to achieve substrate-selective modulation of IDE. For example, insulin stabilizes the entire IDE door subdomain (residues 170-237) while Aβ only stabilizes the zinc binding portion of IDE door subdomain (residues 170-203) (**Figure 6-figure supplement 3-4**). Together, our data indicate that the binding of substrates promotes the open to closed transition of IDE and stabilizes the IDE catalytic site for substrate-assisted catalysis.

Mechanism for the processive degradation of insulin by IDE

IDE processively cuts insulin into two pieces without breaking the disulfide bonds that hold the insulin A and B chains together (**Figure 7A**) (Manolopoulou et al., 2009). However, previously reported insulin-bound IDE structures could not explain the processivity of insulin degradation by IDE (Manolopoulou et al., 2009). In our cryoEM and crystal structures of insulin-bound IDE, extra electron density was clearly visible inside the IDE catalytic chamber (**Figure 7B, 7C, Figure 7-figure supplement 1**), and the insulin structure is quite different to that reported previously (Manolopoulou et al., 2009). The extra density fit well with regions of an unfolded insulin A or B chain with a known scissile bond properly residing at the IDE

catalytic site (**Figure 7A, 7B, Figure 7-figure supplement 2**). Additional density is present for part of the other insulin chain, linked by the expected intermolecular disulfide bonds (**Figure 7A, Figure 7-figure supplement 2**). We also found that the N-terminus displays density characteristic of phenylalanine 1 of the insulin B chain, while other density corresponds to the ring structure formed by an intramolecular disulfide and a bulky tyrosine 14 side chain at the P1' cleavage site, which are characteristic of the insulin A chain (**Figure 7-figure supplement 2**). Thus, this density has key features that can be contributed by either chain and can be best interpreted as an ensemble of unfolded insulin A and B chains, not belonging solely to either chain.

Together, these structures provide the molecular basis of how IDE could processively cut insulin into two pieces without having to choose which insulin chain to cut first. Upon insulin capture by IDE catalytic chamber, IDE stochastically cuts whichever of either insulin A or B chain binds the IDE catalytic cleft first after insulin unfolding inside the catalytic chamber (**Figure 8A**). Our structures also reveal that the N-terminus of insulin interacts extensively with the IDE-N exosite while IDE-C makes substantial contacts with the C-terminal part of insulin. As the N- and C-terminal parts of insulin of the singly-cut insulin are still joined by the inter-molecular disulfide bond, insulin could still effectively keep IDE in the closed conformation. The subsequent unfolding of cleaved insulin leads to processive cleavage of the other insulin chain (**Figure 8A**). The resulting N- and C-terminal insulin fragments would then be released upon the closed to open transition of IDE.

Discussion

By combining cryoEM, crystallography, SAXS, and HDX-MS, our integrative structural analysis reveals the molecular details of how IDE undergoes open to closed conformational switches for the capture, unfolding, and degradation of insulin and peptides that tend to form amyloid fibrils (**Figure 8B**). By rigid-body motion between IDE-N and IDE-C, IDE switches between O and pO states. This results in three possible conformers where the O/pO dimer is dominant (**Figure 8B, Movie S3**). Only open-state IDE captures large peptide substrates (e.g., insulin and Aβ). The degree of opening and the charge distribution of the IDE catalytic chamber determine which peptides are captured by IDE depending on their size and high dipole moment (**Figure 3D**). The motions between open- and closed-state IDE, in conjunction with the selective interactions of the IDE catalytic chamber with these peptides, e.g., IDE

exosite with peptide's N-terminus, creates a force to selectively unfold amyloidogenic peptides. The exposed β-strand of these peptides then stabilizes the inherently unstable IDE catalytic center, leading to the degradation of amyloidogenic peptides by IDE.

The cryoEM structures of open-state IDE suggest the additional ways how IDE may work. Based on the size of catalytic chamber in the closed-state IDE, it is postulated that the entrapment of substrates inside the enclosed catalytic chamber of IDE is required for catalysis (Malito et al., 2008a; Shen et al., 2006). Thus, IDE only degrades peptides that are capable of fitting into the IDE catalytic chamber. This explains well why all of well characterized IDE substrates are peptides less than 80 amino acids long (Malito et al., 2008a; Tang, 2016). This model has successfully guided the identification of CCL3 and CCL4 as novel IDE substrates and the combination of the oligomerization of these chemokines and their degradation by IDE modulates the effectiveness of the chemotactic gradient formed by these chemokines (Ren et al., 2010). It does not escape our attention that IDE should be able to degrade larger proteins if such proteins are readily captured by open-state IDE via the charge and surface complementarity and can effectively stabilize IDE catalytic cleft. We also envision that open-state IDE can bind α-synuclein oligomers and alter the kinetics of oligomerization process, which explains how IDE reduces the amyloid fibril formation of α-synuclein *in vitro* (Sharma et al., 2015).

The catalytic activity of IDE is allosterically regulated by its substrate, ATP, and other partner proteins (McCord et al., 2013; Ralat et al., 2011; Song et al., 2003; Song et al., 2010; Tang, 2016). Based on our data, we put forth a model to explain how the equilibrium between IDE open and "closed" states facilitates IDE allostery (for simplicity, we group structurally similar pO, pC, and C states into the "closed" state that is distinct from open-state IDE). By the extensive contacts between IDE-C domains, IDE readily dimerizes (Kd=~10 nM) (Li et al., 2006; Shen et al., 2006). Our cryoEM data reveal that two IDE-N domains within the IDE dimer undergoes rigid body motion, allowing IDE to undergo the transition between the open and "closed" states without the assistance of substrate (**Figure 8B**). Furthermore, the preferred O/pO combination indicates that the motion of IDE-N in one subunit of IDE dimer is not independent from the other (**Figure 8B**). We thus envision that the preferred combination of the open and "closed" states within the IDE dimer would allow the substrate-induced closure of one subunit to promote the switch of the other subunit to the open state, allowing cleaved products to be released or substrate captured (**Movie S3 synchronized motion 1**).

Conversely, the opening of one subunit from the "closed"-state will promote the closure of the other for substrate unfolding and catalysis (**Movie S3 synchronized motion 1**). Such motions can explain how substrate allosterically regulates IDE activity and how monomerization mutations render IDE less active as well as the lose the ATP- and substrate-mediated regulation (Ralat et al., 2011; Song et al., 2003; Song et al., 2010). This model is also consistent with the kinetic studies which show that phenylalanine 530 mutation to alanine at the linker joining IDE-N and IDE-C makes IDE hyperactive and alters allosteric regulation (McCord et al., 2013). Our HDX-MS data reveal that the binding of IDE substrate or inhibitor only affects the deuterium exchange at the IDE-N and IDE interface and the linker between IDE-N and IDE-C, not between the interface of two IDE subunits (**Figure 5,6**). Thus, our data does not offer an obvious path for substrate-facilitated allosteric communication between IDE subunits. We speculate that IDE allostery is mediated by the collective motions of many atoms in IDE, not by a subset of atoms within a defined path. The detailed mechanism for IDE allostery awaits future MD simulation studies.

Many, if not most, molecular machines are conformationally heterogeneous, adopting a variety of different structural conformers in solution as they adapt form to serve function. CryoEM is uniquely capable of solving the structures of these large flexible macro-molecules. Improvements in the hardware technology over the past 5 years (Li et al., 2013) now provide for excellent quality images and improvements in software allow for classification of particles of different conformations from a heterogeneous mixture of structures (Scheres, 2012). Our approach to obtain cryoEM structure of the open-state IDE, a key functional state recalcitrant to crystallization, is generally applicable to other proteins. In addition to its relatively small size (220 kDa), the IDE dimer adopts multiple conformational states to fulfill its function. To solve the challenge posed by size and pseudo two-fold symmetry in our system, we included high-affinity IDE-binding Fabs, which increases the size of the complex, breaks the apparent symmetry, and provides excellent fiducials for validating the morphology and resolution of the overall structure. We take advantage of two other technological developments to improve cryoEM structure determination of the IDE dimer. A new vitrification device, Spotiton, allows us to prepare samples embedded in a very thin and even layer of vitrified ice, which improves data quality (Dandey et al., 2018; Razinkov et al., 2016). We also addressed the issues of preferred orientation, quite common for many samples, by acquiring images from gold coated grids tilted relative to the electron beam (Russo and Passmore, 2014; Tan et al., 2017). In conjunction with the state-of-art hardware and software in data acquisition, these

implementations allowed us to obtain near atomic resolution 3D structures of the open-state IDE despite its conformational heterogeneity.

The accumulation of toxic amyloid fibrils is associated with many human diseases and IDE plays a key role in preventing amyloid fibril formation by its proteolytic activities (Jucker and Walker, 2013; Tang, 2016). Accumulating data also suggest that IDE plays non-proteolytic roles to regulate other proteostatic processes, e.g., regulating proteasome activity and preventing amyloid fibril formation of α-synuclein (Tang, 2016). As IDE modulates proteostasis by targeting diverse proteins, substrate selective modulation of IDE activity is crucial to realize IDE-based therapy (Pivovarova et al., 2016; Tang, 2016). Indeed, noticeable differences in the reduction of HDX between insulin- and Aβ-bound IDE exist (**Figure 6A, 6B**). Together with our cryoEM structures, our studies offer a road map to develop insulin-selective inhibitors or Aβ-selective enhancers to treat diabetes and Alzheimer's disease.

Material and Methods

Key Resource table

Reagent type (species) or resource	Designation	Source or reference	Identifiers	Additional information
Antibody	Synthetic anti-IDE antibody Fab fragment ($Fab_{H11\text{-}E}$)	This study	NA	About 5 mg/ml for crystallization, and 0.15 mg/ml for cryoEM.
Antibody	Synthetic anti-IDE antibody Fab fragment Fab1Fab1	(McCord et al., 2013)	NA	About 5mg/ml for crystallization.
Recombinant protein (Human)	Cysteine-free IDE	This study	NA	Described as above.
Recombinant protein (Human)	Cysteine-free IDE-E111Q	This study	NA	Described as above.
Recombinant protein (Human)	Insulin	Sigma-Aldrich	234-279-7	
Recombinant protein (Human)	Amyloid β	(King et al., 2014)	NA	
Recombinant protein (Human)	Pepsin	Sigma-Aldrich	P6887-1G	

Chemical compound, drug	BDM44768	(Deprez-Poulain et al., 2015b)	NA	
Chemical compound, drug	6bK	(Maianti et al., 2014)	NA	
Chemical compound	D2O	Cambridge Isotope Laboratories, Inc.	DLM-4-1L	
Software, algorithm	Leginon 3.3	(Suloway et al., 2005)	NA	http://emg.nysbc.org/redmine/projects/leginon/wiki/Leginon_Homepage
Software, algorithm	DoGpicker	(Voss et al., 2009)	NA	http://emg.nysbc.org/redmine/projects/software/wiki/DoGpicker
Software, algorithm	MotionCor2	(Zheng et al., 2017)	NA	http://msg.ucsf.edu/em/software/motioncor2.html
Software, algorithm	Relion2.0	(Scheres, 2012)	NA	http://www2.mrc-lmb.cam.ac.uk/relion/index.php/Main_Page
Software, algorithm	Relion2.1	(Scheres, 2012)	NA	http://www2.mrc-lmb.cam.ac.uk/relion/index.php/Main_Page
Software, algorithm	3DFSC	(Tan et al., 2017)	NA	https://github.com/nysbc/Anisotropy
Software, algorithm	UCSF ChimeraX	(Goddard et al., 2017)	NA	https://www.cgl.ucsf.edu/chimerax/
Software, algorithm	UCSF Chimera	(Pettersen et al., 2004)	NA	https://www.cgl.ucsf.edu/chimera
Software, algorithm	PHENIX	(Adams et al., 2010)	NA	https://www.phenix-online.org/
Software, algorithm	Phaser-MR	(McCoy et al., 2007)	NA	https://www.phenix-online.org/documentation/tutorials/mr.html
Software, algorithm	COOT	(Emsley et al., 2010a)	NA	https://www2.mrc-lmb.cam.ac.uk/personal/pemsley/coot

Software, algorithm	MolProbity	(Chen et al., 2010)	NA	http://www.ks.uiuc.edu/Research/mdff/
Software, algorithm	PRIMUS	(Konarev et al., 2003)	NA	https://www.embl-hamburg.de/biosaxs/primus.html
Software, algorithm	CRYSOL	(Svergun et al., 1995)	NA	https://www.embl-hamburg.de/biosaxs/crysol.html
Software, algorithm	GNOM	(Svergun, 1992)	NA	https://www.embl-hamburg.de/biosaxs/gnom.html
Software, algorithm	SEQUEST/Proteome Discoverer Software	ThermoFisher Scientific	NA	https://www.thermofisher.com/order/catalog/product/OPTON-30795
Software, algorithm	HDEXaminer	Sierra Analytics	NA	http://massspec.com/hdexaminer/

Protein: Wild type human IDE, cysteine-free IDE (IDE-CF), and catalytically inactive IDE mutant, IDE-CF-E111Q were expressed in *E. coli* BL21 (DE3) cells (at 25 °C and 20 h, 0.5mM IPTG induction using T7 medium). His-tagged, biotinylated IDE was expressed in *E. coli* BL21 (DE3) that carried two plasmids, one for IDE with an N-terminal His-tag and a C-terminal AviTag (GLNDIFEAQKIEWHE), and the other for *E. coli* BirA, a biotin ligase that transfers biotin to AviTag. Recombinant IDE proteins were purified by Ni-NTA, source-Q, and Superdex 200 columns as previously described (Manolopoulou et al., 2009). $A\beta_{1\text{-}40}$ was synthesized at a 0.25 mmol scale using Fmoc and HBTU/HOBt chemistry on an Applied Biosystems 433A instrument and purified by RP-HPLC, lyophilized, and stored at -20 °C under Argon as described (King et al., 2014; Sohma et al., 2004). Insulin was purchased from SIGMA (91077C).

IDE-binding synthetic antibody: We screened antigen-binding fragments (Fab) from a phage-display library using immobilized biotinylated IDE as previously described (Miller et al., 2012). To obtain Fabs binding to an epitope distinct from the previously reported IDE-Fab named Fab1 (McCord et al., 2013), we used 1 μM Fab1 as a competitor for panning in the final round of selection. In total, 18 new IDE binding Fabs were isolated and characterized. Of those, IDE-Fab_{H11} was used in structural studies. Elbow-enhanced Fab1 ($Fab1_E$) and $Fab_{H11\text{-}E}$ were engineered to modify the switch residue region of the Fab heavy chain (wild-type sequence: ^{109}VTVSSASTKGP^{119}) to VTVFNQIKGP (Bailey et al., 2018). Fabs were expressed in *E. coli* strain BL21(DE3) or 55244 and purified using a HiTrap protein-G HP column or Protein-G-A1 column as described (Bailey et al., 2014; McCord et al., 2013). Surface plasmon resonance measurements were carried out at 20°C on a Biacore 3000 by immobilizing His-tagged IDE onto a Ni-NTA chip (GE Healthcare) and then injecting 3.3-100 nM of the Fab at a flow rate of 30 μl/min as previously described (Koide et al., 2012; Zhang et al., 2012).

Enzymatic activity assays: A fluorogenic bradykinin-mimetic substrate of IDE, substrate V (7-methoxycoumarin-4-yl-acetyl-RPPGF-SAFK-2,4-dinitrophenyl, R&D Systems), was used to measure the enzymatic activity of IDE on a Tecan Safire microplate reader using an excitation wavelength of 327 nm and emission wavelength of 395 nm (McCord et al., 2013). Reactions were carried out at 37 °C, using 5 μM substrate V in 100 μl of 50 mM potassium phosphate (pH 7.3) with the addition of 0.6 nM IDE in the presence or absence of 12 nM Fab_{H11}. The degradation of substrate V was assessed by monitoring fluorescence increase and the initial

velocity was calculated using linear regression after background subtraction. The standard deviation was derived from three individual experiments.

Crystallography: IDE-CF-E111Q was first incubated with Aβ or insulin in a 1:10 or 1:2 ratio, respectively, at 18 °C overnight (~16-18 h) and IDE-substrate complex was purified using Superdex 200 column. This process was repeated three times. Substrate-bound IDE was then mixed in an equimolar ratio with Fab1 or $Fab1_E$ and substrate- and Fab-bound IDE was purified using Superdex 200 column. The resulting complexes were crystallized in 0.1M sodium cacodylate (pH6.5), 0.2M $MgCl_2$, 10% PEG-3000, and 0.01% ethyl acetate at 18^oC by hanging drop vapor diffusion. Crystals formed within 2-3 days. To crystallize $Fab_{(H11\text{-}E)}$ bound IDE, IDE-CF was purified by Superdex 200 three times before mixing with extra molar $Fab_{H11\text{-}E}$ and $Fab_{H11\text{-}E}$-bound IDE was purified by Superdex 200. Such protein complex was crystallized in 0.088M Ammonium citrate tribasic, pH 7, 10% w/v PEG3350, 0.02M ethylenediaminetetraacetic disodium salt dihydrate at 18^oC by hanging drop vapor diffusion. Crystals formed in about a week. For data collection, crystals were equilibrated in reservoir buffer with 30% glycerol and flash frozen in liquid nitrogen. Diffraction data were collected at 100K on the 19-ID beamline at Argonne National Laboratory. Data sets were processed using HKL2000 and the CCP4 suite. The structures of were determined by molecular replacement. For substrate-bound Fab1-bound IDE structure, the unbound IDE-Fab_1 complex (4IOF) was used as a search model and no NCS average for C2 symmetry of IDE dimer was applied during the refinement to avoid the bias. For the crystal structure of $Fab_{H11\text{-}E}$-bound IDE, the closed-state IDE (2WBY) and Fab in unbound IDE-Fab_1 complex (4IOF) were used as the search model. Model building and refinement were performed by using REFMAC, PHENIX, and COOT (Adams et al., 2011; Emsley et al., 2010b; Potterton et al., 2002). The final model for Aβ-IDE-Fab1 (pdb = 4M1C) has R_{work} = 23% and R_{free} = 27%, that for Insulin-IDE-Fab1 (pdb =5WOB) has R_{work} = 24% and R_{free} = 29% and that for IDE-$Fab_{H11\text{-}E}$ (pdb =5UOC) has R_{work} = 22% and R_{free} = 27%. The data and refinement statistics are listed on **Supplementary file 1**. The key residues involving in the interaction of IDE with $Fab_{H11\text{-}E}$ was calculated using PDBePISA (Krissinel and Henrick, 2007).

CryoEM: Purified wild type IDE was further purified by Superdex 200 chromatography using buffer containing 20 mM HEPES, pH 7.2, 300 mM NaCl, and 20 mM EDTA and then mixed with $Fab_{H11\text{-}E}$ at an equal molar ratio. $Fab_{H11\text{-}E}$-IDE complex was purified by Superdex 200 chromatography in the absence or presence of five-fold molar excess of insulin. Insulin-bound IDE-$Fab_{H11\text{-}E}$ and IDE-$Fab_{H11\text{-}E}$ cryoEM grids were prepared using either a manual plunger or

Spotiton 1.0 (Dandey et al., 2018; Razinkov et al., 2016). For manual plunging, 300 mesh carbon or gold lacey grids, prepared in house (Fukami and Adachi, 1965), were plasma cleaned using O_2 and H_2 for 30 secs using a Solarus plasma cleaner (Gatan). 3µl of sample was applied to the grid and manually blotted with filter paper for 3 secs from the back of the grids followed immediately by plunging into liquid ethane. For Spotiton prepared grids, 300 mesh carbon or gold lacey nanowire grids were plasma cleaned with O_2 and H_2 for 10 secs using a Solarus plasma cleaner (Gatan). 6µl of protein sample was aspirated by the Spotiton piezo tip and about 80 x 50pl of sample was delivered to the grid as it passes the piezo tip en route to being plunged into liquid ethane. All images were acquired using a Titan Krios microscope (FEI) operated at 300KeV with a Gatan K2 direct electron detector (Gatan) in counting mode. Images were automatically acquired using Leginon (Suloway et al., 2005) using collection parameters as shown in **Supplementary file 2**. IDE-$Fab_{H11\text{-}E}$ showed highly preferred orientation in vitreous ice. Thus, images were acquired with the grid tilted at an angle to the electron beam, which allowed better sampling of other orientations (**Figure 2-figure supplement 9B**) (Tan et al., 2017). Images were processed using software integrated into the Appion (Lander et al., 2009) pipeline except where stated. Frames were aligned using MotionCor2 software with dose weighting (Zheng et al., 2017), particles were picked and extracted automatically using DoGpicker (Voss et al., 2009). Particle stacks were then passed to RELION2.1 (Scheres, 2012) and processed through several rounds of 2D and 3D classification. Example images and 2D class averages are shown in **Figure 2-figure supplement 5-7**. Selected classes were then processed for high resolution 3D refinement (**Figure 2-figure supplement 8**). The resolution was further improved by focused classification with signal subtraction. The mask was created in Chimera (Pettersen et al., 2004) with the Fab regions set to value zero and outside Fab regions set to value one. Subsequently the masked refinement was carried out with C1 symmetry using RELION 2.1 (Scheres, 2012). The final resolution was estimated using Fourier Shell Correlation (FSC=0.143) in RELION 2.1 (**Figure 2-figure supplement 9C, 9D**). The anisotropy was analyzed using 3DFSC (Tan et al., 2017). The cryoEM data collection and processing statistics are listed in **Supplementary file 2**. The structural models were built using a combination of high resolution IDE dimer structure (PDB=2cww) and $Fab_{H11\text{-}E}$-bound IDE dimer. The density fitting and structure refinement was done using UCSF CHIMERA (Pettersen et al., 2004), COOT (Emsley and Cowtan, 2004; Emsley et al., 2010b), and PHENIX (Adams et al., 2011). The refinement statistics are listed in **Supplementary file 3**.

SAXS: SAXS data were collected at the BioCAT/18ID beamline at Advanced Photon Source, Argonne National Laboratory (Chicago, USA) (Fischetti et al., 2004) using the photon counting PILATUS 3 1M at room temperature (23^{o}C) and an incident X-ray wavelength of 1.03 Å. The 3.5 m sample-to-detector distance yielded a range of 0.005 – 0.33 Å^{-1} for the momentum transfer ($q = 4\pi \sin\theta/\lambda$ where 2θ is the scattered angle between the incident and scattered beam and λ the X-ray wavelength). For size exclusion chromatography (SEC)-SAXS, 2-3 mg IDE was loaded onto a GE Superdex 200 10/300G in the buffer containing 20 mM Tris, pH 8.0, 100 mM NaCl and the eluates were immediately passed through X-ray beam. To prepare zinc-free catalytic inactive IDE, IDE was first washed with about 2M NaCl and then dialyzed against 500ml 20 mM Tris pH8.0, 100mM NaCl, 20mM EDTA and subsequently purified by Superdex 200 column using the buffer containing 20 mM Tris, pH 8.0, 100 mM NaCl, 20 mM EDTA. Greater than fifteen measurements around IDE protein peak were collected in each run for subsequent analysis. Time-resolved SAXS experiments were done using a microfluidic laminar flow mixer adapted from the design initially made for time resolved fluorescence studies(Park et al., 2008; Park et al., 2006). The mixer chip consisted of 5 inlets: a center channel for IDE solution, two diagonal channels for identical buffers as the IDE solution and two side channels for buffer containing insulin. Syringe pumps (Model 511, New Era Pump Systems Inc., NY, USA) were used to inject sample and buffer solutions continuously into the mixer inlets. Per measurement, 5-10 mg IDE injected from the center channel were compressed into a thin sheet by the diagonal and side channel flows as a result of the hydrodynamic focusing effect. Kinetic reaction was triggered by diffusion of 2-fold molar excess of insulin into the jet of IDE from adjacent flow layers of buffer above and below. The thickness of the sheet was controlled by the flow rate ratios of the inlet channels. The observation channel is 1 mm deep (i.e. X-ray pathlength), 0.2 mm wide and 25 mm long. During the flow experiment, the observation channel was sampled by a grid scan of 10x30 positions and SAXS data was collected at each grid point. The total flow rate determined the maximum accessible time corresponding to the exit end of the observation channel. The time window of 2 second was performed by using the flow rates of 68, 2, 9 µL/min for side, diagonal and center syringe pumps respectively. Increasing the flow rates to 682, 22 and 90 µL/min allows the kinetic study in the time window shorter than 0.2 second. We did three mixing experiments: i) IDE bound with insulin mixing with insulin buffer; ii) IDE mixing with insulin free buffer; and iii) IDE mixing with buffer containing insulin. The mixing experiments i and ii were done using flow rates for 2 s time window while the experiment iii was done for both 2 second and 0.2 second time windows. The

SAXS data reduction and analyses were done using ATSAS package (Petoukhov et al., 2012), PRIMUS (Konarev et al., 2003) and CRYSOL (Svergun et al., 1995). Comparison of experimental scattering profiles with calculated profiles from high resolution atomic models was done using CRYSOL (Svergun et al., 1995). For time-resolved experiments, in order to reduce the effects of the varied parasitic scattering in grid scans, radius of gyration values were obtained using the program GNOM (Petoukhov et al., 2012).

Hydrogen-Deuterium Exchange Mass Spectrometry: Prior to carrying out hydrogen/deuterium exchange experiments, the optimal quench condition that generated the best sequence coverage map of IDE were established as previously described (Marsh et al., 2013). IDE stock solutions were prepared in 8.3 mM Tris-HCl, 50m NaCl, 2.1% DMSO, pH7.2 H_2O buffer by mixing 15 μM of IDE with 30 μM $Fab_{H11\text{-}E}$, 150 μM of Insulin, 150 μM of 6bk, 150 μM of BDM44768 or 300 μM of Aβ, incubating at room temperature for 30 min, then keep on ice for 15 min. Functional hydrogen-deuterium exchange reactions were initiated by dilution of 3 μl of stock solution into 9 μl of D_2O buffer (8.3 mM Tris, 50 mM NaCl, pDREAD 7.2) and incubation at 0 °C. The exchange reactions were quenched after various exchange time points (10, 100, 1000, 10000, 100000 sec at 0 °C, and 100000 sec at RT) by adding 18 μl of ice-cold 0.8% formic acid, 1.6M GuHCl, 16.6% glycerol for a final pH of 2.5. Quenched samples were then immediately frozen on dry ice and stored at -80 °C before LC/MS analysis. Non-deuterated and equilibrium-deuterated control samples are also prepared as previously described (Tsalkova et al., 2012). The frozen samples were thawed automatically on a cryogenic autosampler(Woods and Hamuro, 2001) at 4°C, and digested on an immobilized pepsin column (16 μl bed volume). Proteolytic products were collected on a C18 trap column (Michrom Magic C18 AQ 0.2x1 mm) for 1 min desalting and separated using a reverse phase analytical column (Michrom Magic C18 AQ 0.2 x 50 mm, 3 μM) with a acetonitrile linear gradient (6.4%-38.4% over 30min). MS analysis was performed on an OrbiTrap Elite Mass Spectrometer (ThermoFisher Scientific, San Jose, CA). Instruments settings was optimized to minimize the back-exchange(Walters et al., 2012). The data was acquired in both data-dependent MS/MS mode and MS1 profile mode and Proteome Discoverer software (ThermoFisher) was used to identify proteolytic peptides. The deuterium content of the peptides for each time point was calculated by DXMS Explorer (Sierra Analytics Inc, Modesto, CA), with corrections for back-exchange (Zhang and Smith, 1993). H/D exchange experiments performed using our automated system typically produce deuteron incorporation measurements with a standard deviation of less than 2% of the mean of triplicate

626 determinations (Chang et al., 2015; Hsu et al., 2009a; Hsu et al., 2009b). In the present work,
627 just as in our previous studies, only changes in deuteration level greater than 10% were
628 considered significant (Burke et al., 2009; Hamuro et al., 2004). Heat maps were created using
629 in house program that sub-localize HDX down to smaller fragments using all overlapping
630 peptides.
631 **DATA AND SOFTWARE AVAILABILITY:** The cryoEM maps have been deposited in the
632 Electron Microscopy Data Bank with accession codes EMD-7041, EMD-7092, EMD-7065,
633 EMD-7090, EMD-7062, EMD-7093, EMD-7066, and EMD-7091. The atomic models have
634 been deposited in the Protein Data Bank under accession code EMDB 6B3Q, 6BFC, 6BF8,
635 6B7Y, 6BF6, 6B70, 6BF9, 6B7Z and 6BF7. The crystal structures of Fab1-bound IDE in
636 complex with insulin or Aβ have been deposited in the Protein Data Bank under access code
637 5WOB and 4M1C, respectively. The crystal structure of Fab_1- bound IDE in complex with
638 insulin and Fab_{1E} has been deposited in the Protein Data Bank under access code 5CJO. The
639 crystal structures of IDE in complex with $Fab_{H11\text{-}E}$ has been deposited in the Protein Data Bank
640 under access code 5UOE.
641
642 **Author contributions:** W.-J.T., B.C., C.S.P., and S.L. designed the project. W.G.L. purified
643 protein for EM and conducted negative stained EM data acquisition, L.J.B. screened, purified,
644 and engineered Fab, Z.Z., performed EM grid preparation, data acquisition and processing,
645 assisted by H.W. and Y.Z.T. and overseen by B.C. and C.S.P. W.G.L. and W.-J.T. built and
646 refined cryoEM structural models. W.G.L. and L.A.M. performed protein purification and
647 crystallographic data collection and W.G.L. L.A.M., M.F., A.W., and W.-J. T. built and refined
648 structural models. W.G.L. performed protein purification for HDX-MS, A.W., D.L., and S.L.
649 performed HDX-MS and analysis. W.G.L. purified proteins for SAXS studies and W.G.L. and
650 W.S. performed SAXS studies. R.D.-P., B.D., D.L., A.K., S.K., and A.A.K. provided critical
651 reagents. Z.Z., W.G.L, L.J.B, A.W., S.L., B.C., C.P., and W.-J.T. wrote the manuscript; all
652 authors contributed to manuscript finalization.
653 **Acknowledgements:** We are grateful to Ryan M. Hoffman in Andrew Ward's lab at the
654 Scripps Research Institute for initial negative stained EM data acquisition and analysis, to
655 Srinivas Chakravarthy at BioCAT, APS for assisting with SAXS data collection and analysis, to
656 Juan P. Maianti for synthesizing 6bK, and to Steve Meredith for synthetic Aβ. This work was
657 supported by the NIH grants GM81539 and GM121964 to Wei-Jen Tang, GM103310 to

Bridget Carragher and Clinton S. Potter, Agency for Science, Technology and Research Singapore to Yong Zi Tan, GM103622 to Tom Irving at BioCAT, APS, and DARPA Fold Fx program (N66001-14-2-4053), NIH R35 GM118062, and the Howard Hughes Medical Institute to David Liu. The Simons Electron Microscopy Center is supported by a grant from the Simons Foundation (349247). Use of the Advanced Photon Source was supported by the U.S. Department of Energy, Office of Basic Energy Sciences, under contract No. DE-AC02-06CH11357.

References

Adames, N., Blundell, K., Ashby, M.N., and Boone, C. (1995). Role of Yeast Insulin-Degrading Enzyme Homologs in Propheromone Processing and Bud Site Selection. Science *270*, 464-467.

Adams, P.D., Afonine, P.V., Bunkoczi, G., Chen, V.B., Davis, I.W., Echols, N., Headd, J.J., Hung, L.W., Kapral, G.J., Grosse-Kunstleve, R.W., McCoy, A.J., Moriarty, N.W., Oeffner, R., Read, R.J., Richardson, D.C., Richardson, J.S., Terwilliger, T.C., and Zwart, P.H. (2010). PHENIX: a comprehensive Python-based system for macromolecular structure solution. Acta Crystallogr D Biol Crystallogr *66*, 213-221.

Adams, P.D., Afonine, P.V., Bunkoczi, G., Chen, V.B., Echols, N., Headd, J.J., Hung, L.W., Jain, S., Kapral, G.J., Grosse Kunstleve, R.W., McCoy, A.J., Moriarty, N.W., Oeffner, R.D., Read, R.J., Richardson, D.C., Richardson, J.S., Terwilliger, T.C., and Zwart, P.H. (2011). The Phenix software for automated determination of macromolecular structures. Methods *55*, 94-106.

Bailey, L.J., Sheehy, K.M., Dominik, P.K., Liang, W.G., Rui, H., Clark, M., Jaskolowski, M., Kim, Y., Deneka, D., Tang, W.-J., and Kossiakoff, A.A. (2018). Locking the Elbow: Improved Antibody Fab Fragments as Chaperones for Structure Determination. Journal of Molecular Biology *430*, 337-347.

Bailey, L.J., Sheehy, K.M., Hoey, R.J., Schaefer, Z.P., Ura, M., and Kossiakoff, A.A. (2014). Applications for an engineered Protein-G variant with a pH controllable affinity to antibody fragments. Journal of immunological methods *415*, 24-30.

Blanchet, C.E., and Svergun, D.I. (2013). Small-Angle X-Ray Scattering on Biological Macromolecules and Nanocomposites in Solution. Annu Rev Phys Chem *64*, 37-54.

Burke, J.E., Babakhani, A., Gorfe, A.A., Kokotos, G., Li, S., Woods, V.L., Jr., McCammon, J.A., and Dennis, E.A. (2009). Location of inhibitors bound to group IVA phospholipase A2 determined by molecular dynamics and deuterium exchange mass spectrometry. J Am Chem Soc *131*, 8083-8091.

Chang, Y.G., Cohen, S.E., Phong, C., Myers, W.K., Kim, Y.I., Tseng, R., Lin, J., Zhang, L., Boyd, J.S., Lee, Y., Kang, S., Lee, D., Li, S., Britt, R.D., Rust, M.J., Golden, S.S., and LiWang, A. (2015). A protein fold switch joins the circadian oscillator to clock output in cyanobacteria. Science *349*, 324-328.

Chen, V.B., Arendall, W.B., 3rd, Headd, J.J., Keedy, D.A., Immormino, R.M., Kapral, G.J., Murray, L.W., Richardson, J.S., and Richardson, D.C. (2010). MolProbity: all-atom structure validation for macromolecular crystallography. Acta Crystallogr D Biol Crystallogr *66*, 12-21.

Chiti, F., and Dobson, C.M. (2006). Protein misfolding, functional amyloid, and human disease. Annu Rev Biochem *75*, 333-366.

Chung, K.Y., Rasmussen, S.G.F., Liu, T., Li, S., Devree, B.T., Chae, P.S., Calinski, D., Kobilka, B.K., Woods, V.L., and Sunahara, R.K. (2011). Conformational changes in the G protein Gs induced by the β2 adrenergic receptor. Nature *477*, 611-615.

Dandey, V.P., Wei, H., Zhang, Z., Tan, Y.Z., Acharya, P., Eng, E.T., Rice, W.J., Kahn, P.A., Potter, C.S., and Carragher, B. (2018). Spotiton: new features and applications. J Struct Biol, epub.

Deprez-poulain, R., Hennuyer, N., Bosc, D., Liang, W.G., Enee, E., Marechal, X., Charton, J., Totobenazara, J., Berte, G., Jahklal, J., Verdelet, T., Dumont, J., Dassonneville, S., Woitrain, E., Gauriot, M., Paquet, C., Duplan, I., Hermant, P., Cantrelle, F.-X., Sevin, E., Culot, M., Landry, V., Herledan, A., Piveteau, C., Lippens, G., Leroux, F., Tang, W.-J., van Endert, P.,

712 Staels, B., and Deprez, B. (2015a). Catalytic Site Inhibition of Insulin Degrading Enzyme by a
713 Small Molecule Induces Glucose Intolerance in Mice. Nature Communications *6*, 8250.
714 Deprez-Poulain, R., Hennuyer, N., Bosc, D., Liang, W.G., Enee, E., Marechal, X., Charton, J.,
715 Totobenazara, J., Berte, G., Jahklal, J., Verdelet, T., Dumont, J., Dassonneville, S., Woitrain,
716 E., Gauriot, M., Paquet, C., Duplan, I., Hermant, P., Cantrelle, F.X., Sevin, E., Culot, M.,
717 Landry, V., Herledan, A., Piveteau, C., Lippens, G., Leroux, F., Tang, W.J., van Endert, P.,
718 Staels, B., and Deprez, B. (2015b). Catalytic site inhibition of insulin-degrading enzyme by a
719 small molecule induces glucose intolerance in mice. Nature communications *6*, 8250.
720 Duckworth, W.C., Bennett, R.G., and Hamel, F.G. (1998). Insulin degradation: progress and
721 potential. Endocr Rev *19*, 608-624.
722 Durham, T.B., Toth, J.L., Klimkowski, V.J., Cao, J.X.C., Siesky, A.M., Alexander-Chacko, J.,
723 Wu, G.Y., Dixon, J.T., McGee, J.E., Wang, Y., Guo, S.Y., Cavitt, R.N., Schindler, J.,
724 Thibodeaux, S.J., Calvert, N.A., Coghlan, M.J., Sindelar, D.K., Christe, M., Kiselyov, V.V.,
725 Michael, M.D., and Sloop, K.W. (2015). Dual Exosite-binding Inhibitors of Insulin-degrading
726 Enzyme Challenge Its Role as the Primary Mediator of Insulin Clearance in vivo. J Biol Chem
727 *209*, 20044-20059
728 Eisenberg, D., and Jucker, M. (2012). The Amyloid State of Proteins in Human Diseases. Cell
729 *148*, 1188-1203.
730 Emsley, P., and Cowtan, K. (2004). Coot: model-building tools for molecular graphics. Acta
731 Crystallogr D *60*, 2126-2132.
732 Emsley, P., Lohkamp, B., Scott, W.G., and Cowtan, K. (2010a). Features and development of
733 Coot. Acta Crystallogr D Biol Crystallogr *66*, 486-501.
734 Emsley, P., Lohkamp, B., Scott, W.G., and Cowtan, K. (2010b). Features and development of
735 Coot. Acta Crystallogr D *66*, 486-501.
736 Farris, W., Mansourian, S., Chang, Y., Lindsley, L., Eckman, E.A., Frosch, M.P., Eckman,
737 C.B., Tanzi, R.E., Selkoe, D.J., and Guenette, S. (2003). Insulin-degrading enzyme regulates
738 the levels of insulin, amyloid beta-protein, and the beta-amyloid precursor protein intracellular
739 domain in vivo. Proc Natl Acad Sci USA *100*, 4162-4167.
740 Farris, W., Mansourian, S., Leissring, M.A., Eckman, E.A., Bertram, L., Eckman, C.B., Tanzi,
741 R.E., and Selkoe, D.J. (2004). Partial loss-of-function mutations in insulin-degrading enzyme
742 that induce diabetes also impair degradation of amyloid beta-protein. Am J Pathol *164*, 1425-
743 1434.
744 Fischetti, R., Stepanov, S., Rosenbaum, G., Barrea, R., Black, E., Gore, D., Heurich, R.,
745 Kondrashkina, E., Kropf, A.J., Wang, S., Zhang, K., Irving, T.C., and Bunker, G.B. (2004). The
746 BioCAT undulator beamline 18ID: a facility for biological non-crystalline diffraction and X-ray
747 absorption spectroscopy at the Advanced Photon Source. Journal of synchrotron radiation *11*,
748 399-405.
749 Fitzpatrick, A.W.P., Falcon, B., He, S., Murzin, A.G., Murshudov, G., Garringer, H.J., Crowther,
750 R.A., Ghetti, B., Goedert, M., and Scheres, S.H.W. (2017). Cryo-EM structures of tau filaments
751 from Alzheimer's disease. Nature *547*, 185-190.
752 Fuchsberger, C., Flannick, J., Teslovich, T.M., Mahajan, A., Agarwala, V., Gaulton, K.J., Ma,
753 C., Fontanillas, P., Moutsianas, L., McCarthy, D.J., Rivas, M.A., Perry, J.R., Sim, X., Blackwell,
754 T.W., Robertson, N.R., Rayner, N.W., Cingolani, P., Locke, A.E., Fernandez Tajes, J.,
755 Highland, H.M., Dupuis, J., Chines, P.S., Lindgren, C.M., Hartl, C., Jackson, A.U., Chen, H.,
756 Huyghe, J.R., van de Bunt, M., Pearson, R.D., Kumar, A., Muller-Nurasyid, M., Grarup, N.,
757 Stringham, H.M., Gamazon, E.R., Lee, J., Chen, Y., Scott, R.A., Below, J.E., Chen, P., Huang,
758 J., Go, M.J., Stitzel, M.L., Pasko, D., Parker, S.C., Varga, T.V., Green, T., Beer, N.L., Day-
759 Williams, A.G., Ferreira, T., Fingerlin, T., Horikoshi, M., Hu, C., Huh, I., Ikram, M.K., Kim, B.J.,
760 Kim, Y., Kim, Y.J., Kwon, M.S., Lee, J., Lee, S., Lin, K.H., Maxwell, T.J., Nagai, Y., Wang, X.,

Welch, R.P., Yoon, J., Zhang, W., Barzilai, N., Voight, B.F., Han, B.G., Jenkinson, C.P., Kuulasmaa, T., Kuusisto, J., Manning, A., Ng, M.C., Palmer, N.D., Balkau, B., Stancakova, A., Abboud, H.E., Boeing, H., Giedraitis, V., Prabhakaran, D., Gottesman, O., Scott, J., Carey, J., Kwan, P., Grant, G., Smith, J.D., Neale, B.M., Purcell, S., Butterworth, A.S., Howson, J.M., Lee, H.M., Lu, Y., Kwak, S.H., Zhao, W., Danesh, J., Lam, V.K., Park, K.S., Saleheen, D., So, W.Y., Tam, C.H., Afzal, U., Aguilar, D., Arya, R., Aung, T., Chan, E., Navarro, C., Cheng, C.Y., Palli, D., Correa, A., Curran, J.E., Rybin, D., Farook, V.S., Fowler, S.P., Freedman, B.I., Griswold, M., Hale, D.E., Hicks, P.J., Khor, C.C., Kumar, S., Lehne, B., Thuillier, D., Lim, W.Y., Liu, J., van der Schouw, Y.T., Loh, M., Musani, S.K., Puppala, S., Scott, W.R., Yengo, L., Tan, S.T., Taylor, H.A., Jr., Thameem, F., Wilson, G., Sr., Wong, T.Y., Njolstad, P.R., Levy, J.C., Mangino, M., Bonnycastle, L.L., Schwarzmayr, T., Fadista, J., Surdulescu, G.L., Herder, C., Groves, C.J., Wieland, T., Bork-Jensen, J., Brandslund, I., Christensen, C., Koistinen, H.A., Doney, A.S., Kinnunen, L., Esko, T., Farmer, A.J., Hakaste, L., Hodgkiss, D., Kravic, J., Lyssenko, V., Hollensted, M., Jorgensen, M.E., Jorgensen, T., Ladenvall, C., Justesen, J.M., Karajamaki, A., Kriebel, J., Rathmann, W., Lannfelt, L., Lauritzen, T., Narisu, N., Linneberg, A., Melander, O., Milani, L., Neville, M., Orho-Melander, M., Qi, L., Qi, Q., Roden, M., Rolandsson, O., Swift, A., Rosengren, A.H., Stirrups, K., Wood, A.R., Mihailov, E., Blancher, C., Carneiro, M.O., Maguire, J., Poplin, R., Shakir, K., Fennell, T., DePristo, M., Hrabe de Angelis, M., Deloukas, P., Gjesing, A.P., Jun, G., Nilsson, P., Murphy, J., Onofrio, R., Thorand, B., Hansen, T., Meisinger, C., Hu, F.B., Isomaa, B., Karpe, F., Liang, L., Peters, A., Huth, C., O'Rahilly, S.P., Palmer, C.N., Pedersen, O., Rauramaa, R., Tuomilehto, J., Salomaa, V., Watanabe, R.M., Syvanen, A.C., Bergman, R.N., Bharadwaj, D., Bottinger, E.P., Cho, Y.S., Chandak, G.R., Chan, J.C., Chia, K.S., Daly, M.J., Ebrahim, S.B., Langenberg, C., Elliott, P., Jablonski, K.A., Lehman, D.M., Jia, W., Ma, R.C., Pollin, T.I., Sandhu, M., Tandon, N., Froguel, P., Barroso, I., Teo, Y.Y., Zeggini, E., Loos, R.J., Small, K.S., Ried, J.S., DeFronzo, R.A., Grallert, H., Glaser, B., Metspalu, A., Wareham, N.J., Walker, M., Banks, E., Gieger, C., Ingelsson, E., Im, H.K., Illig, T., Franks, P.W., Buck, G., Trakalo, J., Buck, D., Prokopenko, I., Magi, R., Lind, L., Farjoun, Y., Owen, K.R., Gloyn, A.L., Strauch, K., Tuomi, T., Kooner, J.S., Lee, J.Y., Park, T., Donnelly, P., Morris, A.D., Hattersley, A.T., Bowden, D.W., Collins, F.S., Atzmon, G., Chambers, J.C., Spector, T.D., Laakso, M., Strom, T.M., Bell, G.I., Blangero, J., Duggirala, R., Tai, E.S., McVean, G., Hanis, C.L., Wilson, J.G., Seielstad, M., Frayling, T.M., Meigs, J.B., Cox, N.J., Sladek, R., Lander, E.S., Gabriel, S., Burtt, N.P., Mohlke, K.L., Meitinger, T., Groop, L., Abecasis, G., Florez, J.C., Scott, L.J., Morris, A.P., Kang, H.M., Boehnke, M., Altshuler, D., and McCarthy, M.I. (2016). The genetic architecture of type 2 diabetes. Nature *536*, 41-47.

Fujita, A., Oka, C., Arikawa, Y., Katagai, T., Tonouchi, A., Kuhara, S., and Misumi, Y. (1994). A Yeast Gene Necessary for Bud-Site Selection Encodes a Protein Similar to Insulin-Degrading Enzymes. Nature *372*, 567-570.

Fukami, A., and Adachi, K. (1965). A new method of preparation of a self-perforated micro plastic grid and its application. J Electron Microsc (Tokyo) *14*, 112-118.

Galagovsky, D., Katz, M.J., Acevedo, J.M., Sorianello, E., Glavic, A., and Wappner, P. (2014). The Drosophila insulin-degrading enzyme restricts growth by modulating the PI3K pathway in a cell-autonomous manner. Mol Biol Cell *25*, 916-924.

Goddard, T.D., Huang, C.C., Meng, E.C., Pettersen, E.F., Couch, G.S., Morris, J.H., and Ferrin, T.E. (2017). UCSF ChimeraX: Meeting modern challenges in visualization and analysis. Protein science : a publication of the Protein Society.

Guo, Q., Manolopoulou, M., Bian, Y., Schilling, A.B., and Tang, W.J. (2010). Molecular basis for the recognition and cleavages of IGF-II, TGF-alpha, and amylin by human insulin-degrading enzyme. J Mol Biol *395*, 430-443.

Hamuro, Y., Anand, G.S., Kim, J.S., Juliano, C., Stranz, D.D., Taylor, S.S., and Woods, V.L., Jr. (2004). Mapping intersubunit interactions of the regulatory subunit (RIalpha) in the type I holoenzyme of protein kinase A by amide hydrogen/deuterium exchange mass spectrometry (DXMS). J Mol Biol *340*, 1185-1196.
Henderson, R. (2015). Overview and future of single particle electron cryomicroscopy. Arch Biochem Biophys *581*, 19-24.
Hsu, S., Kim, Y., Li, S., Durrant, E.S., Pace, R.M., Woods, V.L., and Gentry, M.S. (2009a). Structural Insights into Glucan Phosphatase Dynamics Using Amide Hydrogen-Deuterium Exchange Mass Spectrometry. Biochemistry *48*, 9891-9902.
Hsu, Y.H., Burke, J.E., Li, S., Woods, V.L., and Dennis, E.A. (2009b). Localizing the Membrane Binding Region of Group VIA Ca2+-independent Phospholipase A(2) Using Peptide Amide Hydrogen/Deuterium Exchange Mass Spectrometry. Journal of Biological Chemistry *284*, 23652-23661.
Jucker, M., and Walker, L.C. (2013). Self-propagation of pathogenic protein aggregates in neurodegenerative diseases. Nature *501*, 45-51.
Kim, J.M., Wu, S.P., Tomasiak, T.M., Mergel, C., Winter, M.B., Stiller, S.B., Robles-Colmanares, Y., Stroud, R.M., Tampe, R., Craik, C.S., and Cheng, Y.F. (2015). Subnanometre-resolution electron cryomicroscopy structure of a heterodimeric ABC exporter. Nature *517*, 396-U598.
King, J.V., Liang, W.G., Scherpelz, K.P., Schilling, A.B., Meredith, S.C., and Tang, W.-J. (2014). Molecular Basis of Substrate Recognition and Degradation by Human Presequence Protease. Structure *22*, 996-1007.
Koide, A., Wojcik, J., Gilbreth, R.N., Hoey, R.J., and Koide, S. (2012). Teaching an Old Scaffold New Tricks: Monobodies Constructed Using Alternative Surfaces of the FN3 Scaffold. J Mol Biol *415*, 393-405.
Konarev, P.V., Volkov, V.V., Sokolova, A.V., Koch, M.H., and Svergun, D.I. (2003). PRIMUS: a Windows PC-based system for small-angle scattering data analysis. Journal of applied crystallography *36*, 1277-1282.
Krissinel, E., and Henrick, K. (2007). Inference of macromolecular assemblies from crystalline state. J Mol Biol *372*, 774-797.
Kurochkin, I.V. (2001). Insulin-degrading enzyme: embarking on amyloid destruction. Trends Biochem Sci *26*, 421-425.
Kurochkin, I.V., Guarnera, E., and Berezovsky, I.N. (2018). Insulin-Degrading Enzyme in the Fight against Alzheimer's Disease. Trends Pharmacol Sci *39*, 49-58.
Lander, G.C., Stagg, S.M., Voss, N.R., Cheng, A., Fellmann, D., Pulokas, J., Yoshioka, C., Irving, C., Mulder, A., Lau, P.W., Lyumkis, D., Potter, C.S., and Carragher, B. (2009). Appion: an integrated, database-driven pipeline to facilitate EM image processing. J Struct Biol *166*, 95-102.
Leissring, M.A., Farris, W., Chang, A.Y., Walsh, D.M., Wu, X., Sun, X., Frosch, M.P., and Selkoe, D.J. (2003). Enhanced proteolysis of beta-amyloid in APP transgenic mice prevents plaque formation, secondary pathology, and premature death. Neuron *40*, 1087-1093.
Li, P., Kuo, W.L., Yousef, M., Rosner, M.R., and Tang, W.J. (2006). The C-terminal domain of human insulin degrading enzyme is required for dimerization and substrate recognition. Biochem Biophys Res Commun *343*, 1032-1037.
Li, S.S., Tsalkova, T.T., White, M.A.M., Mei, F.C.F., Liu, T.T., Wang, D.D., Woods, V.L.V., and Cheng, X.X. (2011). Mechanism of intracellular cAMP sensor Epac2 activation: cAMP-induced conformational changes identified by amide hydrogen/deuterium exchange mass spectrometry (DXMS). The Journal of biological chemistry *286*, 17889-17897.

Li, X., Mooney, P., Zheng, S., Booth, C.R., Braunfeld, M.B., Gubbens, S., Agard, D.A., and Cheng, Y. (2013). Electron counting and beam-induced motion correction enable near-atomic-resolution single-particle cryo-EM. Nat Methods *10*, 584-590.
Lu, J.X., Qiang, W., Yau, W.M., Schwieters, C.D., Meredith, S.C., and Tycko, R. (2013). Molecular Structure of beta-Amyloid Fibrils in Alzheimer's Disease Brain Tissue. Cell *154*, 1257-1268.
Lyumkis, D., Julien, J.P., de Val, N., Cupo, A., Potter, C.S., Klasse, P.J., Burton, D.R., Sanders, R.W., Moore, J.P., Carragher, B., Wilson, I.A., and Ward, A.B. (2013). Cryo-EM Structure of a Fully Glycosylated Soluble Cleaved HIV-1 Envelope Trimer. Science *342*, 1484-1490.
Maianti, J.P., McFedries, A., Foda, Z.H., Kleiner, R.E., Du, X.Q., Leissring, M.A., Tang, W.-J., Charron, M.J., Seeliger, M.A., Saghatelian, A., and Liu, D.R. (2014). Anti-diabetic activity of insulin-degrading enzyme inhibitors mediated by multiple hormones. Nature *511*, 94-98.
Malito, E., Hulse, R.E., and Tang, W.J. (2008a). Amyloid β-degrading cryptidases: insulin degrading enzyme, presequence peptidase, and neprilysin. Cell Mol Life Sci *65*, 2574-2585.
Malito, E., Ralat, L.A., Manolopoulou, M., Tsay, J.L., Wadlington, N.L., and Tang, W.J. (2008b). Molecular bases for the recognition of short peptide substrates and cysteine-directed modifications of human insulin-degrading enzyme. Biochemistry *47*, 12822-12834.
Manolopoulou, M., Guo, Q., Malito, E., Schilling, A.B., and Tang, W.J. (2009). Molecular basis of catalytic chamber-assisted unfolding and cleavage of human insulin by human insulin-degrading enzyme. J Biol Chem *284*, 14177-14188.
Marciano, D.P., Dharmarajan, V., and Griffin, P.R. (2014). HDX-MS guided drug discovery: small molecules and biopharmaceuticals. Current opinion in structural biology *28*, 105-111.
Marsh, J.J., Guan, H.S., Li, S., Chiles, P.G., Tran, D., and Morris, T.A. (2013). Structural Insights into Fibrinogen Dynamics Using Amide Hydrogen/Deuterium Exchange Mass Spectrometry. Biochemistry *52*, 5491-5502.
McCord, L.A., Liang, W.G., Dowdell, E., Kalas, V., Hoey, R.J., Koide, A., Koide, S., and Tang, W.-J. (2013). Conformational states and recognition of amyloidogenic peptides of human insulin-degrading enzyme. Proceedings of the National Academy of Sciences of the United States of America *110*, 13827-13832.
McCoy, A.J., Grosse-Kunstleve, R.W., Adams, P.D., Winn, M.D., Storoni, L.C., and Read, R.J. (2007). Phaser crystallographic software. Journal of applied crystallography *40*, 658-674.
Merk, A., Bartesaghi, A., Banerjee, S., Falconieri, V., Rao, P., Davis, M.I., Pragani, R., Boxer, M.B., Earl, L.A., Milne, J.L.S., and Subramaniam, S. (2016). Breaking Cryo-EM Resolution Barriers to Facilitate Drug Discovery. Cell *165*, 1698-1707.
Merlini, G., and Bellotti, V. (2003). Molecular mechanisms of amyloidosis. New Engl J Med *349*, 583-596.
Miller, K.R., Koide, A., Leung, B., Fitzsimmons, J., Yoder, B., Yuan, H., Jay, M., Sidhu, S.S., Koide, S., and Collins, E.J. (2012). T cell receptor-like recognition of tumor in vivo by synthetic antibody fragment. PLoS One *7*, e43746.
Noinaj, N., Bhasin, S.K., Song, E.S., Scoggin, K.E., Juliano, M.A., Juliano, L., Hersh, L.B., and Rodgers, D.W. (2011). Identification of the allosteric regulatory site of insulysin. PloS one *6*, e20864.
Park, H.Y., Kim, S.A., Korlach, J., Rhoades, E., Kwok, L.W., Zipfell, W.R., Waxham, M.N., Webb, W.W., and Pollack, L. (2008). Conformational changes of calmodulin upon Ca2+ binding studied with a microfluidic mixer. Proceedings of the National Academy of Sciences of the United States of America *105*, 542-547.

Park, H.Y., Qiu, X.Y., Rhoades, E., Korlach, J., Kwok, L.W., Zipfel, W.R., Webb, W.W., and Pollack, L. (2006). Achieving uniform mixing in a microfluidic device: Hydrodynamic focusing prior to mixing. Anal Chem *78*, 4465-4473.
Petoukhov, M.V., Franke, D., Shkumatov, A.V., Tria, G., Kikhney, A.G., Gajda, M., Gorba, C., Mertens, H.D., Konarev, P.V., and Svergun, D.I. (2012). New developments in the program package for small-angle scattering data analysis. Journal of applied crystallography *45*, 342-350.
Pettersen, E.F., Goddard, T.D., Huang, C.C., Couch, G.S., Greenblatt, D.M., Meng, E.C., and Ferrin, T.E. (2004). UCSF chimera - A visualization system for exploratory research and analysis. Journal of computational chemistry *25*, 1605-1612.
Pivovarova, O., Hohn, A., Grune, T., Pfeiffer, A.F.H., and Rudovich, N. (2016). Insulin-degrading enzyme: new therapeutic target for diabetes and Alzheimer's disease? Ann Med *48*, 614-624.
Potterton, E., McNicholas, S., Krissinel, E., Cowtan, K., and Noble, M. (2002). The CCP4 molecular-graphics project. Acta crystallographica Section D, Biological crystallography *58*, 1955-1957.
Putnam, C.D., Hammel, M., Hura, G.L., and Tainer, J.A. (2007). X-ray solution scattering (SAXS) combined with crystallography and computation: defining accurate macromolecular structures, conformations and assemblies in solution. Q Rev Biophys *40*, 191-285.
Ralat, L.A., Guo, Q., Ren, M., Funke, T., Dickey, D.M., Potter, L.R., and Tang, W.J. (2011). Insulin-degrading enzyme modulates the natriuretic peptide-mediated signaling response. J Biol Chem *286*, 4670-4679.
Razinkov, I., Dandey, V.P., Wei, H., Zhang, Z.N., Melnekoff, D., Rice, W.J., Wigge, C., Potter, C.S., and Carragher, B. (2016). A new method for vitrifying samples for cryoEM. Journal of Structural Biology *195*, 190-198.
Ren, M., Guo, Q., Guo, L., Lenz, M., Qian, F., Koenen, R.R., Xu, H., Schilling, A.B., Weber, C., Ye, R.D., Dinner, A.R., and Tang, W.J. (2010). Polymerization of MIP-1 chemokine (CCL3 and CCL4) and clearance of MIP-1 by insulin-degrading enzyme. EMBO J *29*, 3952-3966.
Russo, C.J., and Passmore, L.A. (2014). Electron microscopy: Ultrastable gold substrates for electron cryomicroscopy. Science *346*, 1377-1380.
Scheres, S.H. (2012). RELION: implementation of a Bayesian approach to cryo-EM structure determination. J Struct Biol *180*, 519-530.
Sharma, S.K., Chorell, E., Steneberg, P., Vernersson-Lindahl, E., Edlund, H., and Wittung-Stafshede, P. (2015). Insulin-degrading enzyme prevents alpha-synuclein fibril formation in a nonproteolytical manner. Sci Rep *5*, 12531.
Shen, Y., Joachimiak, A., Rosner, M.R., and Tang, W.J. (2006). Structures of human insulin-degrading enzyme reveal a new substrate recognition mechanism. Nature *443*, 870-874.
Sohma, Y., Sasaki, M., Hayashi, Y., Kimura, T., and Kiso, Y. (2004). Design and synthesis of a novel water-soluble Aβ1-42 isopeptide: an efficient strategy for the preparation of Alzheimer's disease-related peptide, Aβ1-42, via O-N intramolecular acyl migration reaction. Tetrahedron Lett *45*, 5965-5968.
Song, E.S., Juliano, M.A., Juliano, L., and Hersh, L.B. (2003). Substrate activation of insulin-degrading enzyme (insulysin). A potential target for drug development. J Biol Chem *278*, 49789-49794.
Song, E.S., Rodgers, D.W., and Hersh, L.B. (2010). A monomeric variant of insulin degrading enzyme (IDE) loses its regulatory properties. PLoS One *5*, e9719.
Suloway, C., Pulokas, J., Fellmann, D., Cheng, A., Guerra, F., Quispe, J., Stagg, S., Potter, C.S., and Carragher, B. (2005). Automated molecular microscopy: the new Leginon system. J Struct Biol *151*, 41-60.

Svergun, D., Barberato, C., and Koch, M. (1995). CRYSOL-a program to evaluate X-ray solution scattering of biological macromolecules from atomic coordinates. Journal of applied crystallography *28*, 768-773.
Svergun, D.I. (1992). Determination of the Regularization Parameter in Indirect-Transform Methods Using Perceptual Criteria. Journal of applied crystallography *25*, 495-503.
Tan, Y.Z., Baldwin, P.R., Davis, J.H., Williamson, J.R., Potter, C.S., Carragher, B., and Lyumkis, D. (2017). Addressing preferred specimen orientation in single-particle cryo-EM through tilting. Nat Methods *14*, 793-796.
Tang, W.J. (2016). Targeting Insulin-Degrading Enzyme to Treat Type 2 Diabetes Mellitus. Trends Endocrin Met *27*, 24-34.
Tsalkova, T., Mei, F.C., Li, S., Chepurny, O.G., Leech, C.A., Liu, T., Holz, G.G., Woods, V.L., and Cheng, X.D. (2012). Isoform-specific antagonists of exchange proteins directly activated by cAMP. Proceedings of the National Academy of Sciences of the United States of America *109*, 18613-18618.
Tundo, G.R., Sbardella, D., Ciaccio, C., Grasso, G., Gioia, M., Coletta, A., Polticelli, F., Di Pierro, D., Milardi, D., Van Endert, P., Marini, S., and Coletta, M. (2017). Multiple functions of insulin-degrading enzyme: a metabolic crosslight? Critical Reviews in Biochemistry and Molecular Biology, 1-29.
Voss, N.R., Yoshioka, C.K., Radermacher, M., Potter, C.S., and Carragher, B. (2009). DoG Picker and TiltPicker: software tools to facilitate particle selection in single particle electron microscopy. J Struct Biol *166*, 205-213.
Walters, B.T., Ricciuti, A., Mayne, L., and Englander, S.W. (2012). Minimizing back exchange in the hydrogen exchange-mass spectrometry experiment. J Am Soc Mass Spectrom *23*, 2132-2139.
Ward, A.B., Sali, A., and Wilson, I.A. (2013). Biochemistry. Integrative structural biology. Science *339*, 913-915.
Wei, H., Mo, J., Tao, L., Russell, R.J., Tymiak, A.A., Chen, G., Iacob, R.E., and Engen, J.R. (2014). Hydrogen/deuterium exchange mass spectrometry for probing higher order structure of protein therapeutics: methodology and applications. Drug Discov Today *19*, 95-102.
Woods, V.L., and Hamuro, Y. (2001). High resolution, high-throughput amide deuterium exchange-mass spectrometry (DXMS) determination of protein binding site structure and dynamics: Utility in pharmaceutical design. J Cell Biochem *84*, 89-98.
Wu, S., Avila-Sakar, A., Kim, J., Booth, D.S., Greenberg, C.H., Rossi, A., Liao, M., Li, X., Alian, A., Griner, S.L., Juge, N., Yu, Y., Mergel, C.M., Chaparro-Riggers, J., Strop, P., Tampé, R., Edwards, R.H., Stroud, R.M., Craik, C.S., and Cheng, Y. (2012). Fabs enable single particle cryoEM studies of small proteins. Structure *20*, 582-592.
Zhang, X., Hoey, R.J., Lin, G., Koide, A., Leung, B., Ahn, K., Dolios, G., Paduch, M., Ikeuchi, T., Wang, R., Li, Y.M., Koide, S., and Sisodia, S.S. (2012). Identification of a tetratricopeptide repeat-like domain in the nicastrin subunit of gamma-secretase using synthetic antibodies. Proc Natl Acad Sci USA *109*, 8534-8539.
Zhang, Z., and Smith, D.L. (1993). Determination of amide hydrogen exchange by mass spectrometry: a new tool for protein structure elucidation. Protein science : a publication of the Protein Society *2*, 522-531.
Zheng, S., Polovcak, E., Armache, J.P., Cheng, Y., and Agard, D. (2017). Anisotropic Correction of Beam-induced Motion for Improved Single-particle Electron Cryomicroscopy. Nat Methods *14*, 331-332.

1001

Figure legends

Figure 1 Summary of key unsolved IDE structures. (A) Schematic diagram for the catalytic cycle of IDE. IDE is dimerized via the interaction of IDE-C domains. The open-closed transition of IDE dimer is postulated to be mediated by the rigid-body motion between IDE-N and IDE-C. The binding of substrate, e.g., insulin shifts the equilibrium from favoring the open-state IDE to predominantly closed-state IDE. Until now, the structure of open-state IDE has not been determined. (B) Ribbon representation of IDE dimer (PDB code: 2WBY). IDE-N and IDE-C are colored in cyan and grey, respectively. The IDE door subdomain that contains the catalytic zinc ion is highlighted in red and the partially unfolded insulin entrapped inside the catalytic chamber of IDE is colored in yellow. (C) The key conformational switches required for insulin unfolding and degradation by IDE. Insulin A and B chains in ribbon representation are colored in magenta and cyan, respectively. Top: Insulin alone structure where the intra- and inter-molecular disulfide bonds are marked by arrows. Middle: IDE-bound insulin structure that contains partially unfolded insulin (PDB code: 2WBY). The N-terminus binding exosite (Exo) and catalytic zinc ion are marked by arrows. Until now, the structure of IDE in complex with the fully unfolded or cleaved insulin is not determined.

Figure 2 Structures of IDE-Fab$_{(H11)}$-bound IDE dimer. (A) Overall structure of Fab$_{H11\text{-}E}$ bound IDE dimer in ribbon representation (PDB code: 5UOE). IDE-N and IDE-C are colored in cyan and grey, respectively; The heavy and light chains of Fab$_{H11\text{-}E}$ are colored in orange and purple, respectively. (B) Detailed interactions between IDE and Fab$_{H11\text{-}E}$. The key residues involved in the interaction of IDE with Fab$_{H11}$ were calculated using PDBePISA (Krissinel and Henrick, 2007). (C) Changes of hydrogen/deuterium exchange of IDE induced by the binding of Fab$_{H11\text{-}E}$. Representative 2D class averages of (D) insulin-bound IDE-Fab$_{H11\text{-}E}$, (E) Apo IDE-Fab$_{H11\text{-}E}$-bound IDE from untilted micrographs, and (F) Apo IDE-Fab$_{H11\text{-}E}$-bound IDE from 30 degree titled micrographs. (G) Electron density map of IDE-Fab$_{H11\text{-}E}$-bound IDE dimer in the presence of insulin.

Figure 3 CryoEM IDE dimer. (A) Overall structures of IDE dimer in the presence and absence of insulin, Models are shown as ribbons within the electron density map. O, open state; pO, partially-open state; pC, partially-closed state. IDE-N and IDE-C are colored in cyan and grey, respectively; insulin inside the catalytic chamber of IDE is colored in yellow. For simplicity, Fab is not shown. (B) Comparison of four distinct conformational states within IDE structures; two pC states in the insulin-bound cryoEM IDE structure, three pO and three O states in apo-IDE cryoEM structures, and a closed structure from previous crystallographic work (Guo et al., 2010; Malito et al., 2008b; Manolopoulou et al., 2009; Noinaj et al., 2011; Ren et al., 2010; Shen et al., 2006). The buried surface between IDE-N and IDE-C, distance between the center of mass (COM) of IDE D1 and D4 domains, and dihedral angles (absolute values) between COM of IDE D1-D2 and COM of D3-D4 are shown below the ribbon presentation of IDE structures. (C) Structural comparison of IDE states aligned by IDE-N (top) or IDE-C (bottom), showing rigid body motion of IDE-N and IDE-C guided by the loop connecting IDE-N and IDE-C. (D) Structural basis of IDE open structure primed to capture insulin by size and charge complementarity. The boundaries for the substrate-binding catalytic chambers of IDE-N and IDE-C are marked by a dashed line. The color scale is set from -3 kT/e (red) to 3 kT/e (blue) calculated using APBS 2.1.

Figure 4 Insulin-induced conformational changes of IDE revealed by SAXS. (A) Scattering curves from SEC-SAXS analysis using 2-3 mg IDE in the presence (left) or absence (right) of 4-fold molar excess of insulin. Solid red and blue lines represent the predicted SAXS curves based on indicated IDE structures. (B) Time-resolved SAXS analysis of IDE-insulin interaction. Rapid mixing of IDE with insulin resulted in time-dependent reduction of R_g with τ = 0.1 sec.

Figure 5 Conformational dynamics of IDE door domain. (A) Comparison of crystal structures of Fab1-bound IDE alone (PDB code: 4IDF), Fab1- and Aβ-bound IDE (PDB code: 4MIC) and Fab1- and insulin-bound IDE (PDB code: 5WOB). For simplicity, only the subunit of the dimeric IDE that has the profound change in IDE door subdomain is shown and Fab1 is not

shown. (B) Thermal B factors of two IDE subunits within cryoEM IDE dimer structures of insulin-bound pC/pC state IDE (PDB code: 6B3Q) and pO/O apo-state IDE (PDB code: 6BF8). Averaged B factors of IDE door and D3 are shown for comparison. For simplicity, $Fab_{H11\text{-}E}$ is not shown. (C, D) Changes in H/D exchange of IDE induced by inhibitors, BDM44768 and 6bK. The changes in H/D are mapped and the progress curve of regions with significant changes are shown.

Figure 6 Substrate-induced changes in H/D exchange of IDE. (A) Major changes in H/D exchange of IDE induced by insulin. Changes in H/D are mapped onto IDE structure and the progress curve of regions with significant changes are shown. (B) Major changes in H/D exchange of IDE induced by Aβ.

Figure 7 The interaction of IDE with insulin. (A) Cleavage sites of insulin by IDE. The initial cleavages and resulting fragments are shown. The red X marks the scissile bond revealed by insulin bound IDE structures. (B) CryoEM structure of unfolded insulin inside IDE. The fitting of electron density at the catalytic sites with either insulin A (PDB code: 6B3Q) or B chain (PDB code: 6BFC) are shown. For simplicity, $Fab_{H11\text{-}E}$ is not shown. (C) Structure of unfolded insulin inside IDE from insulin bound IDE-Fab1 complex (PDB code: 5WOB). For simplicity, only the fitting of insulin A chain is shown.

Figure 8 Models for IDE catalytic cycle. (A) Model for conformational changes of insulin inside IDE chamber. Structure of partially unfolded insulin at the IDE catalytic chamber is from PDB code 2WBY while those with unfolded insulin are from PDB code 6B3Q and 6BFC for insulin A and B chain at IDE catalytic site. (B) A model for IDE conformational states relevant to substrate capture and catalysis. For simplicity, only the capture and catalysis of the dominant IDE conformational state, pO/O, is shown. The conformational change of the other IDE subunit allosterically regulated by insulin binding to the open-state IDE within an IDE dimer depicted by movie S3 is not shown. The electrostatic surface potential of IDE is set from -5

kT/e (red) to 5 kT/e (blue) and calculated by UCSF Chimera, and the section interface is colored as grey.

Figure supplement legends

Figure 2-Figure supplement 1 Characterization of IDE-Fab$_{(H11)}$. (A) Sequence of 4 CDRs (H1, H2, H3, L3) of Fab$_{H11}$. (B) Representative SPR sensorgram on Fab$_{H11}$ binding to immobilized IDE. The k_{on} and k_{off} were estimated to be $1.6x10^5$ $M^{-1}s^{-1}$ and $1.1x10^{-4}$ s^{-1}, respectively. (C) Relative catalytic activity of IDE in the presence and absence of Fab$_{H11-E}$ using a model fluorogenic substrate, substrate V. The standard deviation is derived from three experiments. (D) Alignment of IDE from IDE-Fab$_{(H11-E)}$ complex (colored green; PDB code: 5UOE) with that from bradykinin-bound IDE structure (colored blue; PDB code: 3CWW). The RMSD is 0.36Å.

Figure 2-Figure supplement 2 Pepsin digestion maps of IDE for HDX-MS analysis.

Figure 2-Figure supplement 3 Amide hydrogen-deuterium exchange profiles of IDE alone (A) and IDE in the presence of Fab-$_{H11}$ (B). The percentages of deuteration levels of each peptide fragment at various time points are shown as a heat map color-coded from blue (<10%) to red (>90%), as indicated at the bottom right of the figure. Each block represents a peptide segment analyzed at each of the six time points (from top to bottom: 10, 100, 1,000, 10,000, 100,000, and 1000,000 seconds). Proline residues, and regions with no amide exchange data available are colored in gray. The structure features of IDE are shown above IDE sequences and colored according to their domains/subdomains.

Figure 2-Figure supplement 4 HDX-MS analysis of IDE-Fab$_{H11}$ interaction. Differences in deuteration levels in the free and Fab$_{H11}$-bound IDE at various time points (from top to bottom: 10, 100, 1,000, 10,000, 100,000, and 1000,000 seconds) are shown in a color-coded bar ranging from blue (-50%) to red (50%), as indicated at the bottom right of the figure. The structure features of IDE are shown above IDE sequences and colored according to their domains/subdomains.

Figure 2-Figure supplement 5 Cryo-electron micrographs and 2D class averages of insulin-bound IDE-Fab$_{H11-E}$. A) Insulin bound IDE-Fab$_{H11-E}$ images with 3.04 μm (left micrograph) and 3.45 μm (right micrograph) defocus. Representative particles indicated in red circles are shown at higher resolution as insets. B) Fourier transform of the corresponding

image, showing Thon rings going out to 3.1 Angstrom. C) 2D class averages of insulin-bound IDE-$Fab_{H11\text{-}E}$ particles using Relion2.1 and the option to ignore the CTFs until the first peak.

Figure 2-Figure supplement 6 Cryo-electron micrographs and 2D class averages of untilted Apo IDE-$Fab_{H11\text{-}E}$. (A) Untilted apo IDE-$Fab_{H11\text{-}E}$ images with 2.56 µm (left micrograph) and 3.05 µm (right micrograph) defocus. (B) 2D class averages of Apo IDE-$Fab_{H11\text{-}E}$ particles from untilted micrographs using Relion2.1 and the option to ignore the CTFs until the first peak.

Figure 2-Figure supplement 7 Cryo-electron micrographs and 2D class averages of tilted Apo IDE-$Fab_{H11\text{-}E}$. (A) Tilted apo IDE-$Fab_{H11\text{-}E}$ images with 3.51 µm (left micrograph) and 3.54 µm (right micrograph) defocus. (B) 2D class averages of Apo IDE-$Fab_{H11\text{-}E}$ particles from 30 degree tilted micrographs using Relion2.1 and the option to ignore the CTFs until the first peak.

Figure 2-Figure supplement 8 Flow chart of cryoEM data processing. The particle numbers for the final 3D classification, focused classification with signal subtraction and final refinement are indicated. A) Apo IDE-$Fab_{H11\text{-}E}$. Particles from both tilted and untilted micrographs were automatically picked using DoGpicker followed by several rounds of 2D and 3D classification using RELION2.1. Bad 2D class averages were discarded. The particles were then selected for 3D refinement followed by focused classification with signal subtraction on the IDE dimer. The classes particles having the same conformation were grouped (dashed line) into three different subsets. Each subset of particles was refined independently. B) Insulin-bound IDE-$Fab_{H11\text{-}E}$. Particles were automatically picked using DoGpicker followed by several rounds of 2D and 3D classification using RELION2.1. The particles were then selected for 3D refinement followed by focused classification with signal subtraction on IDE dimer. The classes particles having the same conformation were grouped together (dashed line) and refined.

Figure 2-Figure supplement 9 CryoEM statistics of apo IDE-$Fab_{H11\text{-}E}$ and insulin bound IDE-$Fab_{H11\text{-}E}$. A) Final refined map colored according to local resolution generated from ResMap. B) Angular distribution plots generated from RELION2.1. C) FSC plot and resolution estimation using the gold-standard 0.143 criterion generated from RELION2.1. D) 3DFSC

plots. The global half-map FSC (solid red line) and the spread of directional resolution values defined by ±1σ from the mean (green area encompassed by dotted green lines, left axis) and a histogram of directional FSC sampled over the 3D FSC (blue bars, right axis).

Figure 2-Figure supplement 10 Overall fit of cryoEM density map to the structure models. A) Overall density maps of apo IDE in closed conformation with built structure model. B) Overall density maps of apo IDE in open conformation with built structure model. C) Overall density maps of apo IDE in open/closed conformation with built structure models. D) Overall density maps of insulin bound IDE with built structure model. E) Representative density with built models of two α-helixes from apo IDE in O/pO conformation (residue 659-672 and residue 855-875). F) Representative density with built models of two α-helixes from insulin bound IDE (residue 660-673, and residue 677-691).

Figure 3-Figure supplement 1 Comparison of four distinct conformers of IDE, Open (O), partially open (O), partially closed (pC), and closed (C). (A) The comparison of pC (cyan) with pO (magenta), (B) pC (cyan) with C (magenta), (C) pC (cyan) with O (magenta), (D) pO (purple) with O (magenta), and (E) pC (cyan), pO (magenta), and O (green). IDE is aligned by their IDE-C domain.

Figure 4-Figure supplement 1 SAXS analysis of IDE. IDE SAXS scattering profile (top), P(r) function distribution (middle), and Guinier plot (bottom) of IDE without EDTA (A), IDE with EDTA (B), and IDE with EDTA and insulin (C). The solution scattering of models is calculated and fitted to experiment data by CRYSOL. The P(r) distribution, the real space R_g, and D_{max}, were calculated by GNOM. O/pO stands for cryoEM open/partial open state of IDE. C stands for IDE closed state from crystal structure, and pC/pC stands for cryoEM partial-closed/partial-closed state of IDE that is solved in the presence of insulin.

Figure 5-Figure supplement 1 Comparison of crystal structures of insulin- or Aβ-bound IDE. (A) Crystal structure of insulin- and Fab1-bound IDE (PDB code: 5WOB). Fab is not shown for clarity. (B) Insulin-bound IDE (PDB code: 2WBY). Alignment of the insulin (C) and IDE (D) from 5WOB and 2WBY. (E) Crystal structure of Aβ- and Fab1-bound IDE (PDB code: 4M1C). Fab is not shown for clarity. (F) Aβ-bound IDE (PDB code: 2G47). Alignment of Aβ (G)

and IDE (H) from 4M1C and 2G47. IDE-C is colored in grey; IDE-N in Fab1- and substrate-bound IDE is colored in cyan; IDE-N in substrate-bound IDE is colored in green. Insulin A and B chains are colored in magenta and cyan, respectively. Aβ is colored in blue. The RMSD is calculated by PYMOL.

Figure 5-Figure supplement 2 Comparison of thermal B factor distribution of four cryoEM IDE structures, and two crystal structures. Thermal B factor distribution of cryoEM structures of $Fab_{H11\text{-}E}$- and insulin-bound IDE pC/pC (A), or apo IDE pO/pO (B), pO/O (C), and O/O (D) and that of crystal structures of Fab1-bound IDE in the absence (E) and presence of insulin (F). Averaged B factors of IDE door subdomain and D3 domain are shown for comparison in A-D. Only one dimer is shown in insulin- and Fab1-bound IDE structure as four IDE dimers in the asymmetric unit and are similar. Summary of average thermal B factors of various IDE domains for cryoEM structures (G) and crystal structures (H).

Figure 5-Figure supplement 3 Amide hydrogen-deuterium exchange profiles of IDE alone (A) and IDE in the presence of BDM44768 (B). The percentages of deuteration levels of each peptide fragment at various time points are shown as a heat map color-coded from blue (<10%) to red (>90%), as indicated at the bottom right of the figure. Each block represents a peptide segment analyzed at each of the six time points (from top to bottom: 10, 100, 1,000, 10,000, 100,000, and 1000,000 seconds). Proline residues, and regions with no amide exchange data available are colored in gray. The structure features of IDE are shown above IDE sequences and colored according to their domains/subdomains.

Figure 5-Figure supplement 4 Amide hydrogen-deuterium exchange profiles of IDE alone (A) and IDE in the presence of 6bk (B). The percentages of deuteration levels of each peptide fragment at various time points are shown as a heat map color-coded from blue (<10%) to red (>90%), as indicated at the bottom right of the figure. Each block represents a peptide segment analyzed at each of the six time points (from top to bottom: 10, 100, 1,000, 10,000, 100,000, and 1000,000 seconds). Proline residues, and regions with no amide exchange data available are colored in gray. The structure features of IDE are shown above IDE sequences and colored according to their domains/subdomains.

Figure 5-Figure supplement 5 HDX-MS analysis of IDE-small molecule inhibitor interaction. Differences in deuteration levels in the free and BDM44768-bound (A) or 6bK-bound IDE (B) at various time points (from top to bottom: 10, 100, 1,000, 10,000, 100,000, and 1000,000 seconds) are shown in a color-coded bar ranging from blue (-50%) to red (50%), as indicated at the bottom right of the figure. The structure features of IDE are shown above IDE sequences and colored according to their domains/subdomains.

Figure 5-Figure supplement 6 Progression curves that have the significant difference in HDX of IDE when 6bK or BDM-44768 (BDM) were present. The standard deviation error bar to the WT IDE data is determined by three individual experiments.

Figure 6-Figure supplement 1 Amide hydrogen-deuterium exchange profiles of IDE alone (A) and IDE in the presence of insulin (B). The percentages of deuteration levels of each peptide fragment at various time points are shown as a heat map color-coded from blue (<10%) to red (>90%), as indicated at the bottom right of the figure. Each block represents a peptide segment analyzed at each of the six time points (from top to bottom: 10, 100, 1,000, 10,000, 100,000, and 1000,000 seconds). Proline residues, and regions with no amide exchange data available are colored in gray. The structure features of IDE are shown above IDE sequences and colored according to their domains/subdomains.

Figure 6-Figure supplement 2 Amide hydrogen-deuterium exchange profiles of IDE alone (A) and IDE in the presence of Aβ (B). The percentages of deuteration levels of each peptide fragment at various time points are shown as a heat map color-coded from blue (<10%) to red (>90%), as indicated at the bottom right of the figure. Each block represents a peptide segment analyzed at each of the six time points (from top to bottom: 10, 100, 1,000, 10,000, 100,000, and 1000,000 seconds). Proline residues, and regions with no amide exchange data available are colored in gray. The structure features of IDE are shown above IDE sequences and colored according to their domains/subdomains.

Figure 6-Figure supplement 3 HDX-MS analysis of IDE-substrate interaction. Differences in deuteration levels in the free and insulin-bound (A) or Aβ-bound IDE (B) at various time points (from top to bottom: 10, 100, 1,000, 10,000, 100,000, and 1000,000 seconds) are

shown in a color-coded bar ranging from blue (-50%) to red (50%), as indicated at the bottom right of the figure. The structure features of IDE are shown above IDE sequences and colored according to their domains/subdomains.

Figure 6-Figure supplement 4 Progression curves that have the significant difference in HDX of IDE when insulin (INS) or Aβ were present. The standard deviation error bar to the WT IDE data is determined by three individual experiments.

Figure 7-Figure supplement 1 Insulin binding at IDE catalytic chamber from Fab1- and insulin-bound IDE crystal structure at 3.95 Å resolution. All eight catalytic chambers from four IDE dimers in an asymmetric unit are shown. Insulin is colored in pink stick and the electron density around insulin is colored in yellow. The secondary structures and residues crucial for insulin binding of IDE is shown in grey.

Figure 7-Figure supplement 2 The fit of the unfolded insulin A or B chain with electron density inside the catalytic chamber of IDE from cryoEM structure of insulin-bound IDE. (A, B) Two likely fit of either insulin A or B chain into the extra-density at the catalytic chamber of both IDE subunits. Only electron density within 3Å around insulin are shown. The detailed features in the possible fit of extra electron density with unfolded insulin A (A) or B chain (B). The atoms were colored as N, blue; O, red; S, black; and C, magenta (insulin chain A), and C, cyan (insulin chain B). (C, D) The electron density of insulin and the surrounding residues of IDE. H110 and H112 are residues binding the catalytic Zn^{2+} ion while F115 and F820 form a hydrophobic pocket for the substrate binding. Electron density map is contoured to the level that the density around H110 and H112 (C) or insulin (D) is clearly visible to show the strength of the ligand density.

Supplementary file legends

Supplementary file 1. Data collection and structure refinement statistics

Supplementary file 2. CryoEM data collection and processing statistic

Supplementary file 3. CryoEM map and model refinement statistics

Supplementary file 4. Distances and angles between center of mass of different domains of IDE cryoEM and crystal structures.

Figure 1

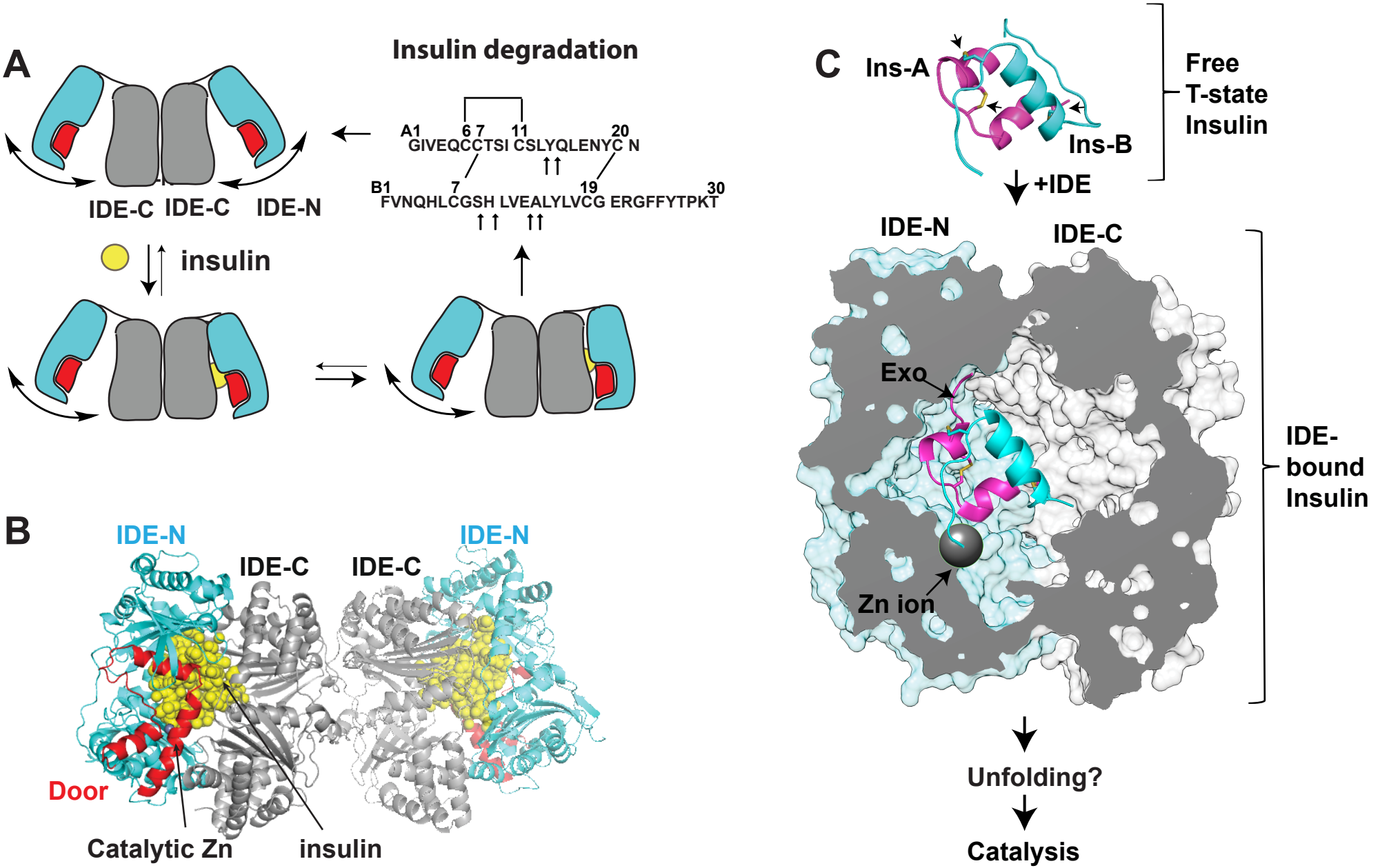
A
Insulin degradation
A1 6 7 11 20
GIVEQCCTSI CSLYQLENYC N
B1 7 19 30
FVNQHLCGSH LVEALYLVCG ERGFFYTPKT
IDE-C IDE-C IDE-N
insulin
B
IDE-N
IDE-C
IDE-C
IDE-N
Door
Catalytic Zn
insulin
C
Ins-A
Ins-B
Free
T-state
Insulin
+IDE
IDE-N
IDE-C
Exo
Zn ion
IDE-
bound
Insulin
Unfolding?
Catalysis

Figure 2

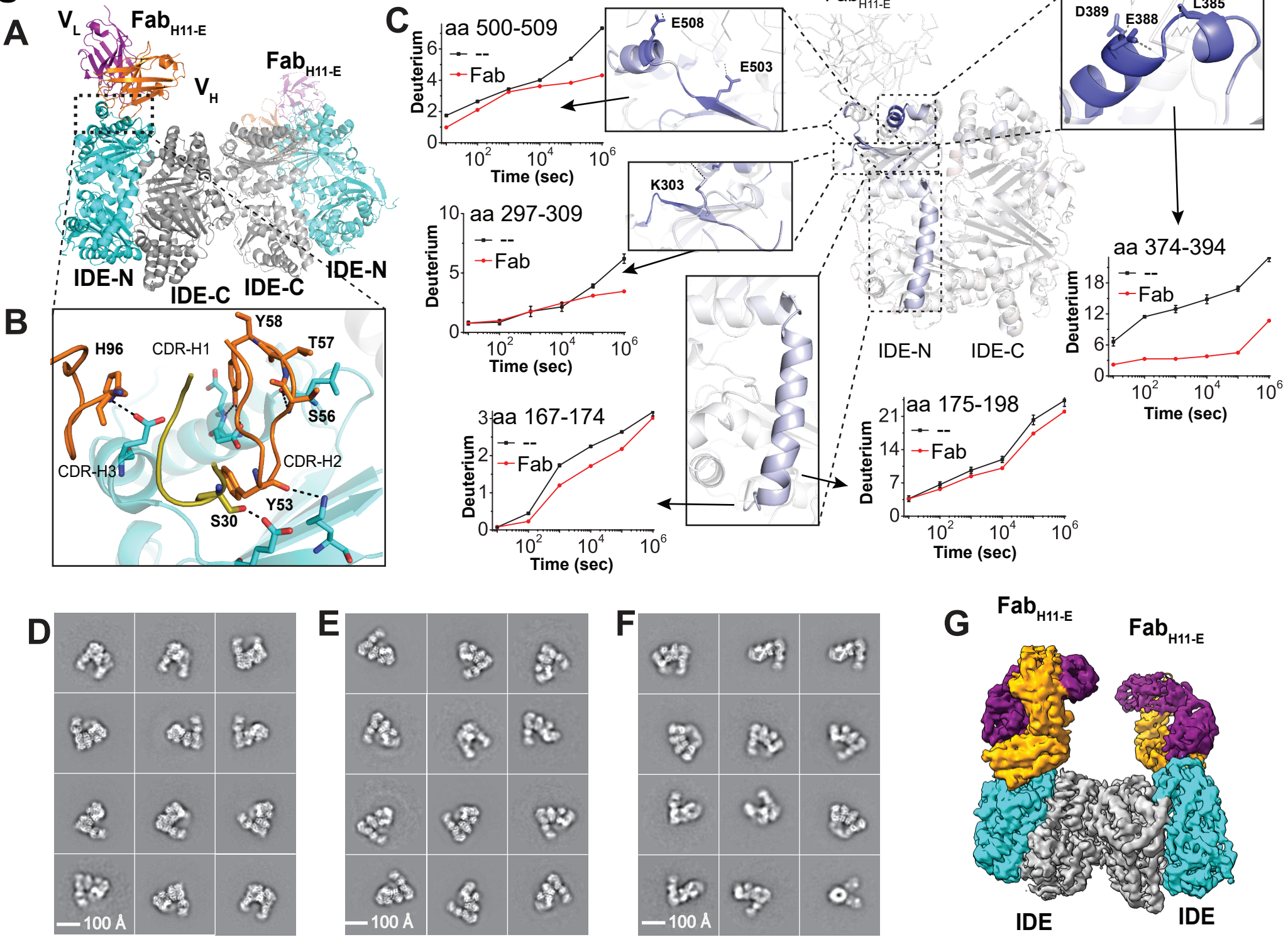
A
V_L
Fab_H11-E
V_H
Fab_H11-E
IDE-N
IDE-C
IDE-C
IDE-N
B
H96
CDR-H1
Y58
T57
S56
CDR-H2
CDR-H3
Y53
S30
C
aa 500-509
Deuterium
Time (sec)
Fab
E508
E503
K303
aa 297-309
aa 167-174
Fab_H11-E
D389
E388
L385
aa 374-394
IDE-N
IDE-C
aa 175-198
D
E
F
100 Å
100 Å
100 Å
G
Fab_H11-E
Fab_H11-E
IDE
IDE

Figure 3

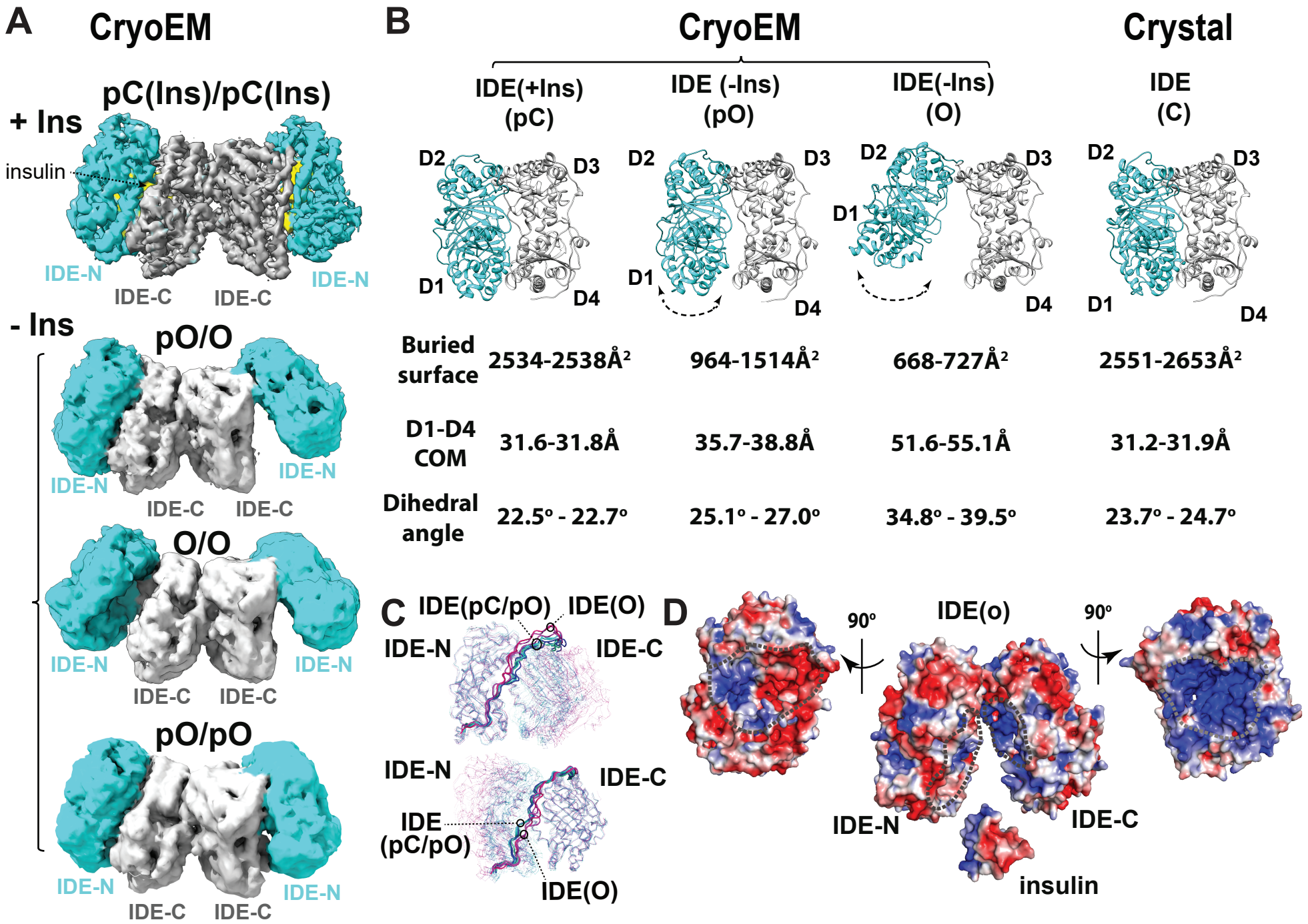
A
CryoEM
pC(Ins)/pC(Ins)
+ Ins
insulin
IDE-N
IDE-C
IDE-C
IDE-N
- Ins
pO/O
IDE-N
IDE-N
IDE-C
IDE-C
O/O
IDE-N
IDE-N
IDE-C
IDE-C
pO/pO
IDE-N
IDE-N
IDE-C
IDE-C
B
CryoEM
Crystal
IDE(+Ins) (pC)
IDE (-Ins) (pO)
IDE(-Ins) (O)
IDE (C)
D2
D3
D1
D4
Buried surface
2534-2538Å²
964-1514Å²
668-727Å²
2551-2653Å²
D1-D4 COM
31.6-31.8Å
35.7-38.8Å
51.6-55.1Å
31.2-31.9Å
Dihedral angle
22.5° - 22.7°
25.1° - 27.0°
34.8° - 39.5°
23.7° - 24.7°
C
IDE(pC/pO)
IDE(O)
IDE-N
IDE-C
IDE-N
IDE-C
IDE (pC/pO)
IDE(O)
D
90°
IDE(o)
90°
IDE-N
IDE-C
insulin

Figure 4

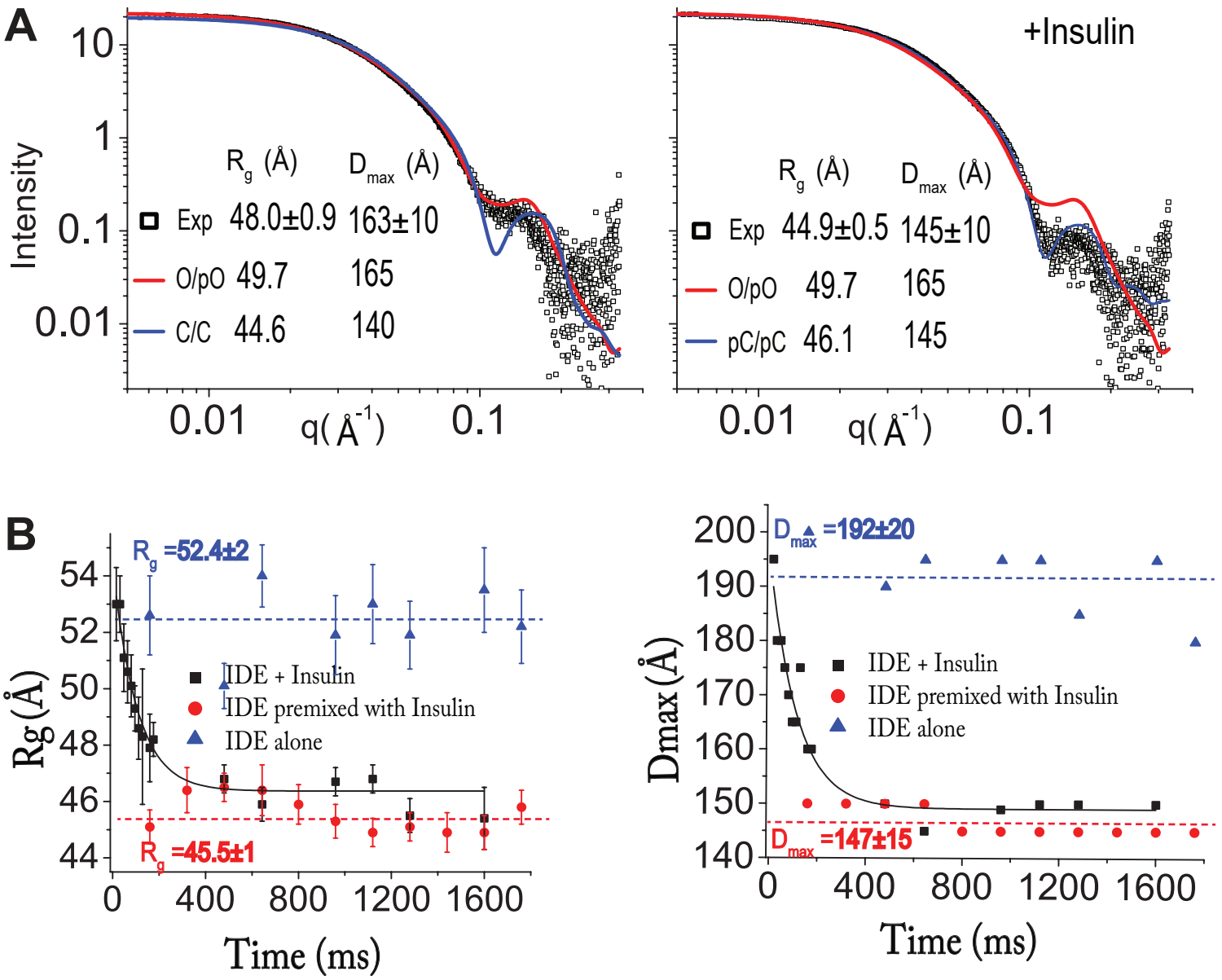
A
Intensity
10
1
0.1
0.01
0.01
q(Å^{-1})
0.1
R_g (Å)
D_{max} (Å)
Exp 48.0±0.9 163±10
O/pO 49.7 165
C/C 44.6 140
+Insulin
R_g (Å)
D_{max} (Å)
Exp 44.9±0.5 145±10
O/pO 49.7 165
pC/pC 46.1 145
B
R_g =52.4±2
R_g =45.5±1
IDE + Insulin
IDE premixed with Insulin
IDE alone
Rg(Å)
Time (ms)
D_{max} =192±20
D_{max} =147±15
Dmax (Å)

Figure 5

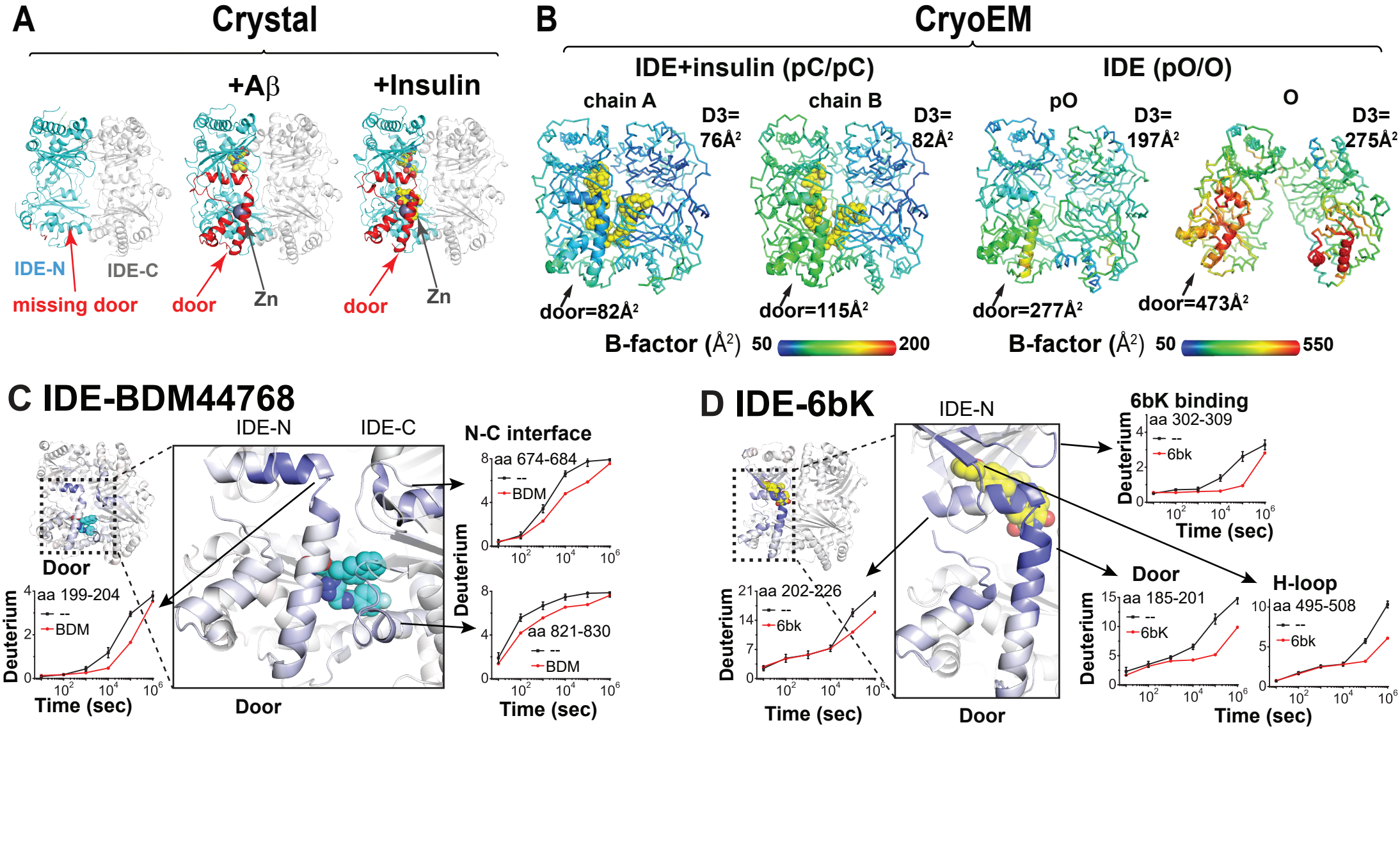
A
Crystal
+Aβ
+Insulin
IDE-N
IDE-C
missing door
door
Zn
door
Zn
B
CryoEM
IDE+insulin (pC/pC)
IDE (pO/O)
chain A
D3= 76Å²
chain B
D3= 82Å²
pO
D3= 197Å²
O
D3= 275Å²
door=82Å²
door=115Å²
door=277Å²
door=473Å²
B-factor (Å²) 50 200
B-factor (Å²) 50 550
C IDE-BDM44768
IDE-N
IDE-C
Door
aa 199-204
BDM
Deuterium
Time (sec)
Door
N-C interface
aa 674-684
BDM
aa 821-830
BDM
Deuterium
Time (sec)
D IDE-6bK
IDE-N
aa 202-226
6bk
Deuterium
Time (sec)
Door
6bK binding
aa 302-309
6bk
Deuterium
Time (sec)
Door
aa 185-201
6bK
Deuterium
Time (sec)
H-loop
aa 495-508
6bk
Time (sec)

Figure 6

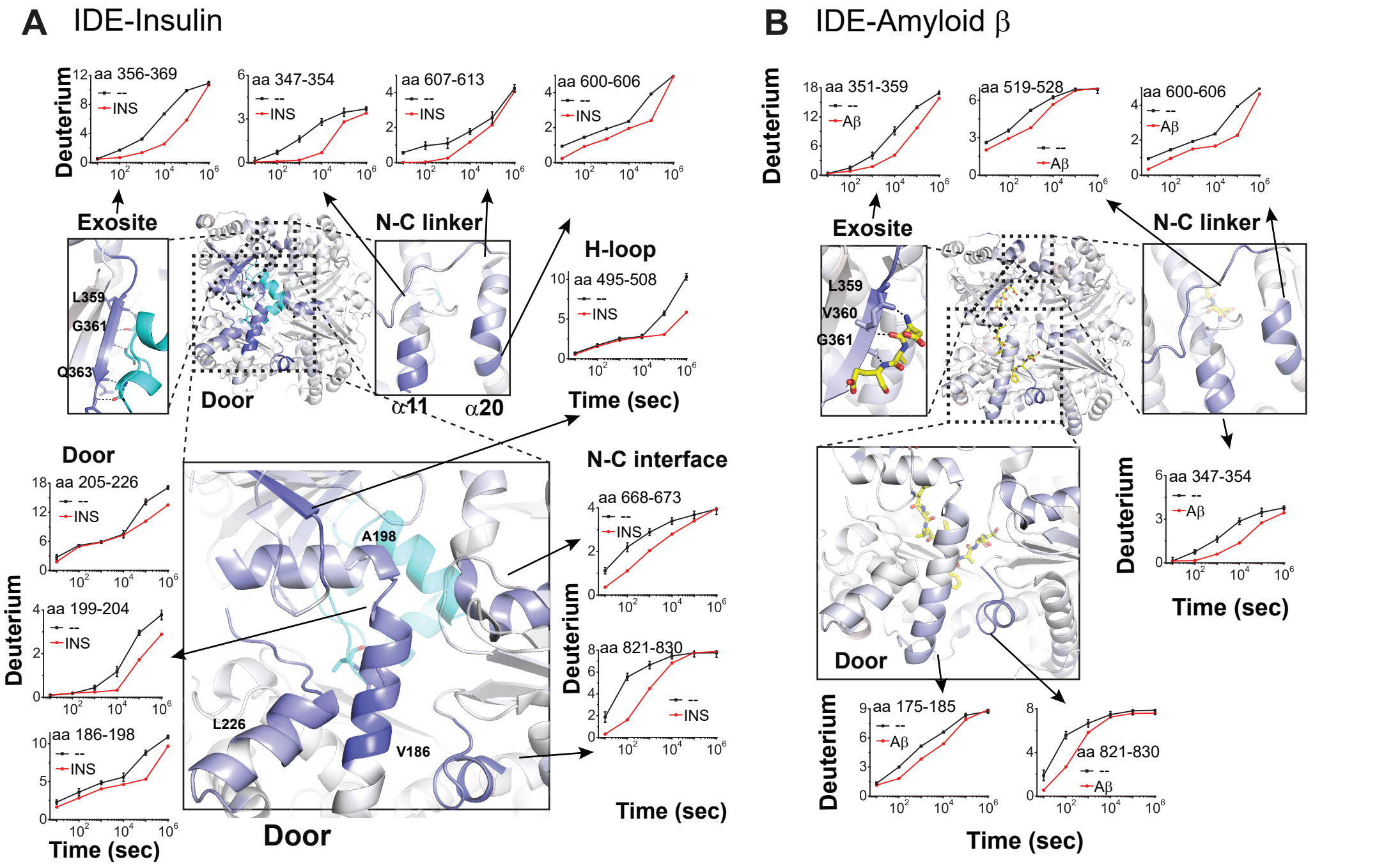
A IDE-Insulin
Deuterium
aa 356-369
aa 347-354
aa 607-613
aa 600-606
INS
Exosite
N-C linker
H-loop
aa 495-508
L359
G361
Q363
Door
α11
α20
Time (sec)
N-C interface
aa 205-226
aa 668-673
aa 199-204
aa 821-830
aa 186-198
A198
L226
V186
B IDE-Amyloid β
aa 351-359
aa 519-528
aa 600-606
Aβ
V360
aa 175-185
aa 821-830

Figure 7

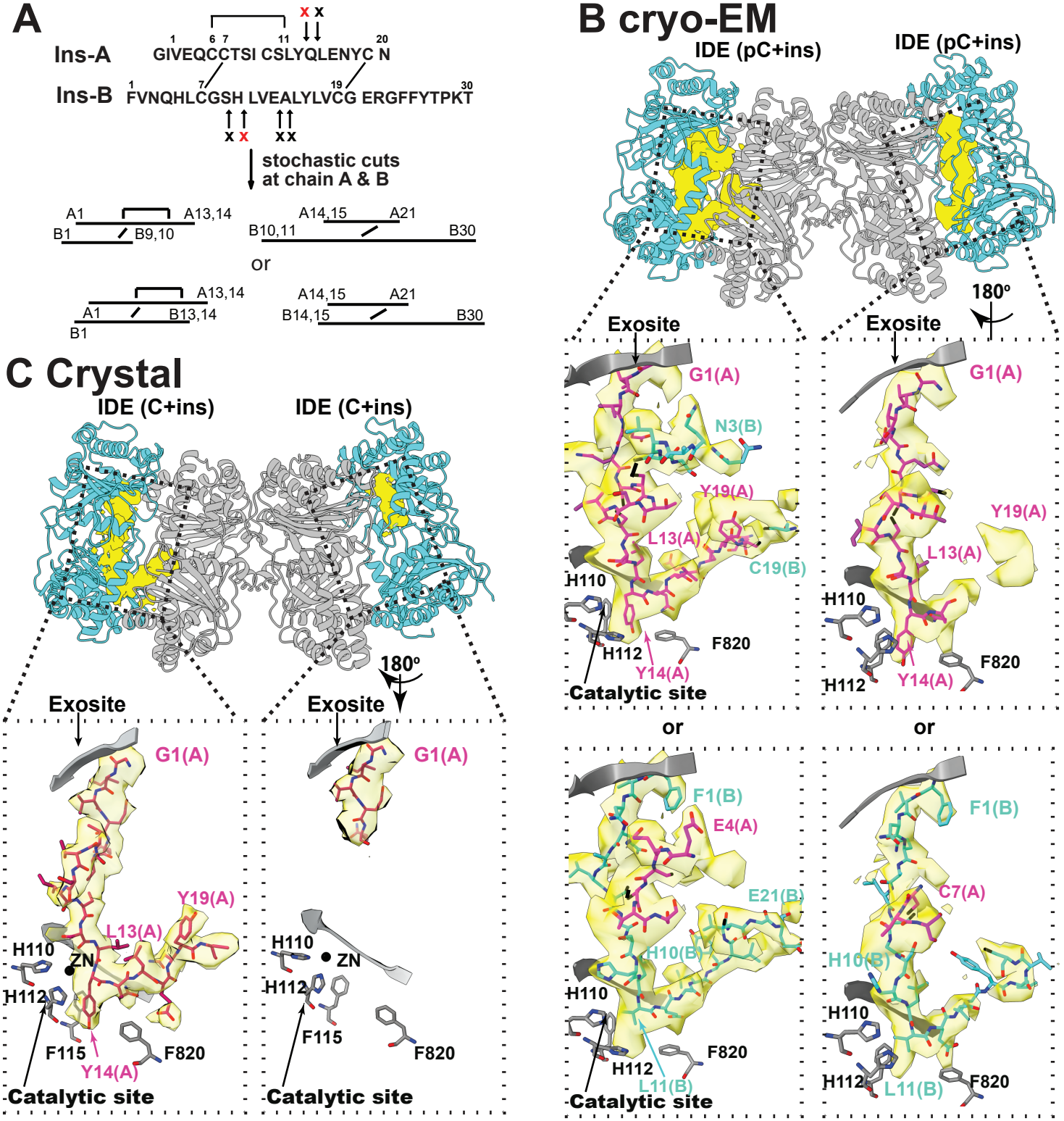
A
Ins-A
GIVEQCCTSI CSLYQLENYC N
Ins-B
FVNQHLCGSH LVEALYLVCG ERGFFYTPKT
stochastic cuts at chain A & B
A1 A13,14 B1 B9,10
A14,15 A21 B10,11 B30
or
A13,14 A1 B13,14 B1
A14,15 A21 B14,15 B30
B cryo-EM
IDE (pC+ins)
IDE (pC+ins)
180°
Exosite
Exosite
G1(A)
N3(B)
Y19(A)
L13(A)
C19(B)
H110
H112
F820
Y14(A)
Catalytic site
or
F1(B)
E4(A)
E21(B)
H10(B)
C7(A)
L11(B)
C Crystal
IDE (C+ins)
IDE (C+ins)
180°
Exosite
Exosite
G1(A)
Y19(A)
L13(A)
H110
ZN
H112
F115
F820
Y14(A)
Catalytic site

Figure 8

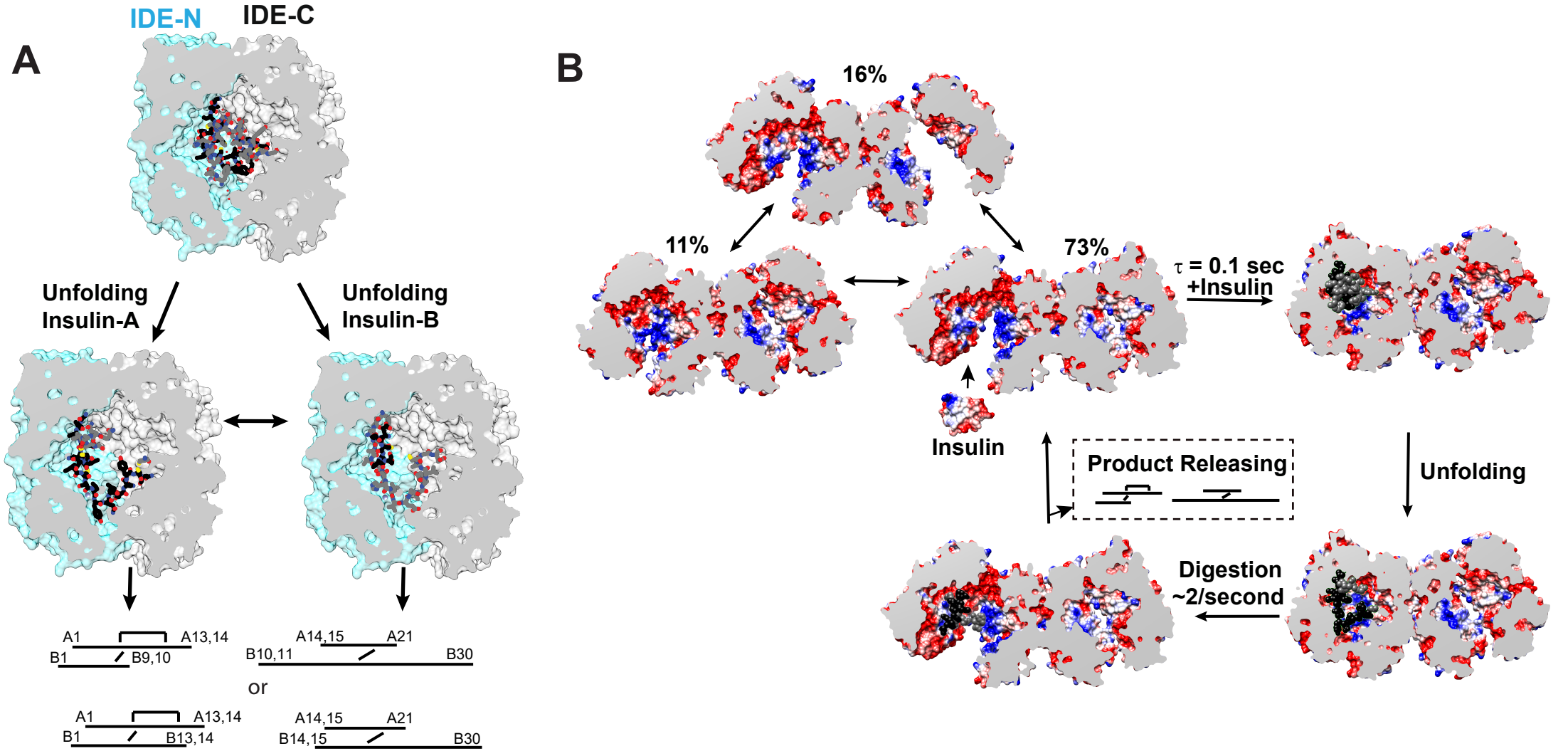
A
IDE-N
IDE-C
Unfolding
Insulin-A
Unfolding
Insulin-B
A1
A13,14
B1
B9,10
A14,15
A21
B10,11
B30
or
A1
A13,14
B1
B13,14
A14,15
A21
B14,15
B30
B
16%
11%
73%
Insulin
τ = 0.1 sec
+Insulin
Product Releasing
Unfolding
Digestion
~2/second

Figure 2-figure supplements 1

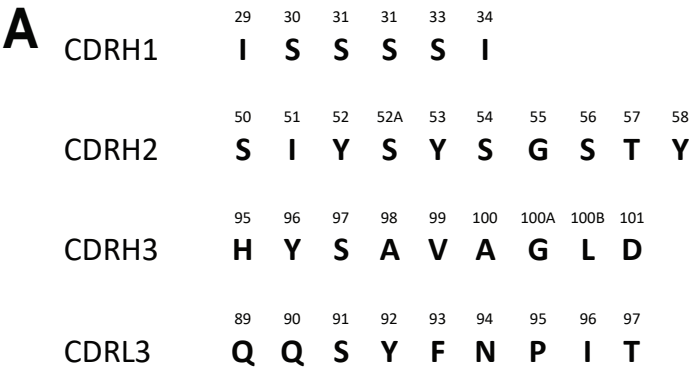

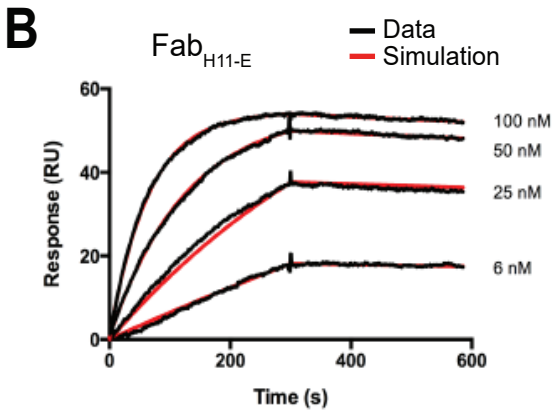

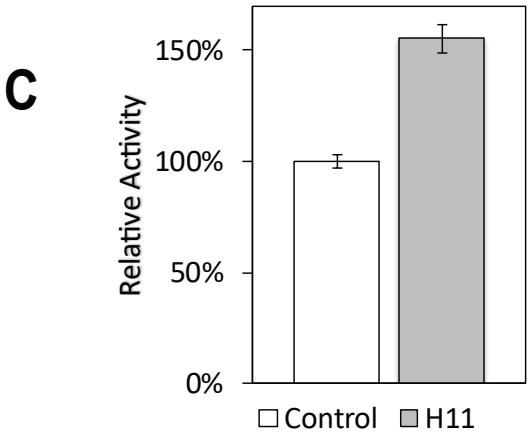

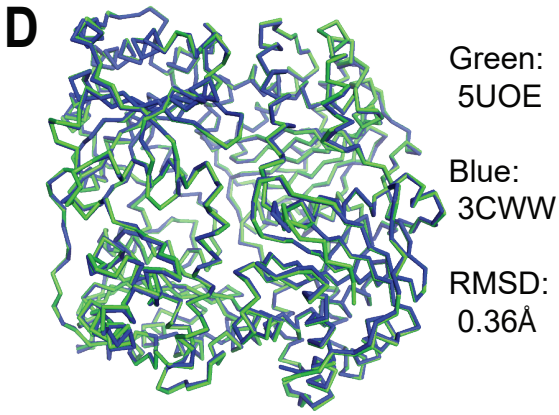

Figure 2-figure supplement 2

Pepsin digestion maps of IDE

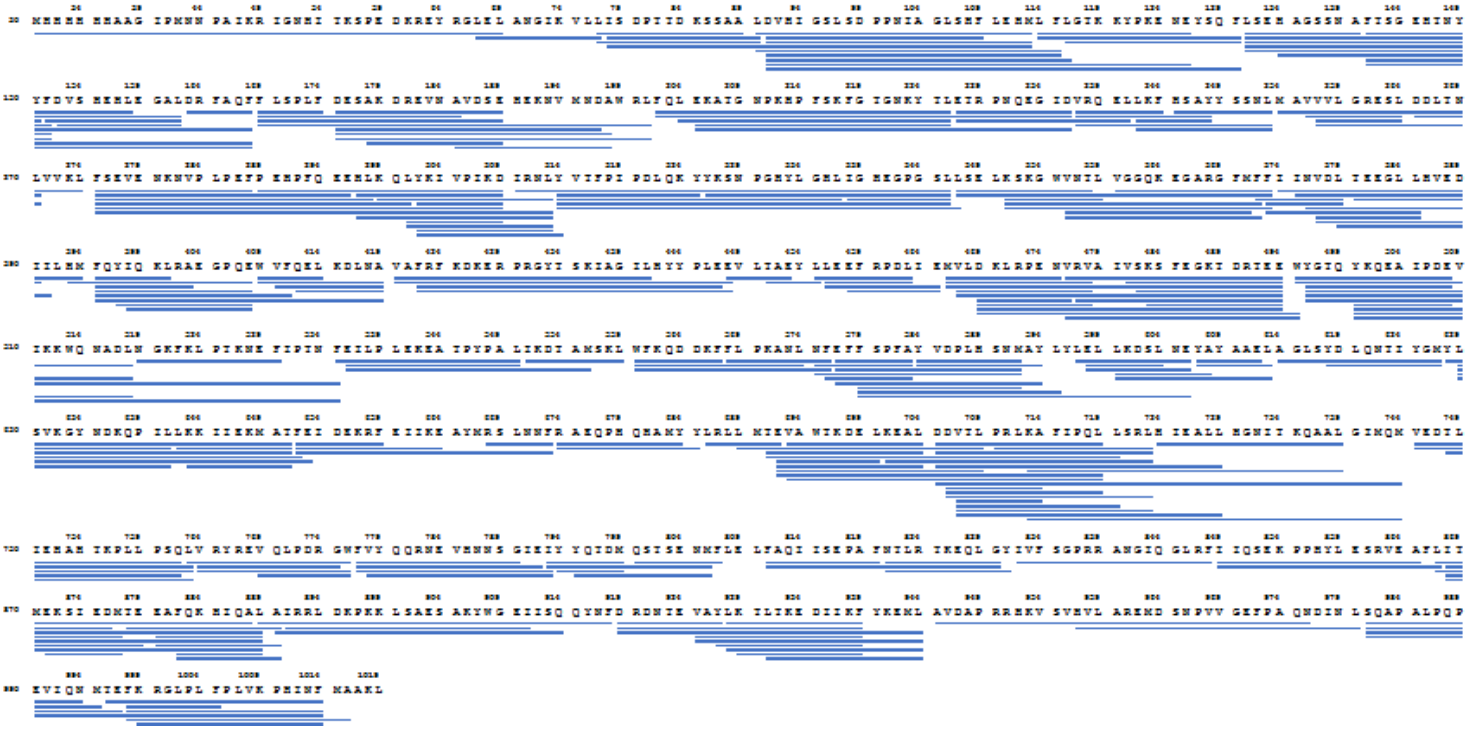

Figure 2-figure supplements 3

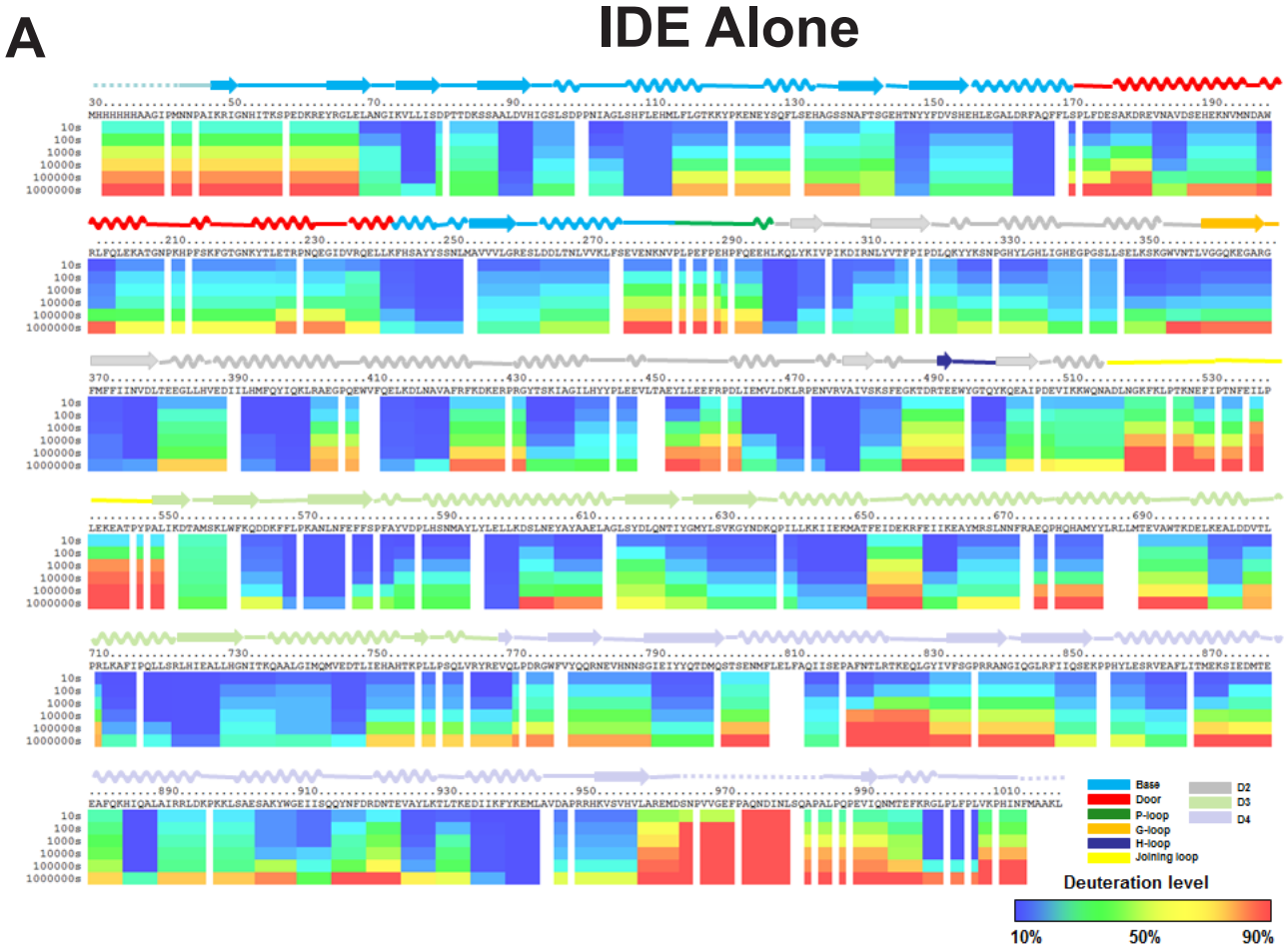

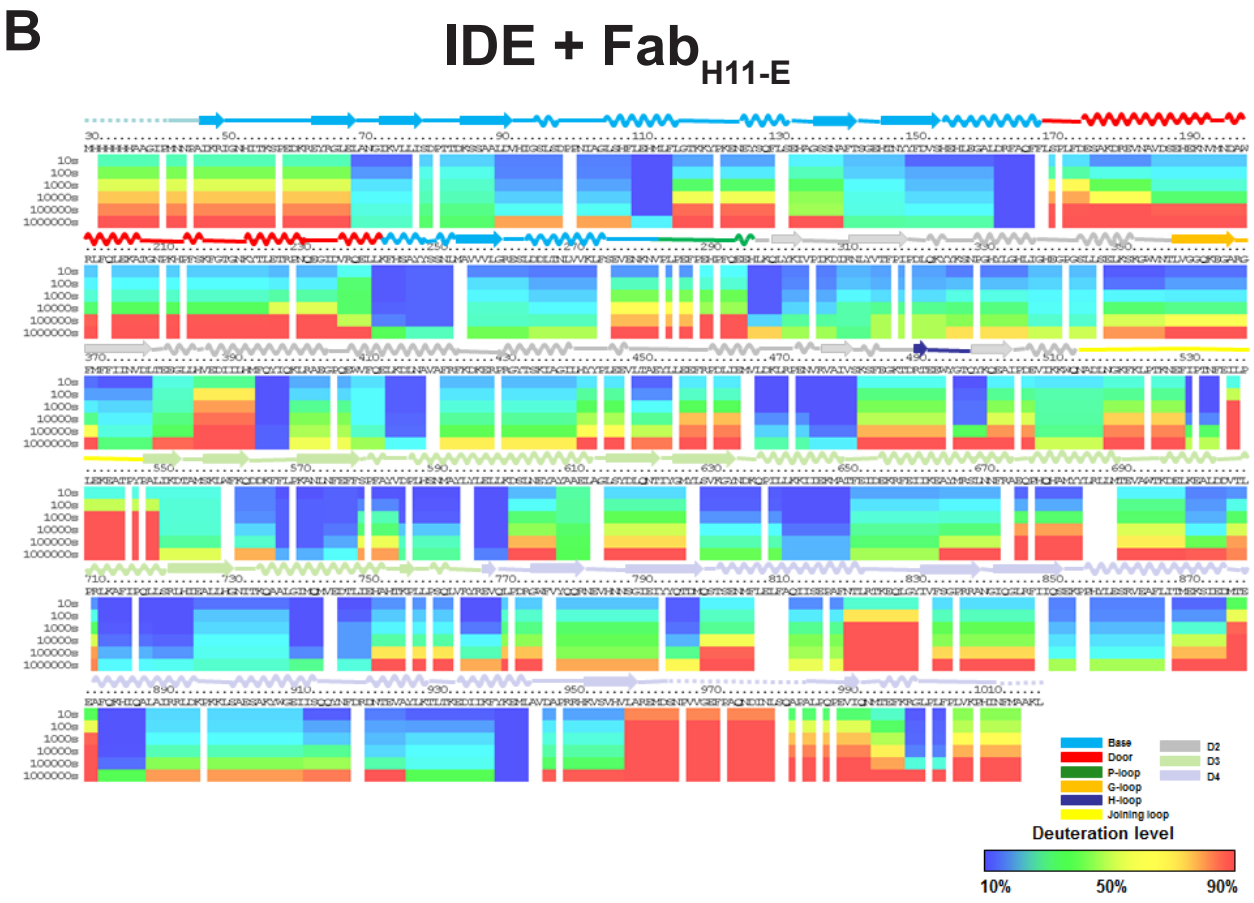

Figure 2-figure supplements 4

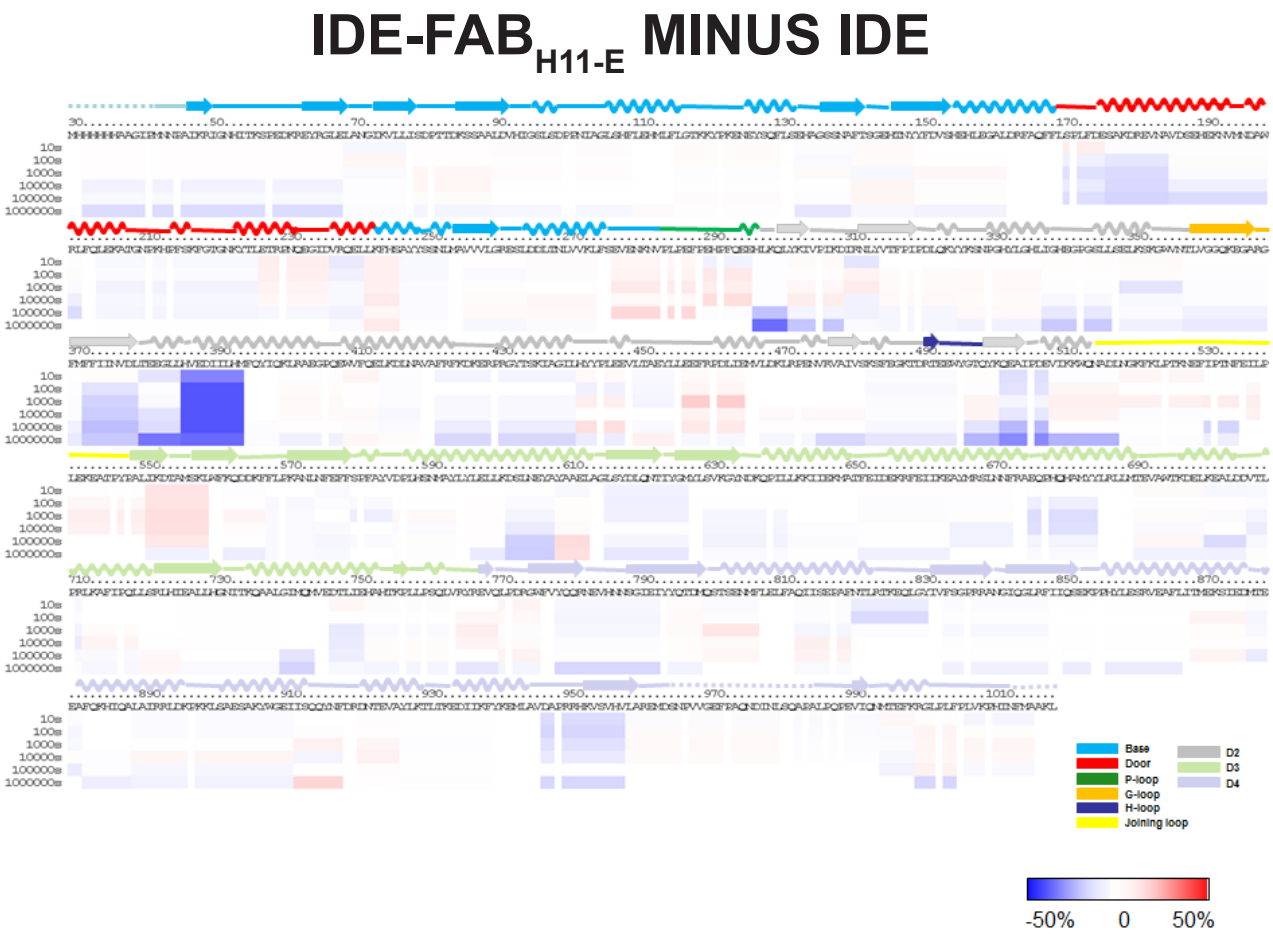

Figure 2-Figure Supplement 5

A

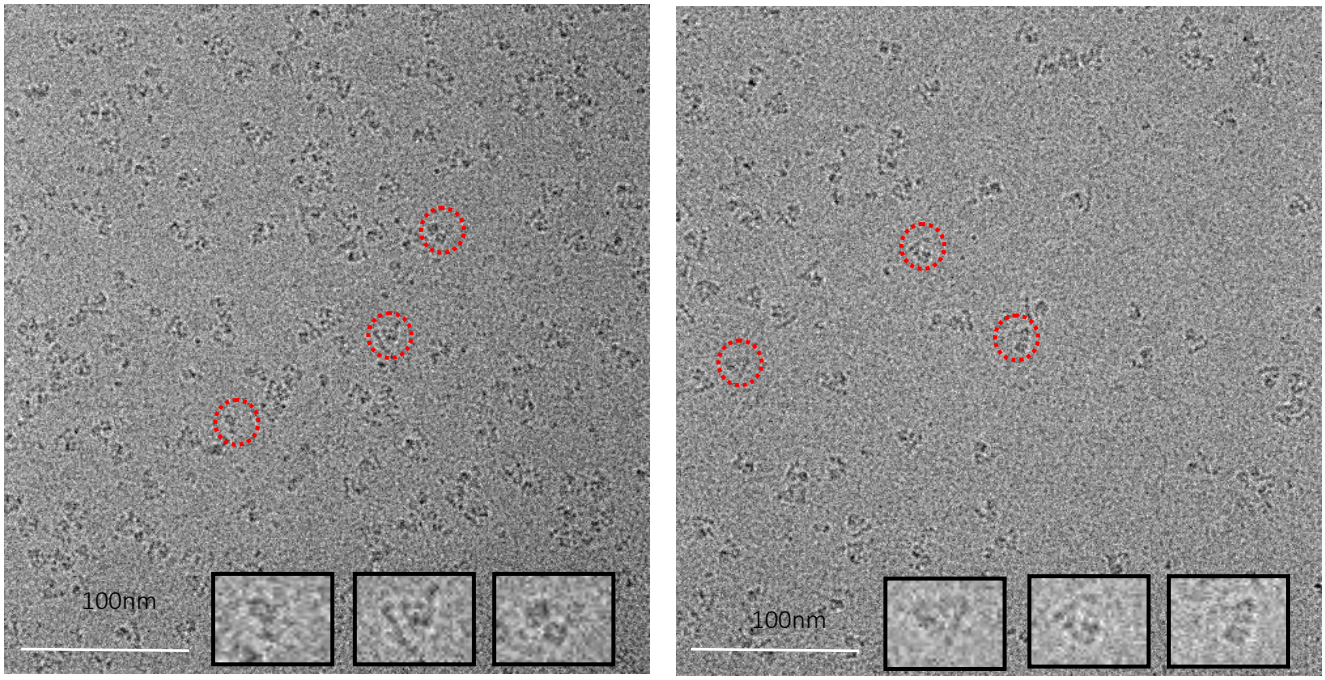

B

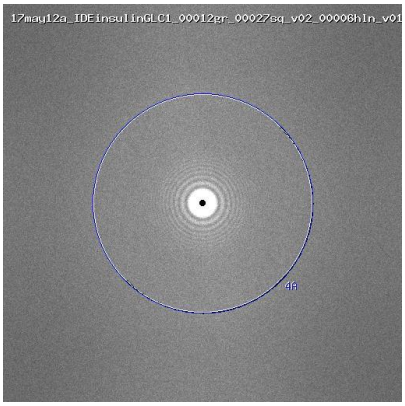

C

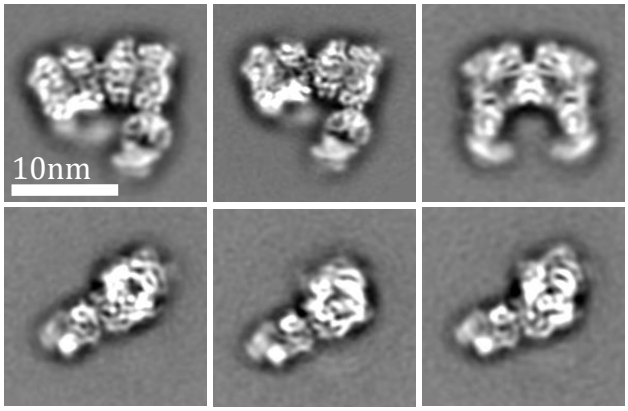

Figure 2-Figure Supplement 6

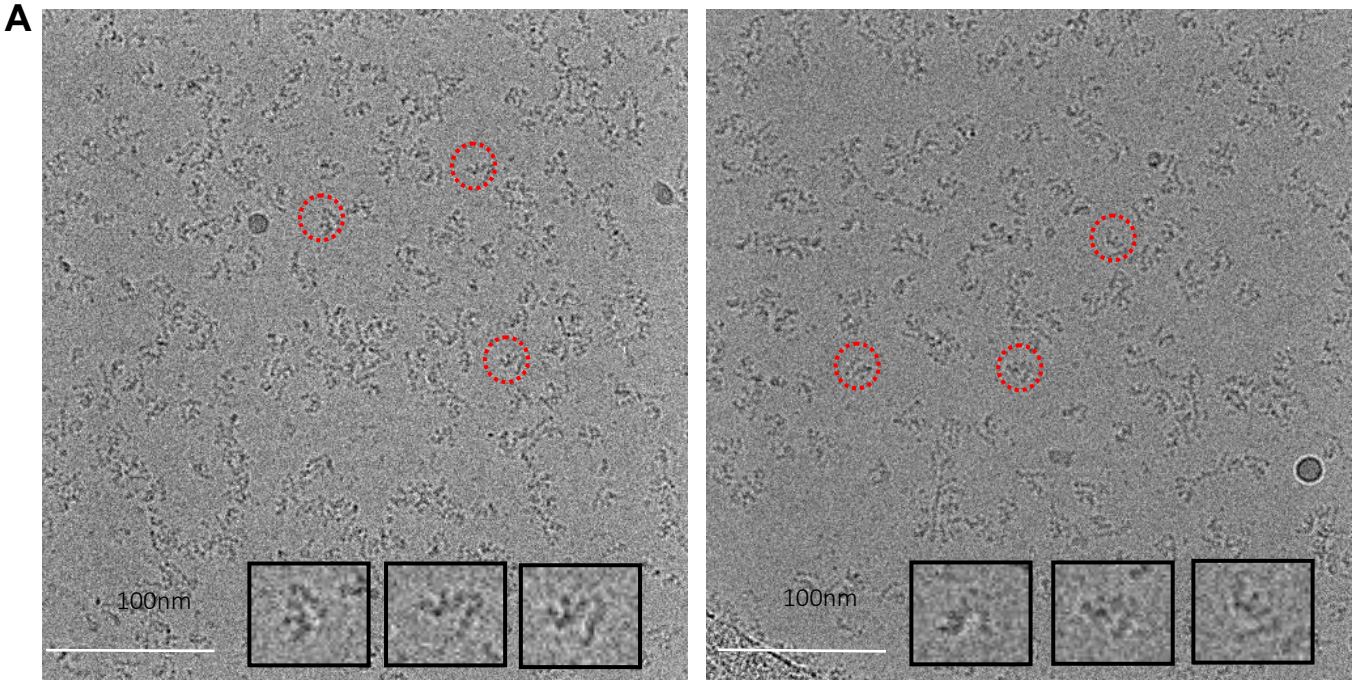

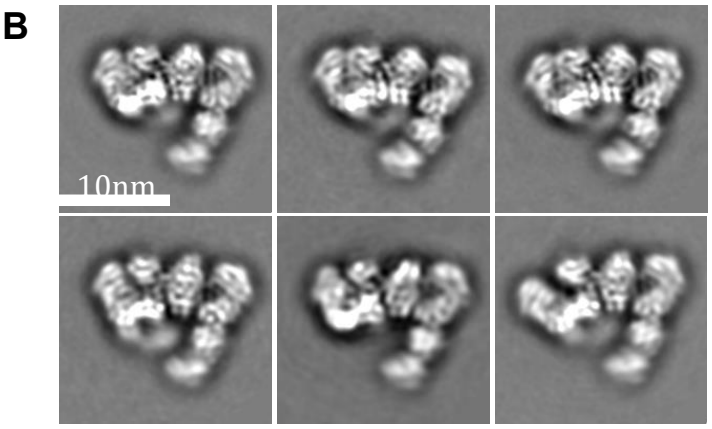

Figure 2-Figure Supplement 7

A

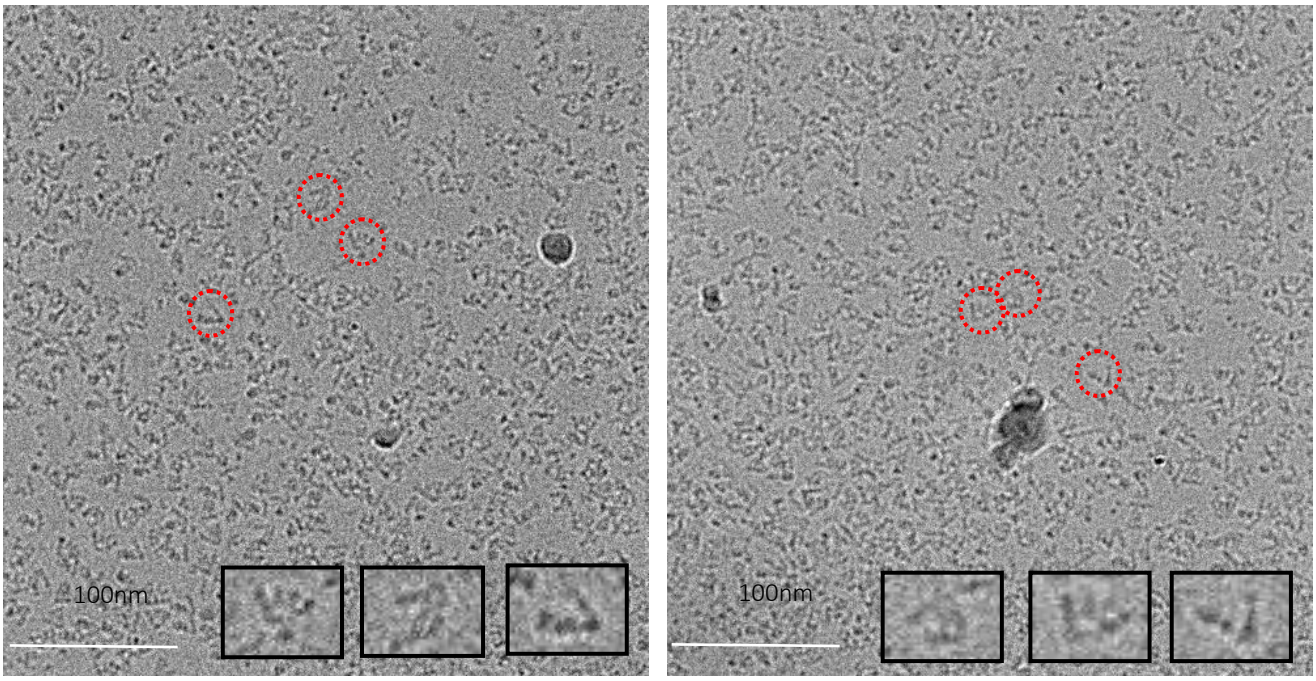

B

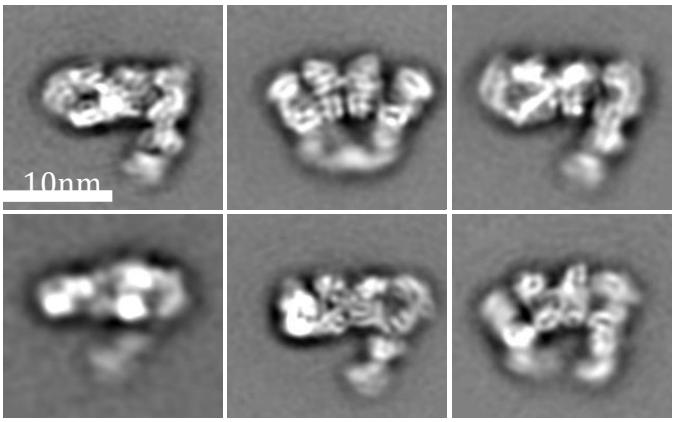

Figure 2 Figure Supplement 8

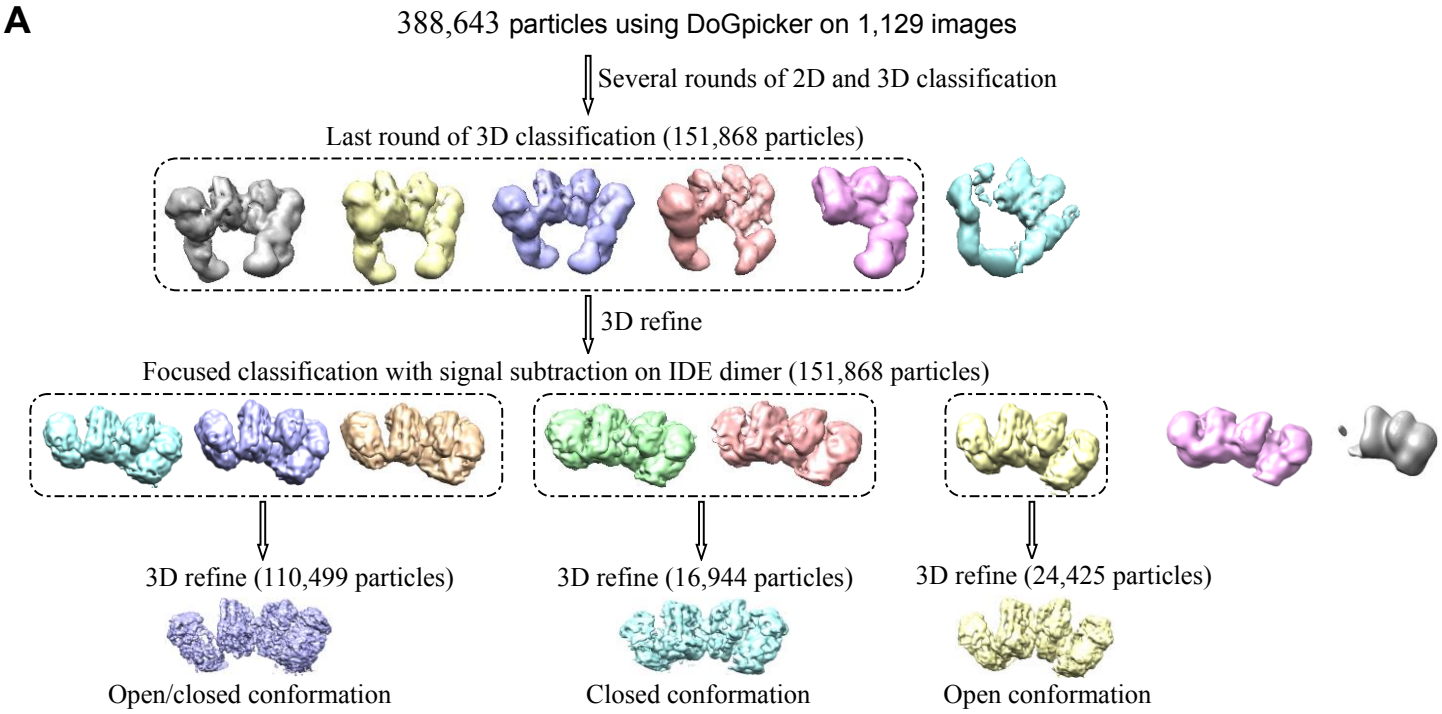

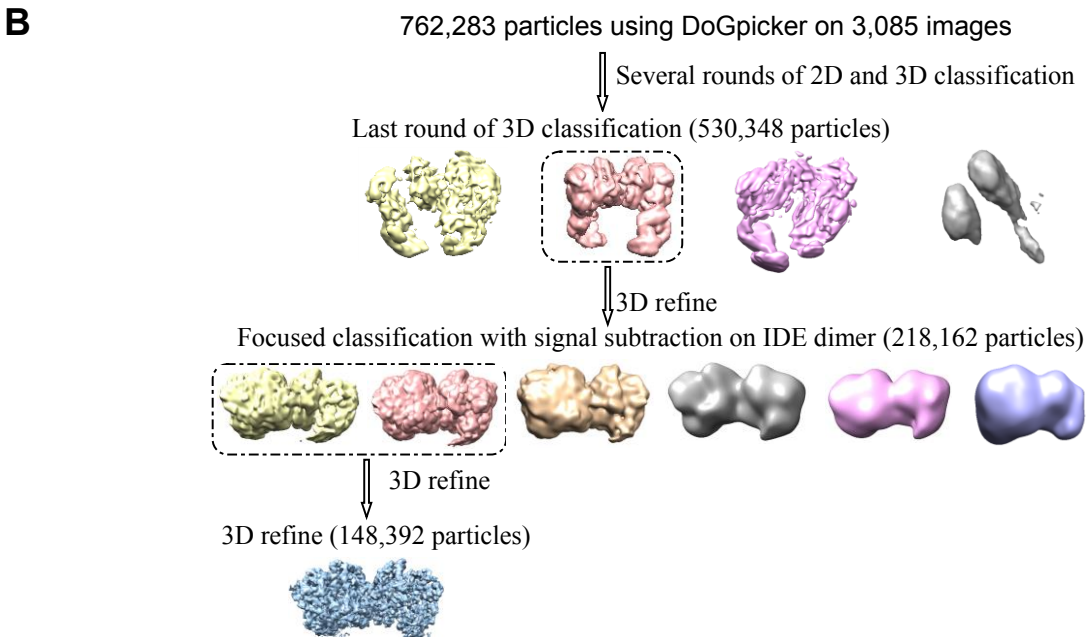

Figure 2 Figure Supplement 9

A

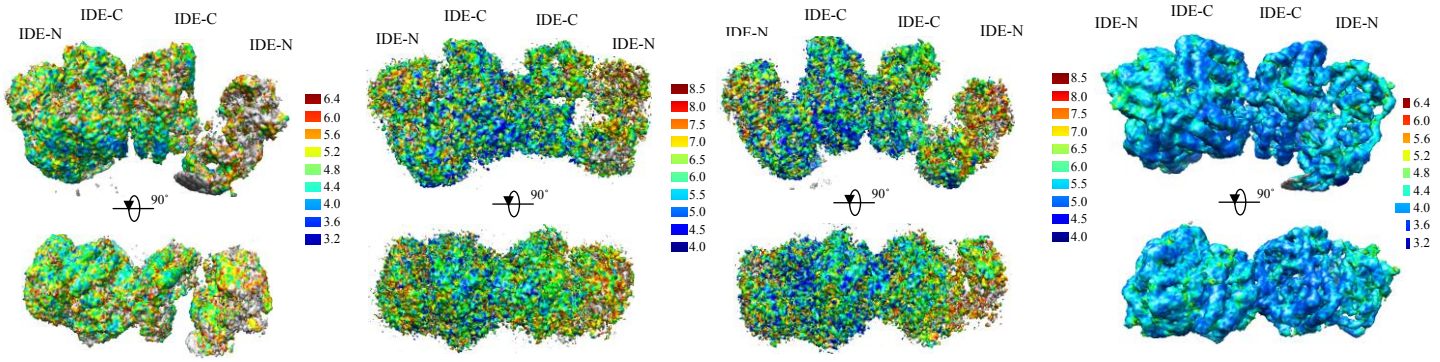

B

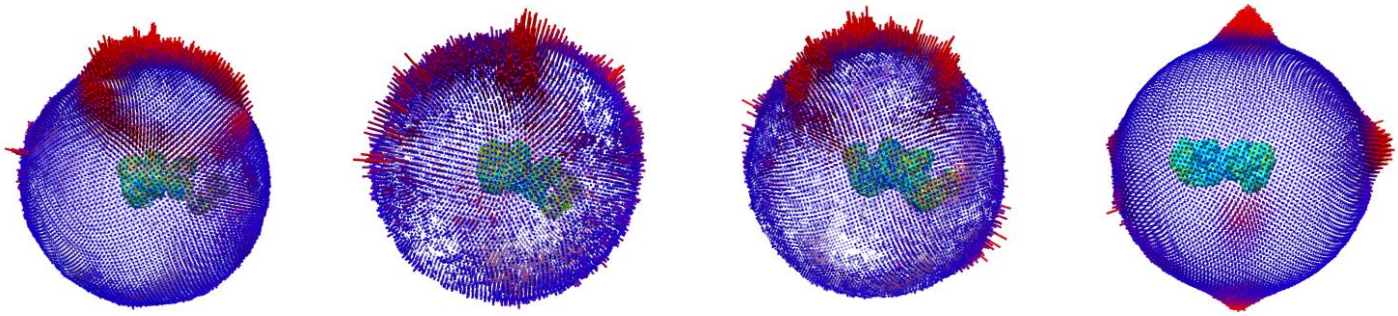

C

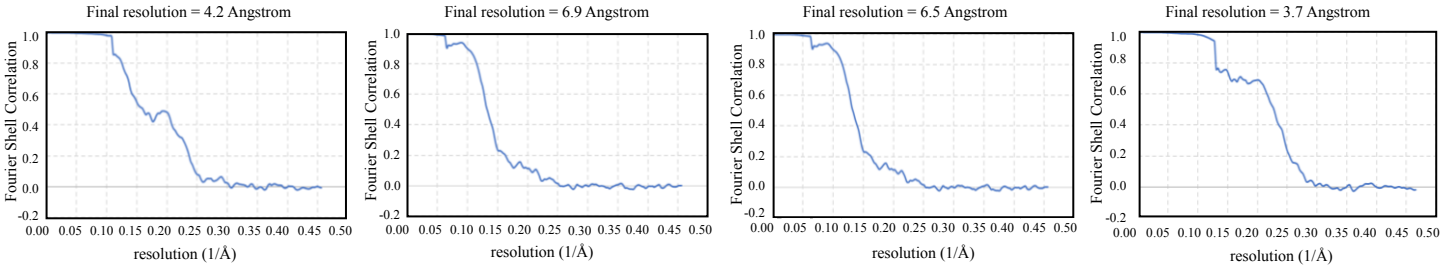

D

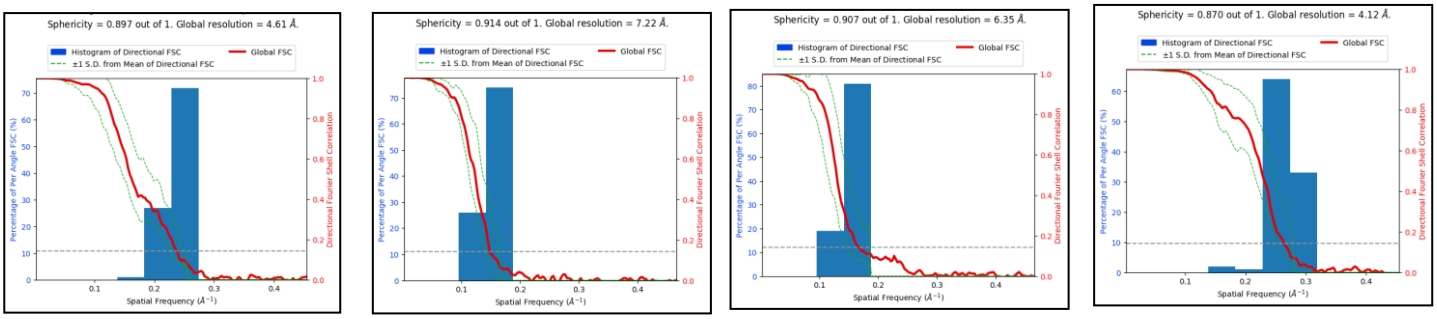

Figure 2 Figure Supplement 10

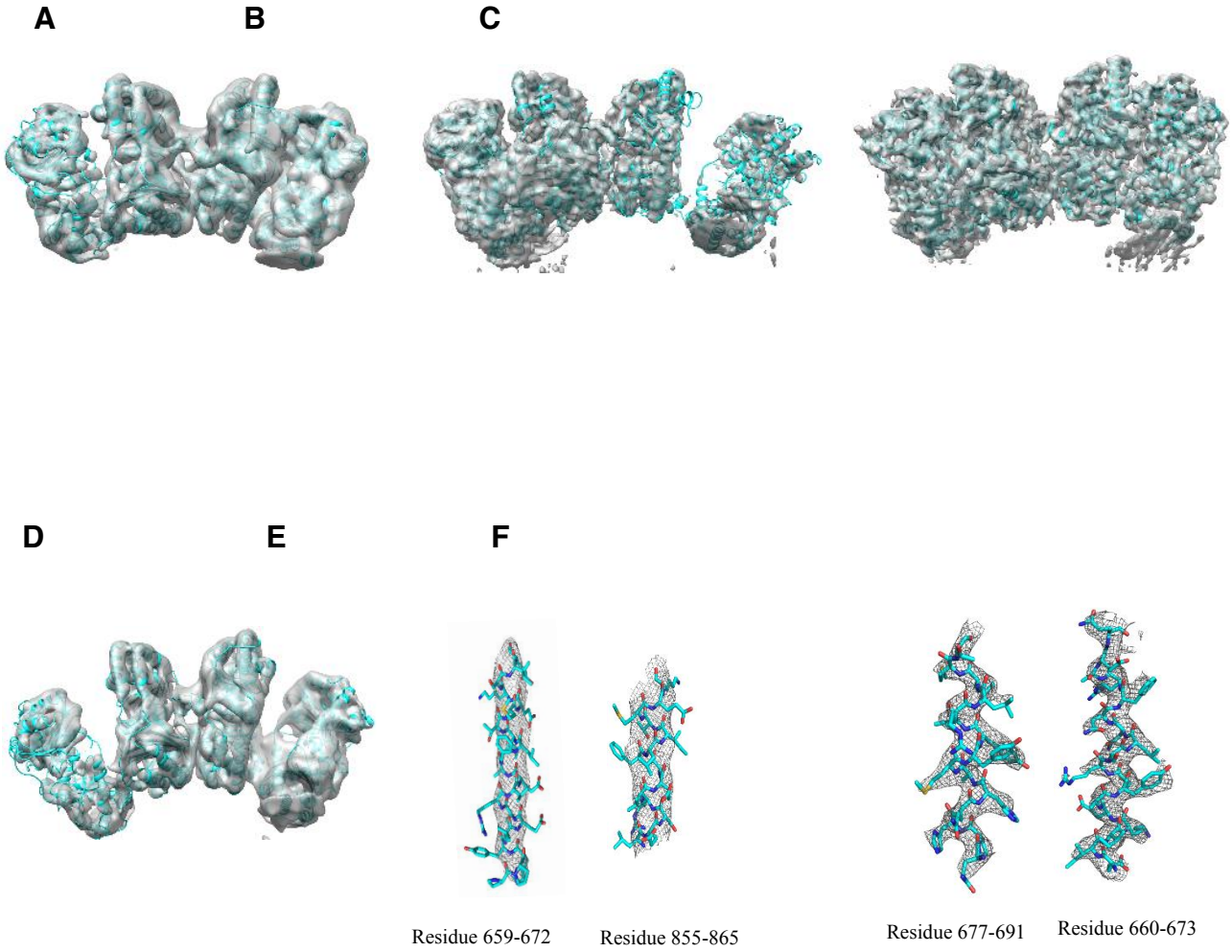

Figure 3 Figure Supplement 1

A pC(cyan)/pO(magenta)

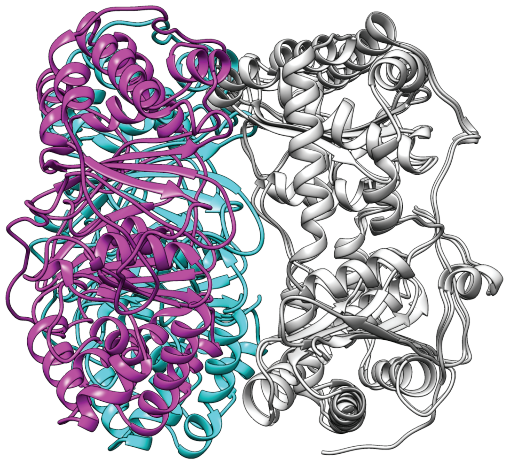

B pC(cyan)/C(magenta)

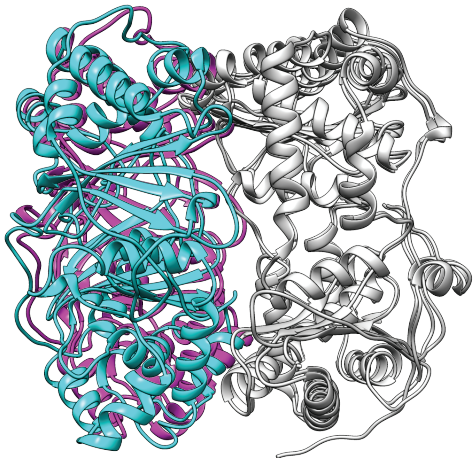

C pC(cyan)/O(magenta)

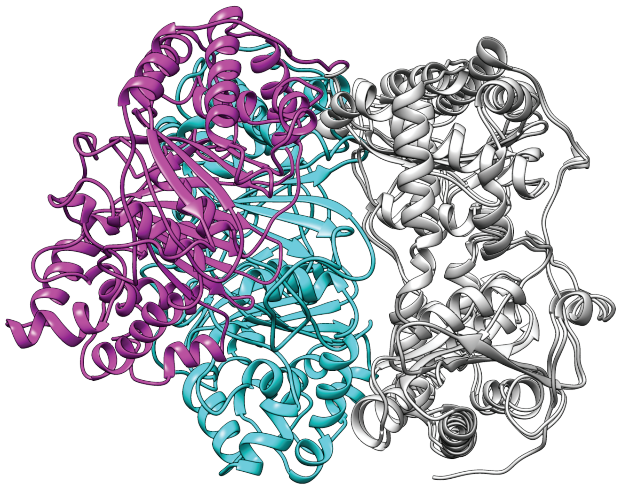

D pO(cyan)/O(magenta)

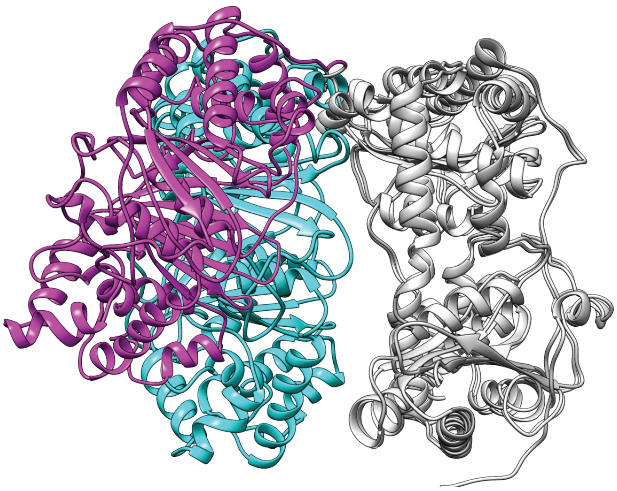

E pC(cyan)/pO(magenta)/O(green)

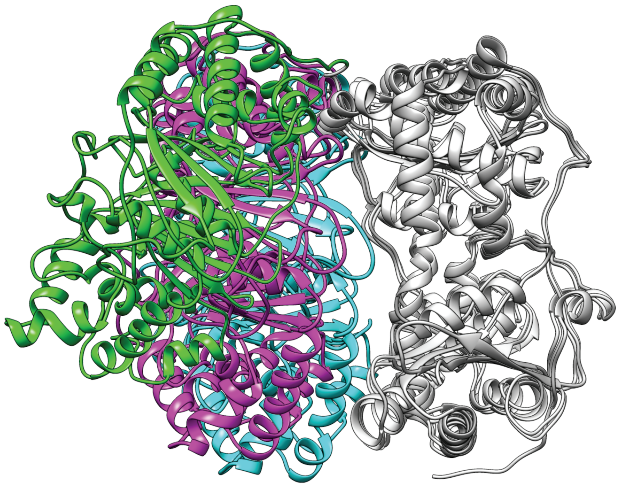

Figure 4 Figure Supplement 1

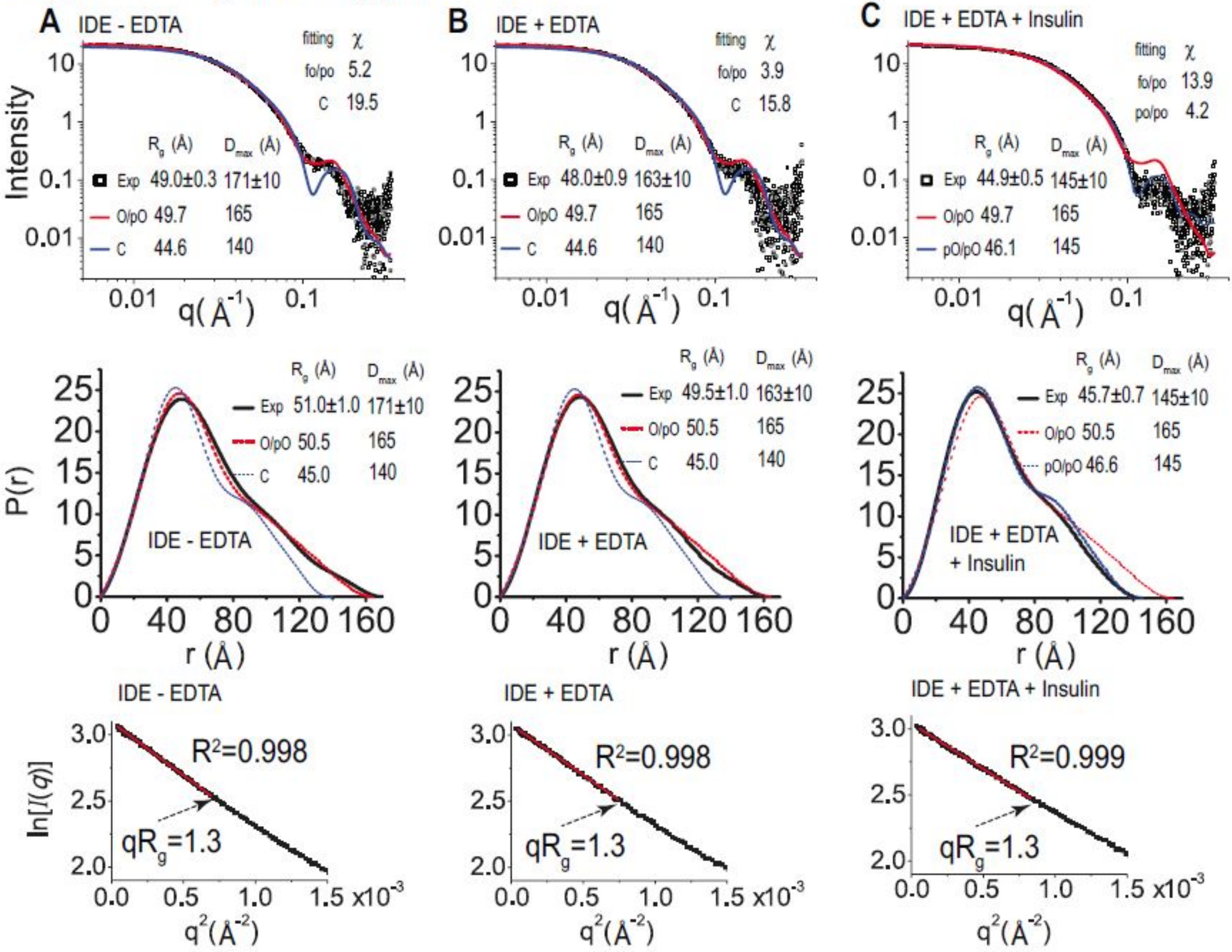

Figure 5 Figure Supplement 1

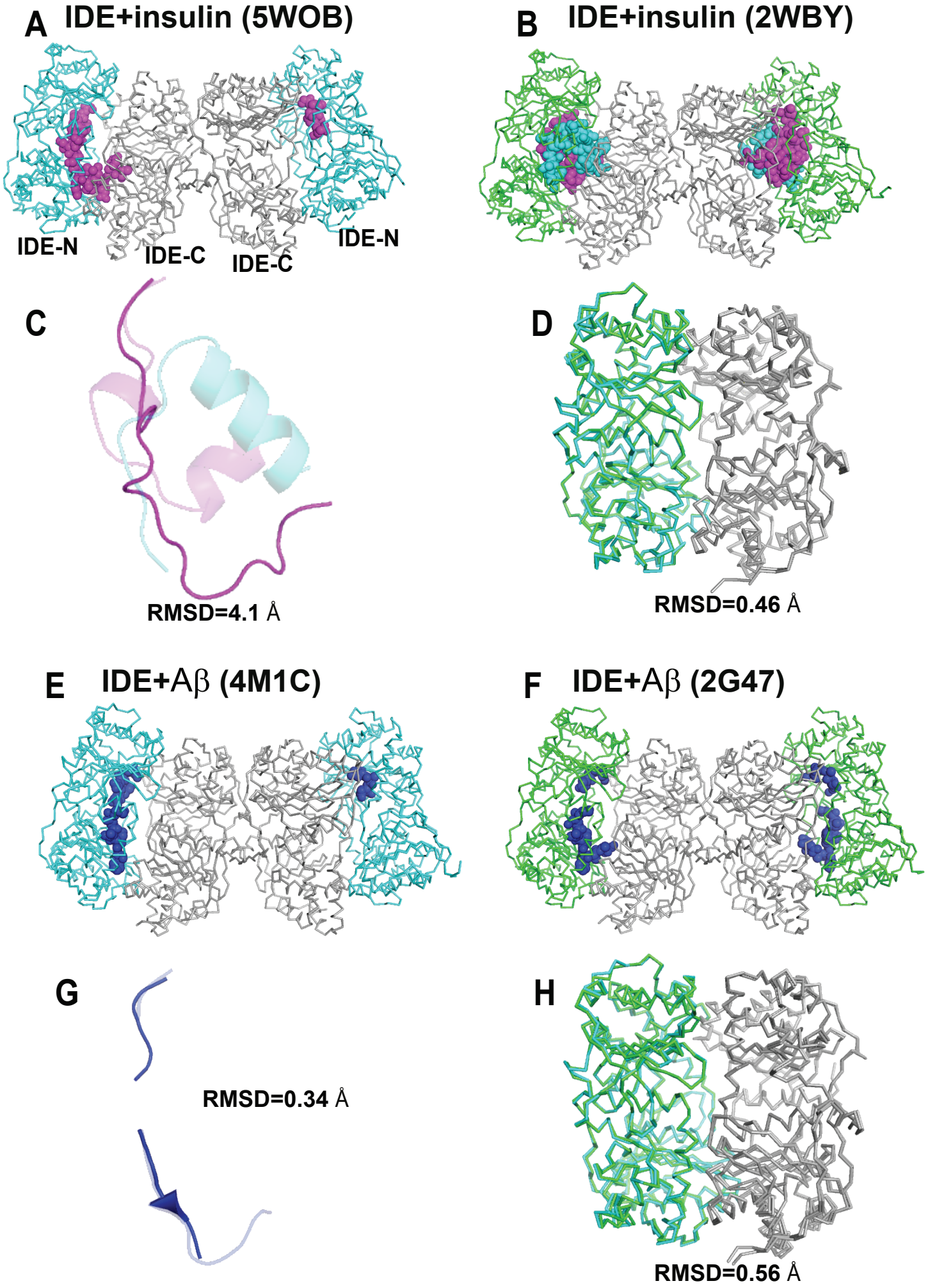

Figure 5 Figure Supplement 2

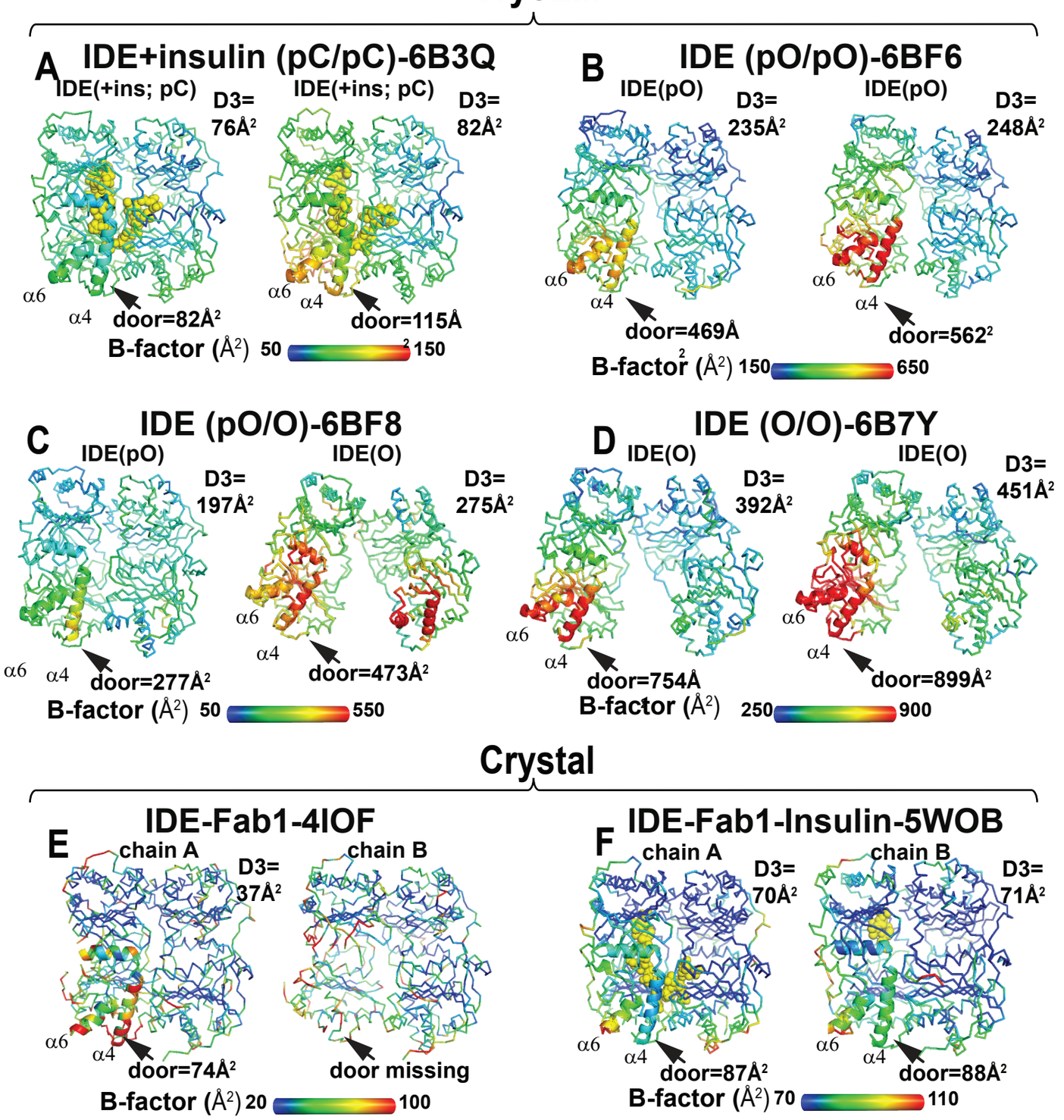

G CryoEM

Domain Name	IDE+insulin		IDE					
			pO/pO		pO/O		O/O	
	pC+ins	pC+ins	pO	pO	pO	O	O	O
Door (176-236) Å²	82	115	469	562	277	473	754	899
α4α6 (176-193, 221-235) Å²	85	121	546	651	346	481	865	967
D1 (43-285) Å²	94	122	425	519	273	428	704	854
D2 (286-530) Å²	86	106	276	385	170	330	465	587
D3 (531-768) Å²	76	82	235	248	197	275	392	451
D4 (769-1011) Å²	84	85	279	280	224	372	445	518

H Crystal

Domain Name	4IOF		5WOB		4M1C		5UOE	
	chain A	chain B	chain A	chian B	chain A	chian B	chain A	chian B
Door (176-236)	74	missing	87	88	81	72	76	81
α4α6 (176-193, 221-235)	80	missing	89	91	86	75	78	83
D1 (43-285)	65	61	85	85	82	72	76	78
D2 (286-530)	39	50	77	79	75	69	74	77
D3 (531-768)	37	37	70	71	69	69	70	75
D4 (769-1011)	42	42	81	79	74	67	74	80

Figure 5 Figure Supplement 3

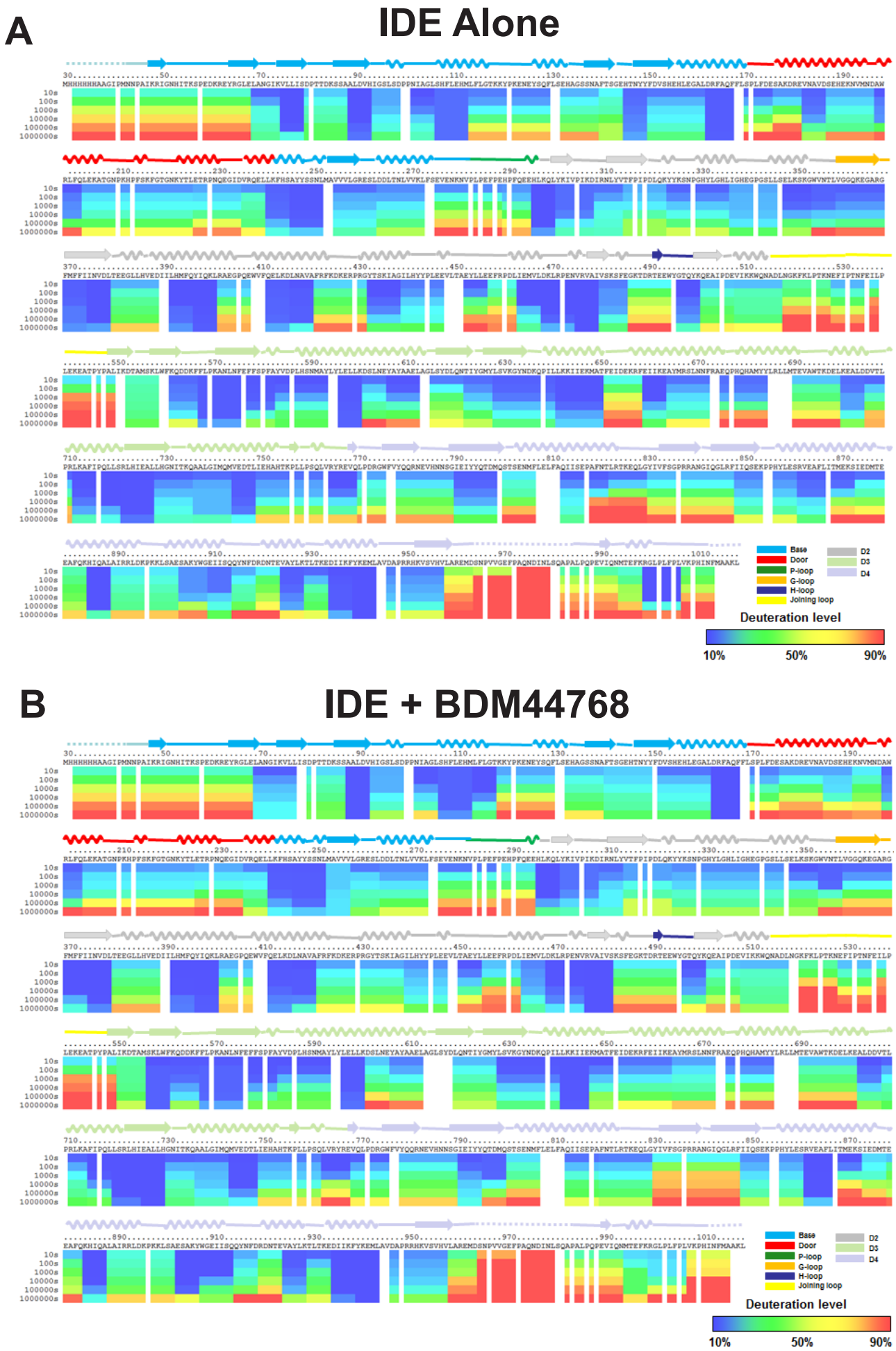

Figure 5 Figure Supplement 4

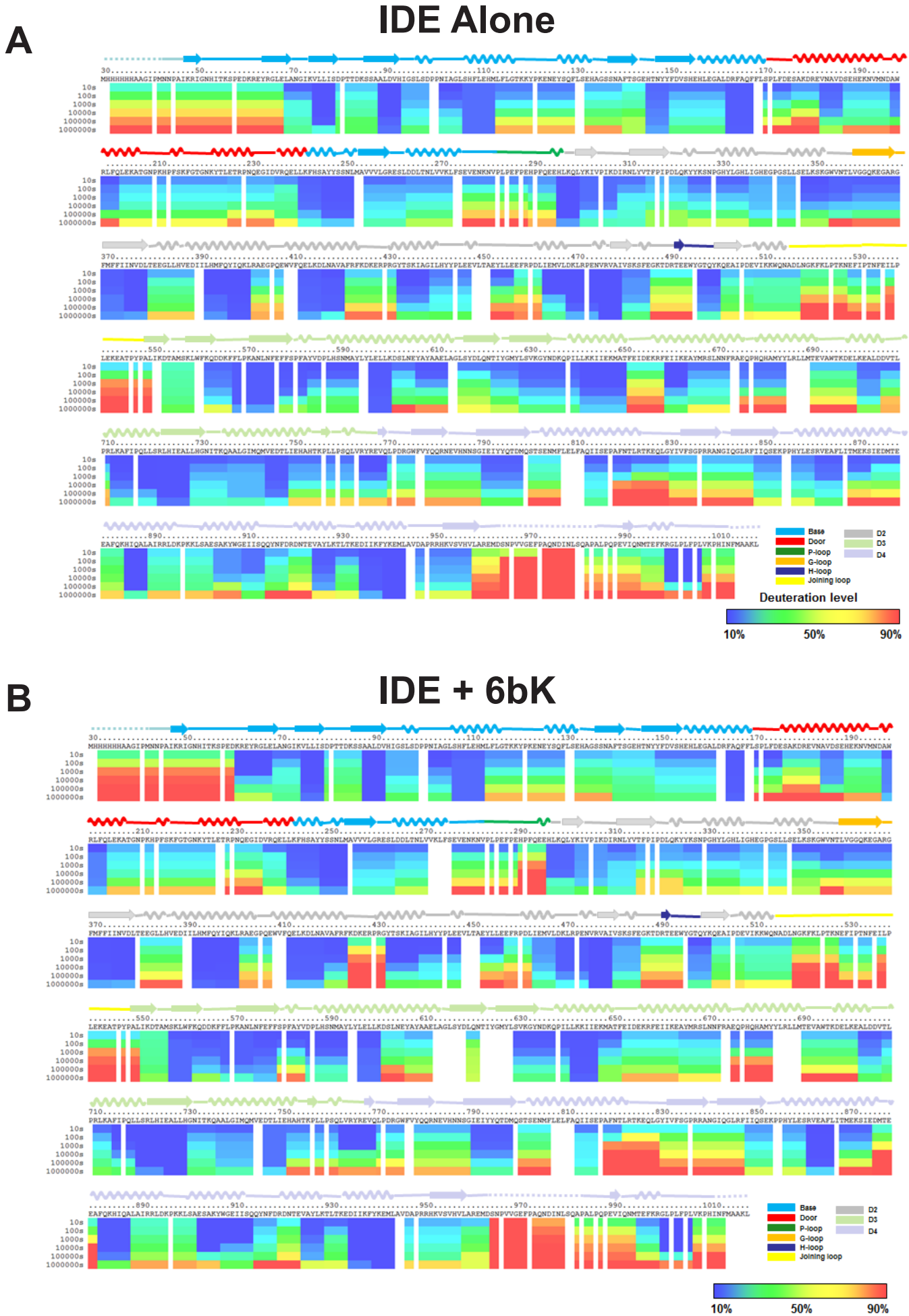

Figure 5 Figure Supplement 5

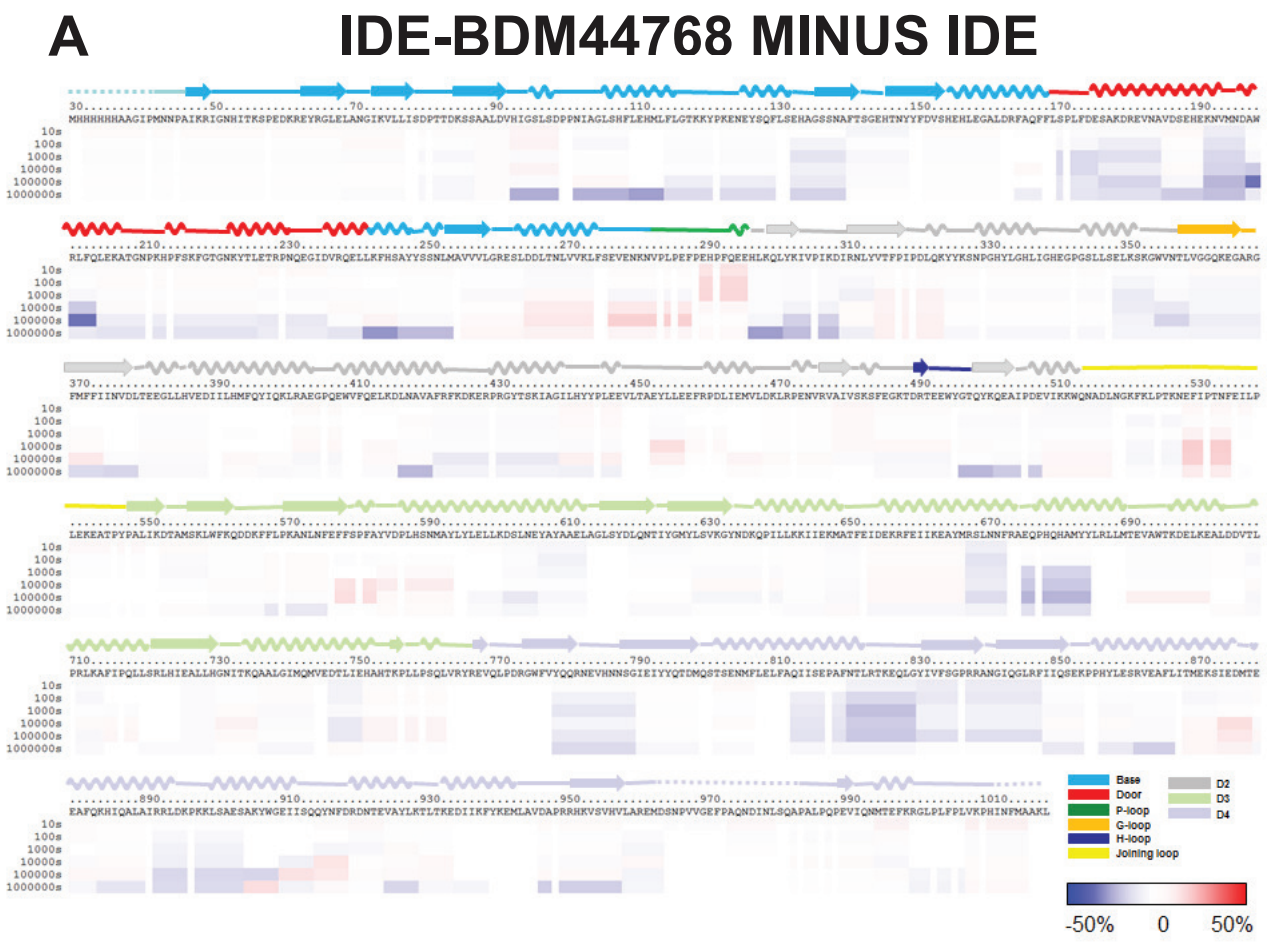

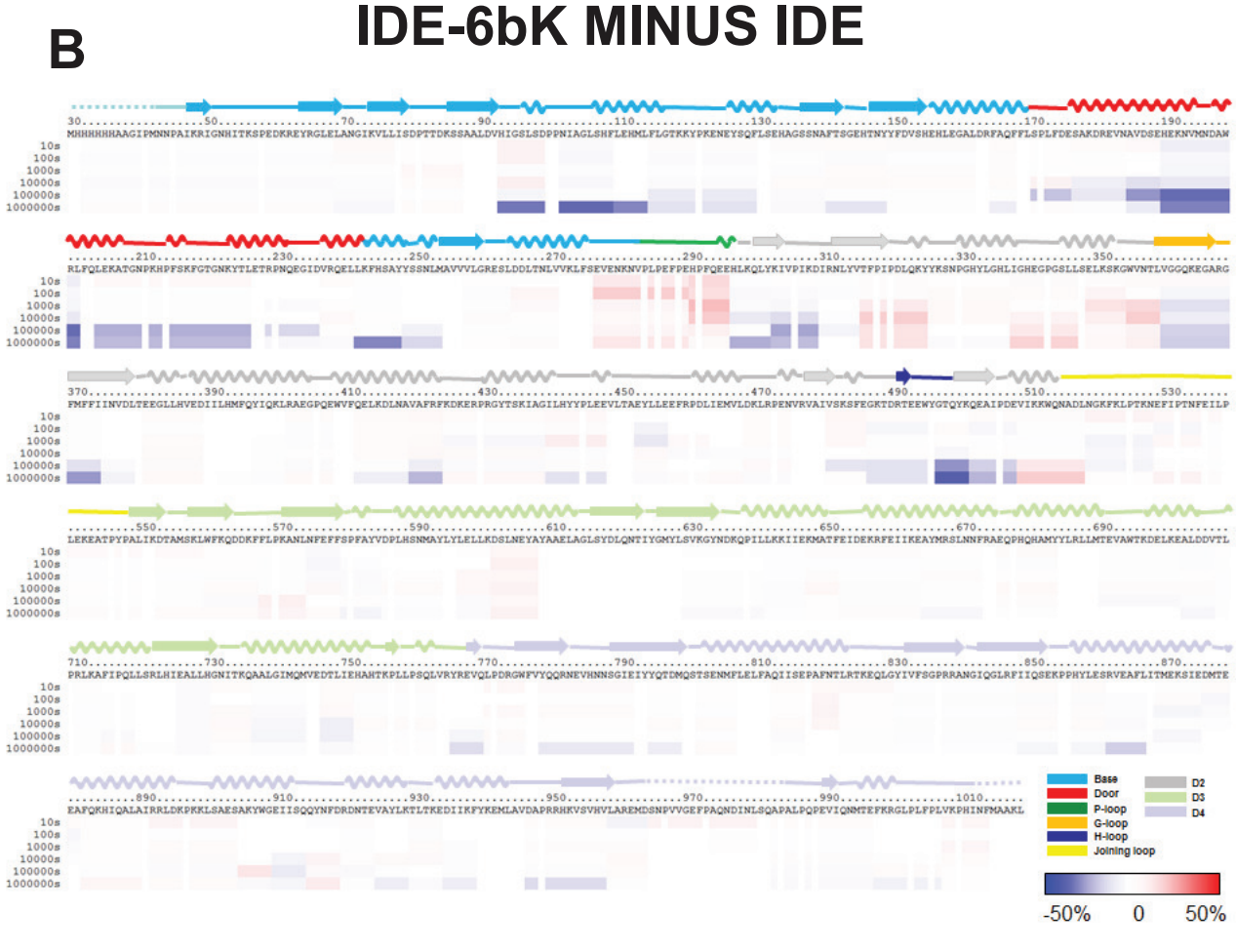

Figure 5 Figure Supplement 6

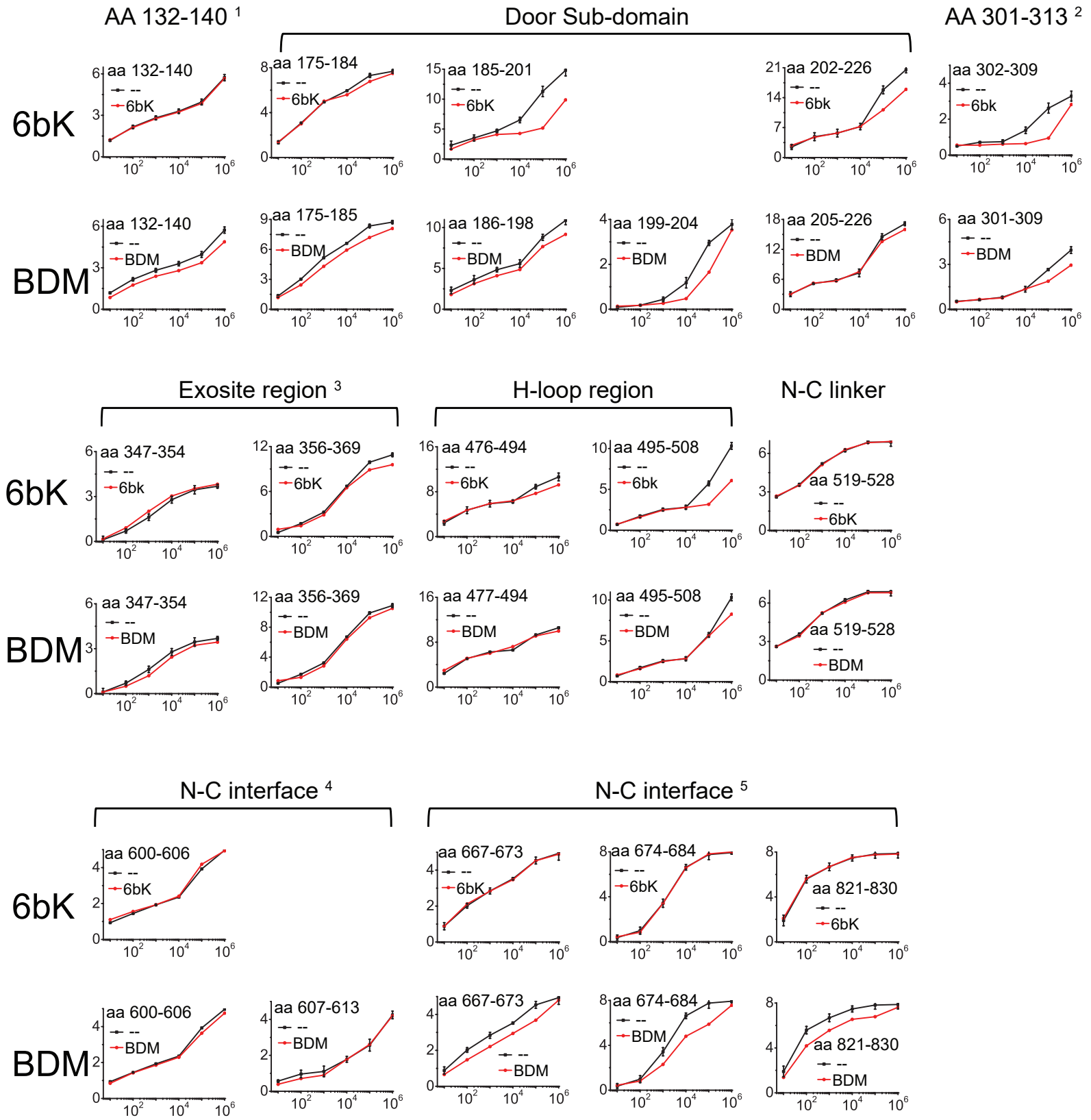

[1] One of the amino acid range that involves in the BDM44768 binding.
[2] One of the region that has changes in H/D exchange rates of IDE induced by binding of 6bk.
[3] aa 347-354 is on the N-C interface, close to aa 600-606, and is part of the linker loop enviroment. aa 356-369 is the major substrate binding site.
[4] The region is under the N-C linker, and consists part of the enviroment of F530.
[5] These regions interact with the Door sub-domain when IDE is closed.

Figure 6 Figure Supplement 1

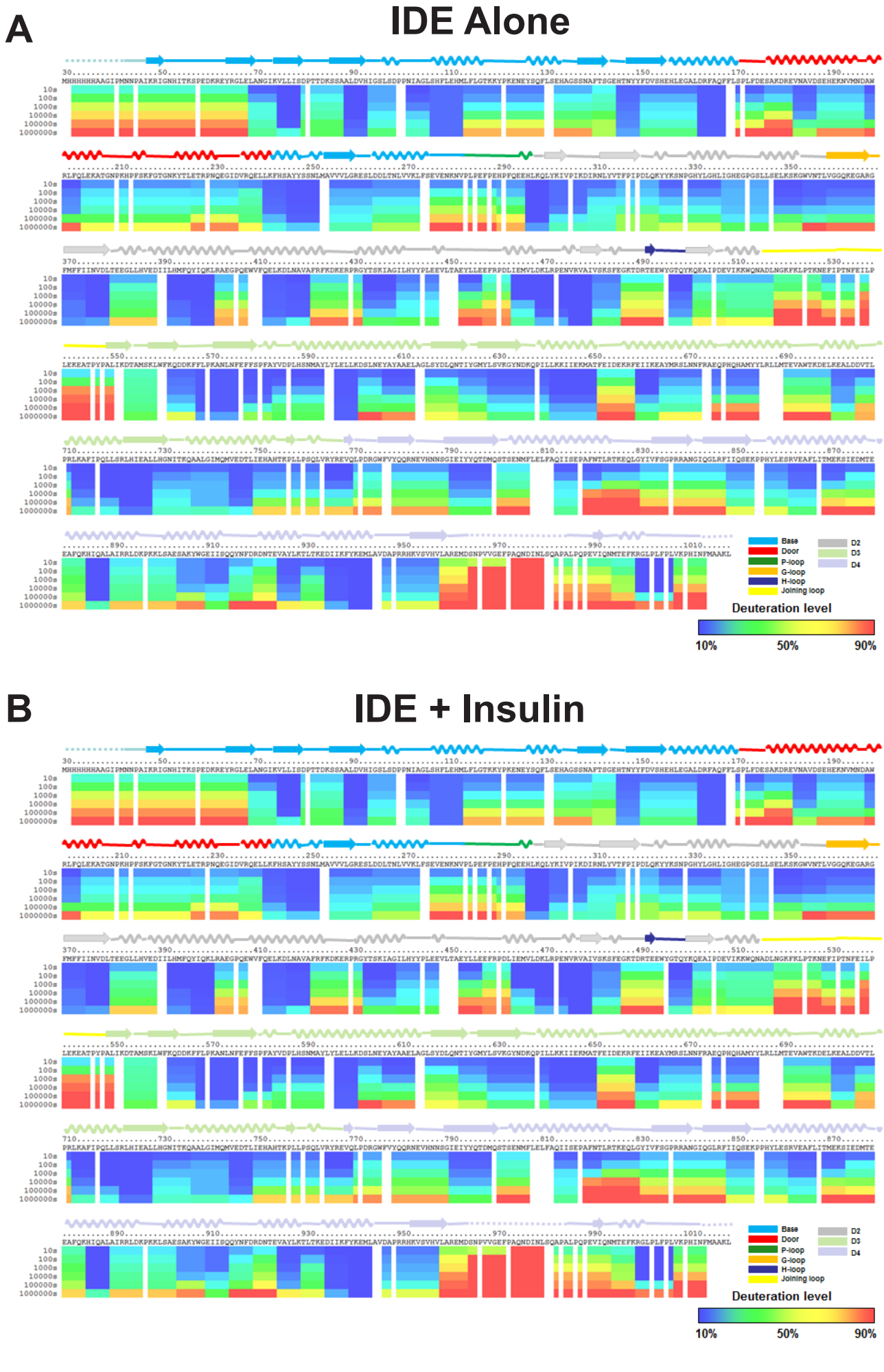

Figure 6 Figure Supplement 2

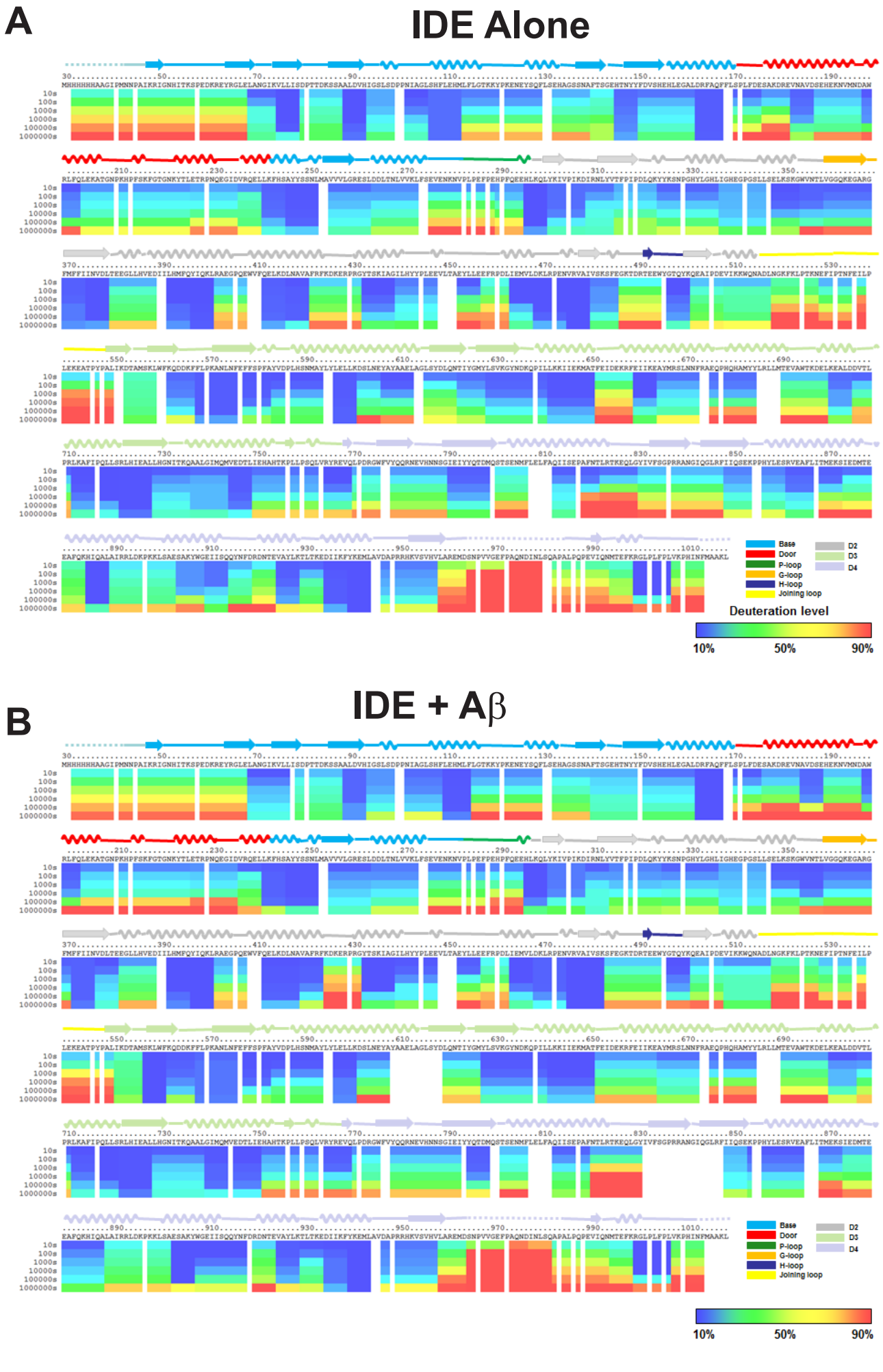

Figure 6 Figure Supplement 3

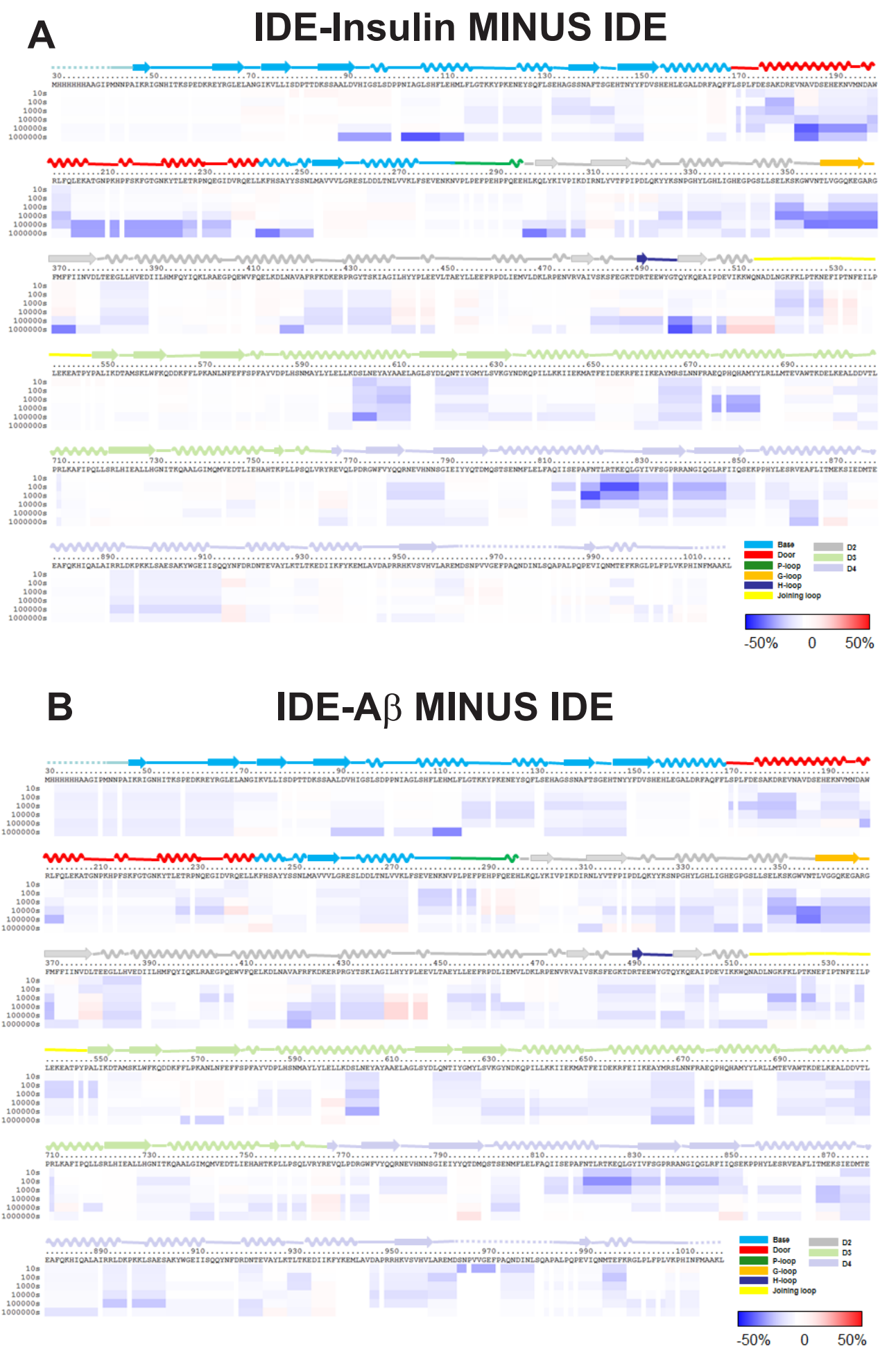

Figure 6 Figure Supplement 4

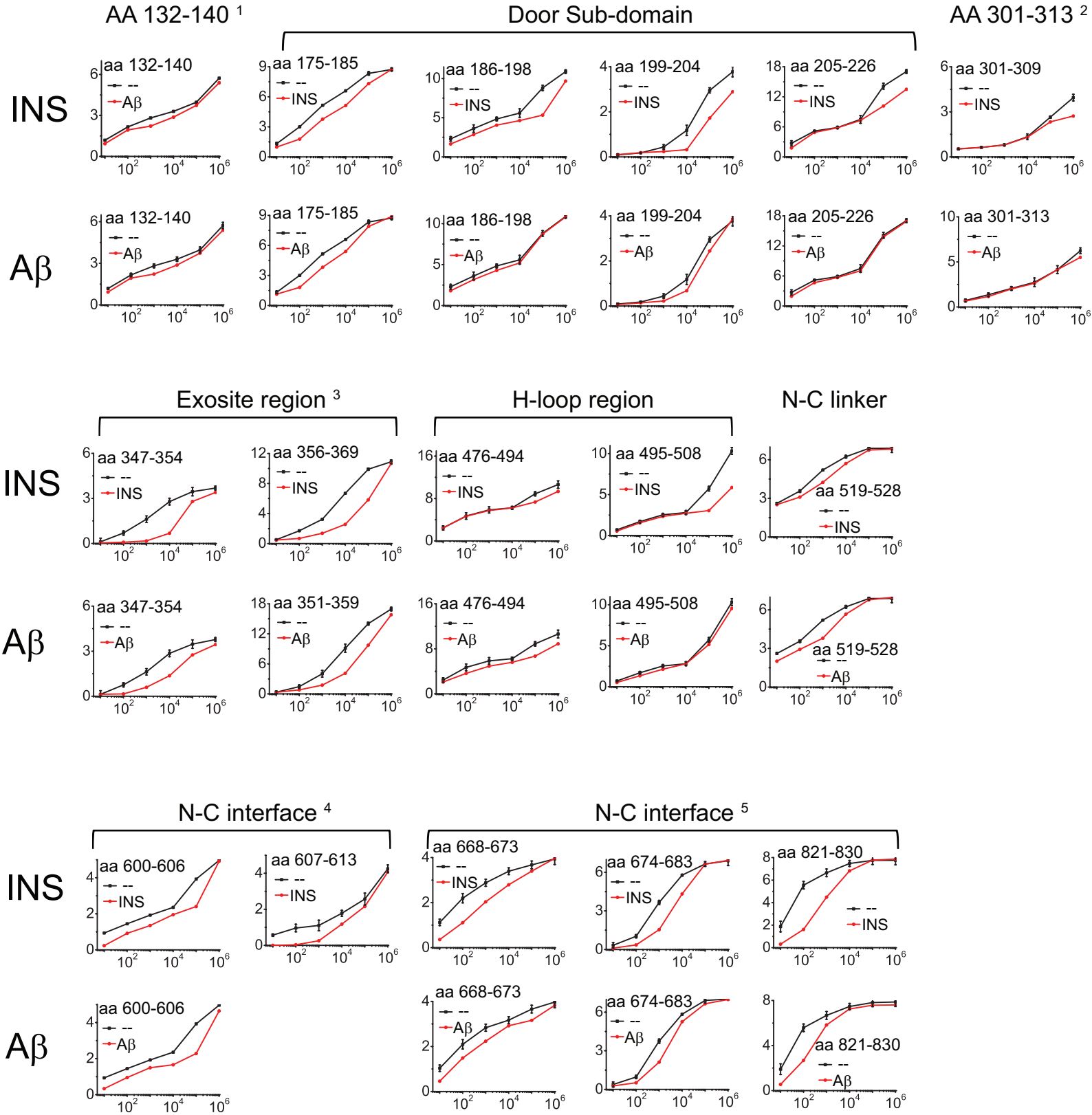

[1] One of the amino acid range that involves in the BDM44768 binding.
[2] One of the region that has changes in H/D exchange rates of IDE induced by binding of 6bk.
[3] aa 347-354 is on the N-C interface, close to aa 600-606, and is part of the linker loop enviroment. aa 356-369 is the major substrate binding site.
[4] The region is under the N-C linker, and consists part of the enviroment of F530.
[5] These regions interact with the Door sub-domain when IDE is closed.

Figure 7 Figure Supplement 1

IDE+Fab1+insulin (crystal)

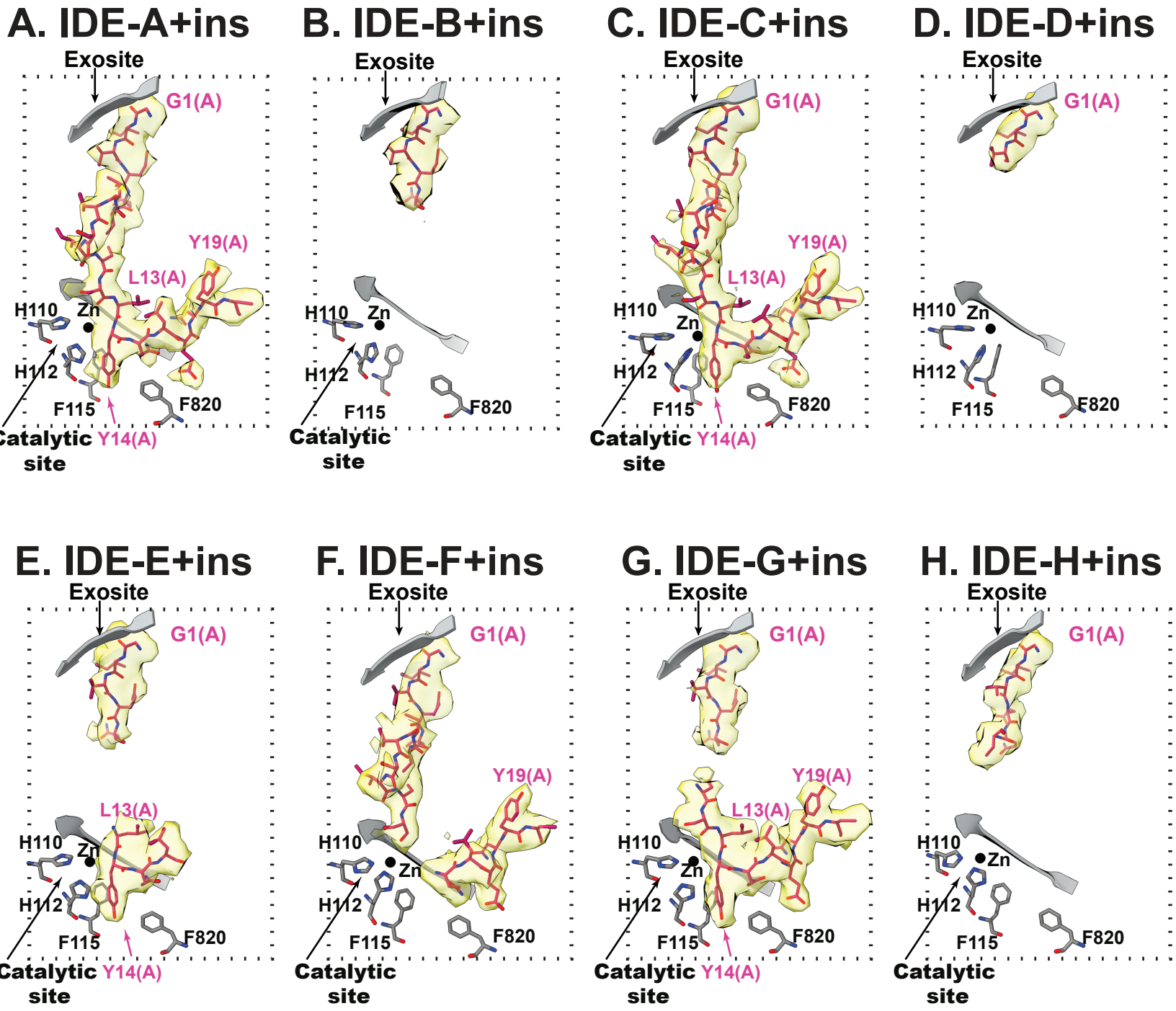

Figure 7 Figure Supplement 2